Quantifying microenvironmental changes in the developing brain in response to acute and chronic metabolic disrupters

Brendan Patrick Butler

A dissertation

submitted in partial fulfilment of the

requirements for the degree of

Doctor of Philosophy

University of Washington

2025

Reading Committee:

Elizabeth Nance, Chair

Cole DeForest

John Berg

Program Authorized to Offer Degree:

Chemical Engineering

University of Washington

Abstract

Quantifying microenvironmental changes in the developing brain in response to acute and chronic metabolic disrupters

Brendan Patrick Butler

Chair of the Supervisory Committee:

Elizabeth Nance

Department of Chemical Engineering

Neurologic diseases are responsible for nearly one-third of all deaths and disability life-adjusted years, many with no effective treatments or cures. Treating the diseased brain is challenging physically, biologically, and clinically: the brain has multiple unique barriers to therapeutics, neurologic disease processes are highly multiplexed and variable, and the presence of pre-existing co-morbidities or prior neurologic conditions changes the disease landscape, complicating or impeding treatment efforts. In this work, we touch on all three challenges. We focus on metabolic disruptions in the form of mitochondrial dysfunction, which is implicated in nearly every neurologic disease and is shown to be a mediator of risk and susceptibility. We use organotypic whole-hemisphere (OWH) brain slice cultures to quantify how mitochondrial dysfunction alters the physical and biological microenvironments of the brain. First, we develop an OWH slice model of mitochondrial dysfunction using the canonical inhibitor rotenone (ROT). We observe region-, dose-, and time-dependent microenvironmental changes that mirror in vivo models. We also show how the extracellular microenvironment, a critical therapeutic barrier, is altered by mitochondrial dysfunction. Next, we characterize how mitochondrial dysfunction from ROT exposure

modulates susceptibility to stroke-like injury using an oxygen-glucose deprivation (OGD) model, an effect which has not been previously investigated in vitro. Here, we demonstrate that timing of metabolic disruption relative to the OGD insult worsens tissue recovery. Gene expression analysis and imaging reveal a connection between mitochondrial state and inflammatory responses as one driver for metabolic-related effects on OGD recovery. Our findings highlight a role of pre-existing metabolic deficits in neurological injury and recovery, capture changes in microenvironment features that can impact therapeutic delivery and enable pre-clinical screening platforms that better represent the clinical scenario for patients seeking treatment for neurologic disease.

Table of Contents

List of Figures

List of Tables

Acknowledgments

Thank you to my supervisory committee: Dr. Elizabeth Nance, Dr. John Berg, Dr. Cole DeForest, Dr. Jon Weinstein. Your feedback and guidance helped me continue to grow and ask more from my science at each major milestone. I'm excited to be sharing this final product with you. To Dr. Zachary Sherman, thank you for being willing to join my supervisory committee for the final part, I'm looking forward to having your perspective and feedback.

To my family, thank you - without you, none of this would have been possible. You supported me moving across the country to chase my goals in an uncertain time, selfishly letting another loved one go away at a time when we were most isolated. It's the same unconditional love and support you gave me in 4th grade as a I sat on the couch with a geometry textbook and in middle school when I dragged you all to the Greek Festival so I could practice my newfound language skills. Mom, thank you for your non-stop support and care over the years. I always felt like you were right here, and I've never felt luckier to be your son. Dad, thank you for your support, curiosity, and always asking to read those long documents like this one. I hope you're proud of my biggest "research project" yet. Tommy, every time I get to come home and see you, grab Chipotle and quote our favorite movies is the best reset to remember what life was about (he may be a doctor, but you should still call 9-1-1).

To Bettegene Butler, Granny, (and Papa Jim from above), thank you for all you did to support my educational journey out here, inspiring me to strive for excellence, to value humor and wit, and the joy of a martini with the ones you love. Thank you to all my other Butler and Cozzi family (I could break the word count with this one) for all the time spent at holidays and gatherings, hanging out, and asking me questions about what I'm actually doing out here. We've all had such big moments over the last five years, and I can't wait for many more with all of you. I love you all.

To Elizabeth, I don't know if there are enough words to thank you for everything you did, but my gratitude stems from every word of this document. You went immeasurably above and beyond to ensure I became the best scientist and person I could be, before I even knew what that looked like. You believed in me from the start and wanted me in your lab (even after reading my incredibly unfocused GRFP proposal). You were patient and compassionate yet taught me better discipline and knew how to steer me in the right direction when I faltered or got too lost in my head and forgot what all of this was about. I'm grateful to have had you in my corner and I look forward to our continued relationship as I set my own path in academia. I hope you know how much my time as your student meant to me. Thank you for all the times you and Tommy (and the pups) welcomed me into your home as well. You also have the thanks of the 40 or so Midwesterners above who think you are an absolute rockstar.

To my fellow Nance Lab members past and present, particularly Nuo Xu, Nels Schimek, Gaby Balistreri, Emily Du, Ruby Jin, Sydney Floryanzia, and Colin Landis - thank you for being my community for the last five years. Each of you are brilliant scientists and lovely human beings, and I'm grateful to have worked with each and every one of you. Thank you for all you did to support me, I couldn't have done this without you guys as well. To Mike McKenna, thanks for all you did to help me when, frankly, I had no idea what I was doing. I'm happy to report our project is in good hands, and it's thanks to the foundation you built for me.

To my undergraduate research team: Gisele Charpentier, Kristin Bennett, Malcolm Renney, and Jay Kimerling. Thank you for everything you did to make our research possible. Thank you for trusting me as your mentor through these years and thank you for being patient with me as I learned what it meant to carry that role. I absolutely adore each of you and I'm so proud of what you accomplished and will continue to do. Kristin, I especially need to thank you for stepping in to be that person for me every time I needed it (which was often). All of the conversations, 211 jam sessions, laughs, tears, meals, and rides home provided unwavering support that I am forever grateful for. Thank you and Jesse, and the kids (and the dogs), for always sharing your home with me.

To all of our wonderful staff in Benson Hall, Andrea, Nhan, Ben, Anita, and many others. Thank you for all you did to keep that place running and all you do to make sure our research happens and that we feel supported.

To Macoy McLaughlin, from the moment we met to now, you've supported me every step of the way. You saw every late night, long day, and early morning (usually because you were awake before me), every everything. Thank you for always pushing me to stay in it and do my best, no matter how badly I wanted to quit. I love you. And to Jennifer McLaughlin, who was here where my mom couldn't be, I hope you know how much you contributed to this as well and how grateful I am to have had your support.

To Ava Karanjia, Duncan Reece, Anthony "Rudy" Pyka, Maria Politi, Widi Sugianto, lifelong friends I made by sheer coincidence that we all decided to pursue our PhD's in the same place at the same time. Each of you made this whole thing 100% better. You all touched my life in unique ways and I'm grateful for all you did to support me as a friend. I can't wait to continue our friendships beyond grad school.

To ChemE graduate math, for bringing in Matthew Canin, followed by Tanner O'Rourke and Julian Willnow. You three made the state of Washington home for me. Love you boys.

Outside of graduate school, I was so fortunate to meet so many people who made Seattle a second home. Thank you, Matt Taylor, for your support and friendship over the years and for bringing me into your family as well. Giuseppe Inglima, Joshua Biggs, Pili Laulu-McFaul, I found such wonderful friends in all of you. You allowed me to nurture a part of myself that needed it and made life outside the lab so much fun. Looking forward to everything we get to do together in the future.

To Liz Eboli, Samantha Siu, Mark Fratto, Elena Mendez, Emma Varsbergs, and Lauren Eboli, thanks for always being there every trip home. I'm looking forward to the many years ahead of travel and fun times.

To Hannah Howell, Kevin Patel, Nick Narla, and CJ Jacobs, the OG Purdue squad who were there for my humble beginnings as a chemical engineering student, and human being learning to make his way in the world. You are the foundation of this journey and always in my heart.

To Dr. Visali Ratakonda, (soon to be Dr.) Jonah Wirt (even though you should get the title by default now since you've already published more than I did), Reem Ali Esq., Allie Dolz-Lane and Maddie Dolz-Lane (both of you are going to get your PhD's I'm calling it), my beautiful and brilliant friends I had the pleasure of growing up with. Thank you for all the calls and FaceTimes as I adjusted to my new life here in Seattle, and for having me by your side to continue to celebrate life's big moments with you.

Lastly, to Timmy. I promised myself when I started this thing that I would end with a dedication to you and your memory. You met my childhood interests of geography, art, and cultures with genuine enthusiasm, and I know you would have approached our conversations about neuroscience with the same kindhearted nature. I'm privileged to live out my life as a scientist and human in your honor. We love and miss you every day.

Chapter 1. Introduction

1.1 Impacts of neurological diseases

Nearly 1 in 3 people in the United States suffer from neurologic disease, which constitutes the leading causes of death and disability-adjusted life years [1,2]. The cost of treatment per year for all neurologic diseases comprises $800B annually, not including the added financial burden of caring for pre-existing or resulting co-morbidities, nor the burden on the patient's support system to provide additional care[1]. Despite the prevalence and severity of neurologic disease, many do not have curative or preventative therapies, and current standards-of-care cannot address systemic causes of neurologic disease pathophysiology, herein termed neuropathophysiology. Furthermore, trauma or disease to the brain increases risk of developing future neurologic disease, leading to compounding clinical, financial, and social burdens. For example, stroke in elderly populations with dementia has a 4x higher mortality rate compared to those without cognitive defects; additionally, an elderly person who experiences stroke has a higher risk of developing Alzheimer's disease[2,3]. At the other end of the lifespan, newborns who survive brain injury around the time of birth are more likely to develop cerebral palsy or other neurodevelopmental or neuropsychiatric disorders[4,5]. Adolescents and adults experiencing anxiety and depression are at a higher risk for dementia[6]. Therefore, it is of critical interest to investigate neuropathophysiologies in a way that enables study of multiple overlapping, often feed-forward, hallmarks. The cyclical nature of neuropathophysiologies inevitably accelerates clinical, financial, and social burdens, which already present major strains on the U.S economy and healthcare system.

1.1 Hallmarks of neuropathophysiology: a multi-parameter interaction space

The pathophysiology of neurologic disease is represented by several main hallmarks, all of which can interact with each other, leading to upregulation, downregulation, or bidirectional effects, depending on the input stimulus[7]. These include hallmarks (labeled in red) and natural or environmental inputs (labeled in blue), connected by physiological responses (black) (Fig. 1.1). One example hallmark is

inflammation, acute or chronic, typically where microglial cells (the resident immune cells of the brain) become activated and engage in processes to eliminate sources of tissue damage, which involves clearance of dying or dead cells[8,9]. Oxidative stress arises from the mismanagement of radical oxygen species (ROS), which naturally accumulate in mitochondria yet trigger cell death or inflammatory pathways when unregulated. Another hallmark characterized by imbalance or dysregulation of a molecule that exists as a normal part of neural cell function is glutamate toxicity. Glutamate is a primary excitatory neurotransmitter for neural cell communication, but excessive buildup can lead to cell damage or death[10]. Cell death can result from a variety of pathways, such as apoptosis (programmed cell death), necrosis (uncontrolled cell death resulting from environmental stimuli), or ferroptosis (excessive iron accumulation preventing clearance of radical species).

While the example figure maps the interaction space of neuropathophysiological hallmarks and their causes in the context of nanoparticle delivery to the brain, it is a useful visualization of the complexity of these pathways. Furthermore, it provides us with a foundational starting point for this work: identifying a cause or multiple causes implicated in neurologic disease and analyzing how each contributes to the development of neuropathophysiological hallmarks. In this work, we will focus on cellular energy metabolism, how it can be disrupted, and the consequences for the risk and onset of neuropathophysiological hallmarks.

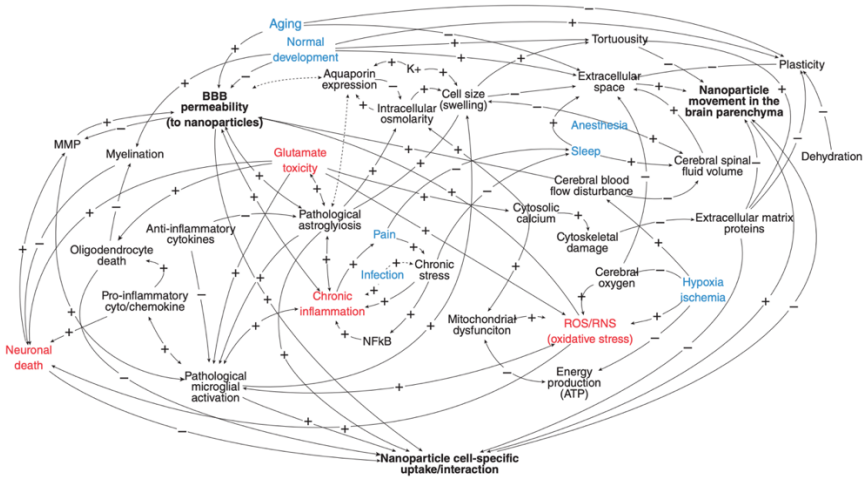

Figure 1.1. Systemic map of neuropathophysiological hallmarks (red) and examples of natural or induced effects (blue), connected by the brain's physiological responses (black). Pluses indicate

upregulation and minuses indicate downregulation, and double-sided arrows indicate bidirectional effects. Adapted from Curtis et al., 2016.

1.2 Role of cellular energy metabolism in neurologic disease

Because the brain is our most energy-intensive organ, utilizing nearly 20% of the body's total energy at 2% body mass, disruptions in cellular energy metabolism are severe and are associated with a wide range of neurologic diseases[11,12]. In addition to association, metabolic disruptions are also shown to be a root cause of several neuropathological hallmarks[13–17]. In this work, we focus specifically on mitochondrial dysfunction due to its widespread role in neuropathophysiology. For example, the age-related cognitive decline leading to the development of neurodegenerative diseases is characterized by chronic decline of mitochondrial function, which is also associated with ROS buildup and chronic inflammation[14,18]. Ischemic events like stroke, characterized by lack of blood flow to the brain, deprive neural cells of necessary energy generation substrates such as oxygen and glucose, therefore disrupting metabolism and causing ROS buildup and inflammatory responses. Glutamate toxicity, involved in stroke and a variety of neurodegenerative diseases, can lead to mitochondrial impairment due to excessive calcium influx; at the same time, ROS buildup from dysfunctional mitochondria can render neurons more susceptible to damage from excessive glutamate[19]. Other neurologic diseases and disorders that involve metabolic aberration, typically in the form of mitochondrial dysfunction, include anxiety and depression, autism spectrum disorder, schizophrenia, addiction, and obsessive-compulsive disorder[16,20–22]. Furthermore, co-morbidities and other lifestyle factors can also lead to mitochondrial dysfunction in the brain. Lastly, mitochondrial damage has important implications, for familial neurologic disease because mitochondrial DNA (mtDNA) is highly conserved, and relative abundance of mtDNA is influenced by mitochondrial dysfunction[23]. Ultimately, mitochondria are critical players in a variety of feedback loops critical to neural cell survival. Therefore, strategies to understand disruptions to cellular metabolism in the form of mitochondrial dysfunction can enable investigation into how neuropathophysiological hallmarks interact and provide opportunity to accurately screen therapeutics in the presence of co-morbidities or competing neurologic disease.

1.3 Models of the brain environment

Studying the roles of cellular energy metabolism and mitochondrial dysfunction in a neuropathological setting requires model systems that accurately reflect the native brain environment and enable tunability with a variety of stimuli implicated in mitochondrial dysfunction. Unfortunately, the current availability of models that achieve these goals are limited – addressing this gap is a core tenet of this thesis work. It's important to overview the types of model systems that exist to probe neuropathophysiology and discuss their advantages and disadvantages. Each has a place in these studies, yet the choice of model system needs to be appropriate for the types of questions being asked.

The types of model systems for the brain environment include *in vivo* animal models, *in vitro* cell models, engineered tissue models, or synthetic models. Each comes with its own benefits and drawbacks, which are discussed in a comprehensive review in Chapter 4. The model system that is most representative of the native brain environment is the *in vivo* model, and the least representative models include *in vitro* single-cell models in 2D or in hydrogels designed to mimic the stiffness of the brain. These two classes of model systems represent the boundary conditions of a continuum between native representation and experimental access. Advantages of *in vivo* models include perfectly native representation of the brain environment, clinical translational relevance, and access to behavioral studies; however, animal housing costs are expensive, animal-to-animal variability must be considered, and the choice of species matters for accurate representation of neuropathophysiology in humans. *In vitro* 2D or hydrogel models do not represent the native brain environment, often focusing on limited or single cell types, but are tunable systems that provide valuable opportunities to test cellular and extracellular responses to various stimuli. In the middle of the continuum are *ex vivo* models like organoids and organotypic cultures, the latter of which is the focus of this thesis work. Other engineered systems such as microfluidic devices for blood-brain barrier (BBB) modeling and brain-on-a-chip models to incorporate electrophysiology but are promising yet not developed enough to stand on their own without a supplementary *in vivo* or *in vitro* model system to support their findings. Ideally, analysis of neuropathophysiological hallmarks would draw from studies that span a variety of model systems, but this is not always feasible.

1.5 Cultured organotypic brain slices

In this work we focus on cultured organotypic whole-hemisphere brain slice models as our primary model system. Organotypic brain cultures are thin slices of brain tissue (~300-450 μm) that can be harvested from animal or human donors cultured from days to Click or tap here to enter text.weeks.[24,25] Generally, organotypic cultures obtained from younger donors respond better to culturing and can survive weeks to months *in vitro*, however techniques are emerging that enable viable culturing of tissue from older donors or patients to provide more age-specific or disease-specific relevance[26–29]. Organotypic brain slice cultures may include just a single region (hippocampal, striatal, cortical) or include the whole-hemisphere (OWH). Organotypic brain slice cultures retain native cytoarchitecture and extracellular matrix (ECM), and for OWH cultures, the presence of multiple regions.

The two most characterized methods for preparing and culturing brain slices are the roller tube and semi-porous membrane techniques, but the latter is more widely used and is the slice technique used in this work. In addition to experimental access to a native representation of the brain environment, a single animal can yield tens of brain slices, minimizing animal lives and animal-to-animal variability. Slice cultures also reorganize in structure throughout culture and in response to biological stimuli, making them a dynamic system to study the brain environment. Researchers have used *ex vivo* brain slices to measure changes in extracellular space (ECS) volume[30], the diffusion of nanoparticles[31,32], effect of formulation parameters on nanotherapeutic localization[31,32], gene expression in response to stimulated excitotoxicity, hypoxia-ischemia, and mitochondrial dysfunction[33–35], morphological features of microglia populations[36–39], and ECM protein expression[40–43]. OWH slices are most suitable for the scope of this thesis work because they allow for the input of various stimuli to introduce mitochondrial dysfunction and abnormal metabolic environments, and the opportunity to screen neuropathophysiological hallmarks at a variety of relevant length and time scales, from the RNA level to the ECM.

1.6 OWH slice cultures to study region-dependent extracellular properties in tandem with cellular responses

Access to native ECM is a major advantage of organotypic brain cultures, with the added advantage in OWH cultures of access to region-dependent ECM. The ability to study extracellular properties as a function of neuropathophysiological state is important for both our holistic understanding of disease processes, but also to study how a disease state may influence the delivery of a therapeutic.

1.6.1 Roles of the ECS and ECM in neurobiology

While much of the brain's function is determined by complex interactions of cells that take place in the brain environment, the ECS and ECM are also known to play critical roles in mediating and modulating these interactions[44–46]. Increasing evidence demonstrates the role of the microenvironment as dynamic, capturing disease and injury processes as a neurological and micromechanical sink. Several studies have shown microstructural changes in the brain environment in a variety of injury and disease states, such as traumatic brain injury (TBI), Alzheimer's and Parkinson's Diseases, cancer, depression, and aging[47].

Structurally, the ECS is space between cells - a narrow (primarily nanometer-length scale), tortuous environment that resembles porous media, albeit discontinuous with the presence of dead-space domains[48,49]. Bulk properties of the ECS include tissue extracellular volume fraction ($\alpha = VECS/VTissue$), width $dECS$, and tortuosity ($\lambda = (DW/DECS)^{1/2}$), which describes the extent to which the diffusion of water molecules in the ECS diffusion deviate from free molecular diffusion. Early efforts to characterize brain microstructure focused on quantifying these parameters and inspired the development of novel techniques to probe their heterogeneity. The first measurements by Nicholson and Syková used real-time iontophoresis (RTI) (discussed in Chapter 4) with the tetramethylammonium ion (TMA^+) to attribute approximately 20% ($\alpha = 0.20$) of healthy brain volume to extracellular space and showed reduction to 4% in an *in vivo* adult rodent model of acute ischemia[50]. RTI experiments revealed age- and state-dependent tortuosity in brain tissue, and future studies showed changes in extracellular volume fraction based on sleep state and presence of neuropsychiatric disorders[46].

The ECM fills the narrow confines of the ECS, a structure compositionally and functionally unique to the brain that has a variety of important neurobiological functions. Serving as a scaffold structure, the ECM surrounds resident cells to support intracellular communication, promote cell potentiation, and provide mechanical integrity to brain tissue[45]. The ECM consists of three parts: a basement membrane exterior to vascular endothelial cells; a neural interstitial matrix that provides structural support and spacing for cells; and perineuronal nets (PNNs) that surround and support interneurons. The basement membrane is comprised of laminin, type IV collagen, fibronectin, and a heparan sulfate proteoglycan. The neural interstitial matrix is comprised of a proteoglycan matrix cross-linked by covalent bonds and link proteins. The class of brain ECM proteoglycans primarily consist of hyaluronan chains, which are covalently bound to sulfated disaccharide chains (glycosaminoglycans, or GAGs) known as chondroitin sulfate. The ECM maintains an effective negative charge from the presence of hydroxyl groups on disaccharide chains. Hyaluronan, or hyaluronic acid (HA), serves as the backbone for CSPG binding and is the primary modulator of ECM viscosity[51]. The ECM is capable of stiffening and fluidizing like a standard hydrogel, with link proteins such as aggrecan, brevican, and tenascin-R. Brain interstitial fluid (ISF) contains and maintains the concentration of critical ions for synaptic transmission, such as Na^+, K^+, Ca^{2+}, and Cl^-, and can influence ECS volume[52].

Brain ECS and ECM are dynamic structures that undergo modifications in healthy states as well as neuropathological states. The ways in which the hydrogel-like structure of the ECM may deform in response to disease states has important implications in neurobiology[53]. Matrix characteristics such as pore size, viscoelasticity, and degradability can impact the degree to which cellular growth, spreading, and migration interact with ECM mechanical properties[54]. Brain tissue is considered to behave as a *viscoelastic* material, having properties of both viscous fluids and elastic solids[55,56]. This viscoelastic behavior has gained significant attention as a marker of disease dynamics within e ECS. For example, viscoelastic alterations are seen in chronic-progressive multiple sclerosis amyloid plaques in transgenic mouse models for Alzheimer's disease, and in brain aging[57,58]. Brain micro-rheology, specifically viscoelasticity, can underscore disease progression from a purely mechanical perspective and is a strong focal point in probing disease dynamics, especially with nano-based tools that can sense micro-rheology.

In addition to micro-rheological properties and bulk properties like extracellular volume fraction and tortuosity, ECS composition can also change in response to development, aging, disease, or injury and can directly impact diffusive ability and brain micro-rheology[41,56,59–62]. ECM composition can be measured by several techniques, including imaging, western blots, and mass spectrometry. While image-based methods are often considered qualitative or semi-quantitative, they provide a snapshot of bulk ECM protein distribution and presence within the ECS. Western blotting and immunoblotting can also be used to verify presence of ECM proteins and ECM protein expression in injury or disease models. Dot-blot immunodetection verified presence of proteins on brain-derived extracellular vesicles used as a treatment for hypoxia-ischemia in a slice model of oxygen-glucose deprivation[34]. Other methods to characterize ECM composition include tandem liquid-chromatography mass spectrometry (LC-MS), proteomics, and lipidomics, each of which are possible with the OWH brain slice model system.

1.6.2 Brain ECS and ECM as drug delivery barriers in the central nervous system

Nanoparticle platforms have emerged in recent years as promising candidates for drug delivery to the brain, given their tunability and capability of delivering a wide variety of agents. For neurologic diseases, nanoparticles are a prime candidate for translating benchtop discoveries to mass-produced therapeutics but face unique challenges in delivery to the central nervous system (CNS)[63]. Nanoparticles targeting brain parenchymal cells face a series of transport challenges immediately after administration, the first of which is the blood-brain barrier, followed by the brain ECS and ECM[64]. While most OWH slice models do not include a vascular component to model BBB transport, the presence of native ECS and ECM enable investigation into how nanoparticle vehicles interact with this secondary barrier. Nanoparticle probes in the brain ECS navigate and interact with a dense ECM of proteins and proteoglycans. The distinct biological roles of ECM structural features result in specific interactions with diffusing nanoparticles[52–54,65], which are quantified as part of Chapter 2 and the limitations regarding the interpretation of which are discussed in more detail in Chapter 5. More detail on techniques to probe ECS/ECM properties is discussed in Chapter 4.

While diffusion, rheology, and composition studies provide insight into changing biology within the ECS, from a disease understanding as well as drug delivery perspective, each also serves as only piece of a highly dynamic, heterogeneous system. It is critical to note that observing changes in one aspect does not directly assess or infer changes in another. For example, diffusion changes could be due to a variety of ECS properties: changes in ECM composition, local ion concentration, microstructural remodeling, or cellular processes. This interdependence of ECS properties was seen in the pioneering studies by Nicholson and Syková[48,66] and continues to be revealed with the development of novel probing techniques. Therefore, changes in the ECS measured by current technologies are often correlative and descriptive rather than mechanistic. Scientists can utilize a combination of model systems, probes, and methodologies to simultaneously capture the complexities and multiple length and time scales of brain ECS biology. In this work, we focus primarily on the multiple-particle tracking methodology to probe extracellular properties in live OWH brain slice cultures, and a variety of synthetic systems that capture distinct aspects of particle-ECM interactions.

1.7 Multiple particle tracking to probe the brain ECS and ECM

Multiple-particle tracking (MPT) is a state-of-the-art approach that has been used to quantify nanoparticle diffusion behavior in a variety of systems and predict system properties, such as gel stiffness and biological age of donor tissue[67,68]. Particle populations are captured at high magnification and frequency to yield tens of thousands of trajectories over millisecond time steps for a single experiment. Several studies, in biological and non- biological systems, applied particle tracking (single-particle (SPT) or multiple-particle) to characterize transport[69]. MPT and SPT have been applied to successfully study the transport of viruses in mucosal layers[70], particles in the vitreous fluid of the eye[71], during endocytotic and exotytotic events[72], particles in *E. coli* biofilms[73], and in the ECS of an *ex vivo* murine synucleinopathy model[74]. Prior work in the Nance Lab applied MPT to study nanoparticle diffusivity in *ex vivo* brain slices. We captured changes in brain effective diffusion coefficients ($D_{b,eff}$) of 40 nm PS-PEG nanoparticles in response to a range of stimuli, such as ECM-degrading enzymes, oxygen-glucose deprivation, and mitochondrial dysfunction[35,68,75]. We also observed distinct differences in diffusion data in tissue slices obtained from different developmental ages, wherein a convolutional neural network used trajectories to predict the age

of the donor tissue with 86% accuracy[68]. To interpret our data, we correlate data from assays and cellular images in parallel, time-matched experiments to hypothesize what is biologically responsible for changes in diffusive behavior. However, as will be discussed in the next section, this can often lead to inconclusive findings and it can be important to understand the effect of how trajectory sampling influences interpretation of MPT outputs.

1.8 Challenges in biological interpretation of MPT data

A principal challenge with MPT experiments, specifically in biological systems, is the ability to infer the biological driving forces behind apparent changes in diffusion. The ability to parse out which interactions are the dominant driving forces behind a particle's trajectory could be extremely beneficial for our approaches to nanoparticle design and our ability to infer biological insight from particle diffusion patterns. Ideally, particle trajectories from a single video or experiment could delineate the particle-system interactions that are driving diffusive patterns and then connect that to the biology of the system either directly or by correlation.

1.8.1 Methodological challenges for MPT data interpretation

One way MPT data outputs has been linked to the underlying biology is to make use of machine-learning (ML) pipelines to predict biological variables of the system in which particles are tracked. This has proven successful when the biological variable of interest is defined, such as the developmental age of brain slice donor tissue and the density of specific ECM structures[68], or the storage moduli of hydrogels[67]. MPT has been moderately successful in predicting whether an OWH brain slice received injury, like OGD or ROT, but is less successful distinguishing the type or severity of injury (OGD duration or ROT concentration). Strategies to improve predictions involve correlating trajectory data with other biological data, such as imaging or histology datasets, but this introduces its own limitations because the length and timescales of the measurements are less comparable. In addition to the functional state of the tissue being different (live vs. fixed tissue) and requiring extensive time and expensive staining materials, the spatial and temporal resolutions of imaging data are not the same. Use of different statistical methods like linear mixed-models have improved fidelity of predictions of biological variables[76]. Integration of parallel biological data, especially that which is collected in the same locations of the tracking sample,

are of interest but have not yet been extensively explored in brain tissue for their effect on predictive power. Ultimately, the ability to infer tissue functional state from particle trajectories is of significant interest and would be beneficial to our understanding of particle-system interactions in disease, ultimately helping better inform nanotherapeutic design.

1.8.2 Analytical challenges resulting from systemic features of brain tissue

There are a couple reasons relevant to this section as to why interpreting MPT data via ML-based or other parallel correlative assessment is challenging. One of which is that the scales of measurement are starkly variable. At the particle level, interactions with microstructure and the local fluid environment are captured on the millisecond scale. Short-range interactions between particles and ECS structure, such as cell membrane undulations or gyration forces of polymer chains, happen at even shorter timescales. Videos may be collected over several minutes, and the biological basis for the experiment could happen over hours to days. Secondly, ML models and even correlations rely on robust controls or "ground truth" states. Ground truths do not yet exist for particles diffusing in brain tissue, although good agreement has been observed between particles of similar sizes diffusing in a variety of brain environments, such as *ex vivo* human tissue, *ex vivo* rodent tissue, and the *in vivo* mouse brain[75,77]. However, when it comes to training ML models or basing correlations, the default control is "healthy" tissue that does not receive the stimulus that is trying to be predicted.

It's also difficult to simulate particle diffusion data in the brain because these models rely on knowledge of the polymer physics of brain microenvironmental structures, which are not well-characterized. For example, the Amsden obstruction-scaling model is born from the hydrogel field to characterize pore-size distributions in hydrogels using the probability of a particle to diffuse through a channel of a specific radius, and requires parameters such as equivalent bond lengths of monomers, the Flory-Huggins polymer-solvent interaction parameter, and other polymer-specific proportionality constants that are not documented for brain tissue[78]. With one particle size alone in brain tissue, the Amsden computation of pore size distribution is heavily biased to the size of that particle. However, if multiple sizes of particles are tracked, the model can be fit to estimate the constants and therefore compute the size distributions of nanoparticles in that medium, which Nance et al. accomplished to show that the majority of pore sizes in brain tissue range from 25-220 nm[77], a finding which has been validated by others using alternative methods[79].

1.8.3 Challenges from data sampling and acquisition in MPT datasets

The lack of ground-truth, control data regarding probes diffusing in brain tissue also presents a challenge during data acquisition because trajectories from a given region of interest can generate quite a range of diffusion values despite being tracked in functionally the same tissue. The reality is that diffusion measurements in brain tissue can vary quite significantly video-to-video, as a function of the sampling field of view, and the time at which they are captured, in addition to other physical and biological variables. Therefore, a researcher collecting MPT videos in the brain or other biological environment could retroactively discard or clean data that does not align with reported values for control diffusive behavior, but this would introduce bias. Rather than avoid bias, we suggest studies to understand and quantify where variability in MPT data outputs originates. One source of perturbation to MPT data outputs can come from spatial or temporal sampling within fields of view (FOVs) of various sizes. Here, in the same location of an OWH brain slice, two confocal images at 40 x magnification and 100 x magnification were collected, then three videos were randomly sampled within each magnification's FOV. In a single measurement, it can be observed that particle diffusion data can vary significantly depending on the total area of the FOV wherein videos are sampled, with there being less variability in a smaller 100 x magnification FOV compared to a 40 x magnification FOV (Fig. 1.2).

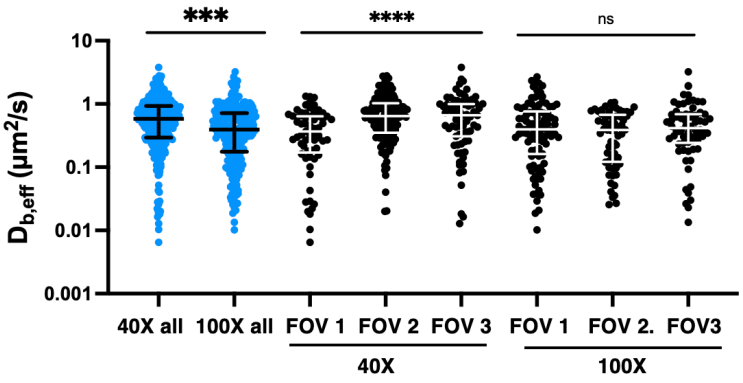

Figure 1.2. Brain effective diffusion coefficients ($D_{b,eff}$, $\mu m^2/s$) of 40 nm PS-PEG nanoparticles in OWH brain slices aggregated across all trajectories (blue) sampled from each imaging trajectory, and then split by diffusion coefficient of each individual sampling location. Data points represent individual trajectories. All videos acquired at 100 fps and 100 x magnification. Kruskal-Wallis tests with non-Gaussian distributions were used with a significance cutoff of $p < 0.05$ were used for statistical comparisons, done in GraphPad prism.

Additionally, as particles constantly move in and out of frame, especially as they are subjected to a wide range of particle-system interactions, time-series data of trajectories imaged in the same locations also show variability. In another FOV, smaller-size (512 px^2) videos were sampled over time in the same locations (termed 'reps') within at least three independent random locations (V1-3) of the same area at 40 x and 100 x magnification (Fig. 1.3).

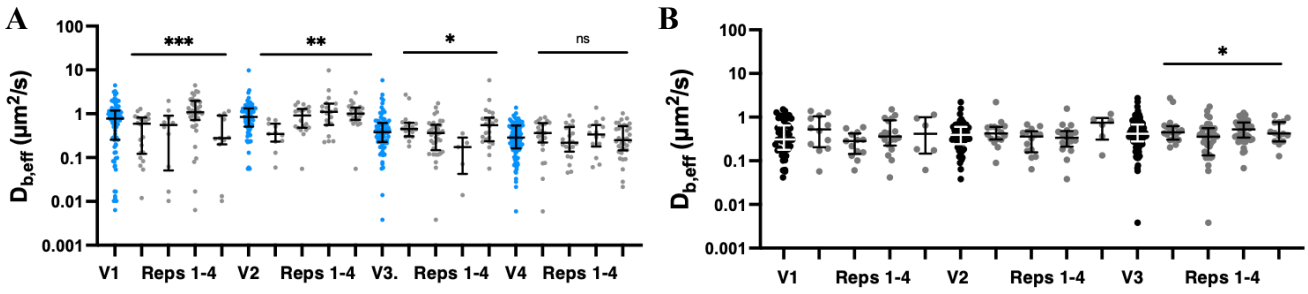

Figure 1.3. Brain effective diffusion coefficients ($D_{b,eff}$, μm^2/s) of 40 nm PS-PEG nanoparticles in OWH brain slices, taken as a time-series in random locations of (A) 40 x imaging field of view and (B) 100 x imaging field of view. For both plots, each V designates an independent video taken in a random location at 1024px^2 and each rep is a 512px^2 video taken in the same location. Data points represent individual trajectories. All videos acquired at 100 fps and 100 x magnification. Kruskal-Wallis tests with non-Gaussian distributions were used with a significance cutoff of $p < 0.05$ were used for statistical comparisons, done in GraphPad prism.

The effect of time-based sampling is substantial when locations are randomly sampled from a larger area, and more controlled when locations are randomly sampled from a smaller area. Regardless, each V1-3 represents the same x,y position between the 40 x and 100 x images, demonstrating that very different values can be collected and that particles fluctuate in and out of frame significantly over a few minutes in a way that can also influence the data output. Furthermore, this is not an inherent property of MPT video acquisition but more a reflection of sampling in active biological systems like *ex vivo* brain slice. A controlled sample with direct inference of system physical properties from particle data, such as glycerol in water, shows spatial and temporal sampling produce consistent outputs independent of system viscosity (Fig. 1.4).

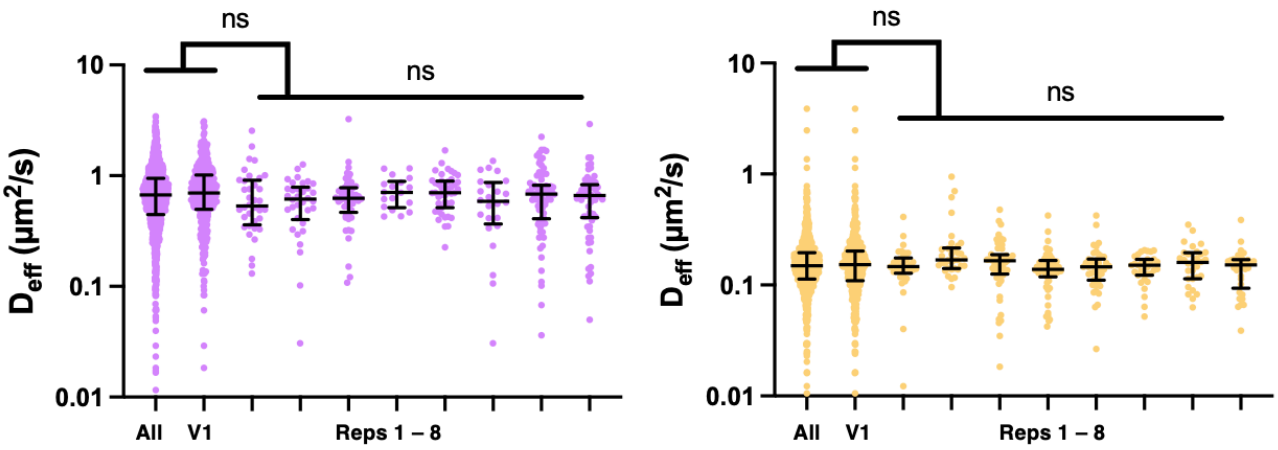

Figure 1.3. Effective diffusion coefficients (D_{eff}, μm²/s) of 40 nm PS-PEG nanoparticles in glycerol/water solutions at 22°C, taken in (left) 50% glycerol/water and and (right) 75% glycerol/water. "All" represents all data points from every 1024px² video taken in one well of an 8-well chamber slide, V1 represents the data from a single 1024px² video, and reps 1-8 are the time series of 512px² videos taken over a few minutes. Data points represent individual trajectories. All videos acquired at 100 fps and 100 x magnification. Kruskal-Wallis tests with non-Gaussian distributions were used to compare medians of time-series replicates with aggregate and individual-video diffusion data with a significance cutoff of $p < 0.05$

In glycerol/water solutions of 50% v/v (purple) and 75% v/v (gold), particles sampled at 512 px² over 8 replicates did not vary significantly in between each other, nor with their aggregate 1024 px² FOV (V1) diffusion data, nor with the aggregate diffusion data for the entire sample (across three FOVs). While more data in other systems is needed, we hypothesize that increasing complexity and heterogeneity of the tracking environment increases the sources of particle-system interaction and ultimately causes variation in spot detection, leading to differences in computed diffusion values. In brain tissue, or other biological environments, the diffusion parameters computed from MPT trajectories represent an effective value that accounts for all the various contributions to particle diffusion: viscous interactions from polymer chains, hydrodynamic interactions, steric interactions, electrostatic interactions, adhesive interactions, and any particle-particle interactions. While the degree to which each of these interactions exist in an MPT field of view could make it more difficult to infer subtle biological features from trajectory data alone, they also likely have a strong effect on the probability of true sampling of the space. Ongoing work is quantifying spatiotemporal sampling effects in hyaluronan and agarose systems, as well as combining them to engineer more spatial randomness into the local environment, expecting that system heterogeneity plays a significant

part of how video sampling strategy can influence the results of an MPT experiment. In Chapter 2, there is discussion surrounding possible biological contributions to changes in particle diffusive behavior that were influenced by mitochondrial dysfunction. Unfortunately, inference of driving forces behind diffusion data from parallel datasets such as cell density, microglial density, and microglial morphology did not explain trends in diffusion data based on general hypotheses that more cell-dense or microglial-dense experimental groups would show lower diffusion. These results prompted investigation into multiple aspects of the MPT error analysis pipeline, with the expectation to implement our findings into future MPT experiments in ex vivo tissue.

1.9 Scope and purpose of thesis

In this thesis, we develop and characterize individual and combinatorial models of metabolic disruption in the brain and quantify their responses across a range of relevant length and time scales. In Chapter 2, we first develop an OWH brain slice model of mitochondrial abnormalities in the neonatal brain and demonstrate how the effects of mitochondrial inhibition propagate across time, brain region, and scale, including properties of the ECS measured by MPT[35]. In Chapter 3, we integrate our model of mitochondrial dysfunction with oxygen-glucose deprivation (OGD), a well-characterized model of hypoxia-ischemia. We combine the two injury modalities to demonstrate how mitochondrial dysfunction affects the brain's responses to hypoxia-ischemia, noting that the severity of the OGD response is modulated by the timing of the application of the mitochondrial inhibitor. In Chapter 4, we summarize the state of nano-based methods to characterize the brain extracellular microenvironment[80].

Chapter 2. A rotenone organotypic whole-hemisphere slice model of mitochondrial abnormalities in the neonatal brain

Butler, B., Renney, M., Bennett, K., Charpentier, G., and Nance, E.

This chapter was published in full on 14 November 2024 in the Journal of Biological Engineering ***volume 18****, Article number: 67 (2024). DOI: https://doi.org/10.1186/s13036-024-00465-w*

2.1 Introduction

In the brain, mitochondria play critical roles in processes that dictate cell function, communication, and fate[81]. Mitochondria are critical to energy generation and involved in intercellular calcium clearance, lipid biogenesis, radical oxygen species (ROS) regulation, and cell communication[81]. Collectively, all neural cells work intimately to maintain a tightly regulated neurometabolic unit that is responsible for 20% of the body's total energy utilization, which is primarily derived from mitochondrial oxidative phosphorylation[11,12,82,83]. The repertoire of roles mitochondria have in neural cells and the brain's reliance on mitochondrial energy links metabolic dysfunctions to a variety of neurologic conditions, including stress, aging, neurodegeneration, traumatic brain injury, post-traumatic stress disorder, stroke, and neuropsychiatric disorders[16,18,84–89].

While mitochondria are well-studied in adult neurologic injury and disease, less is known about their roles in developmental brain injury, where the energy landscape is vastly different[90]. The size of the developing brain ranges between one-fourth and one-third that of the adult brain and is estimated to utilize nearly twice as much glucose as the adult brain for growth, maturation, synaptic pruning, and restructuring[91,92]. Regional metabolic activity profiles in the developing brain are also complex, temporally nonlinear and varying with gestational and developmental age [93]. At the mitochondrial level, differences in respiratory capacity, electron transport chain protein expression, and recovery of metabolism post-injury are shown to depend on sex and developmental age[20,94–97]. The heightened energy demands of neurodevelopment render the developing brain more sensitive to metabolic disruptions. Moreover, there are several unique avenues by which neonatal populations experience mitochondrial abnormalities. Clinical studies have connected preterm birth, placental lesions, intrauterine growth restriction, intermittent hypoxia, maternal stress, pain, childhood trauma, exposure to pollutants from fine particulates (PM2.5), and

glutamate excitotoxicity with differences in mitochondrial respiratory capacity, density, gene expression, protein expression, and ROS levels[84]. Differentials in mitochondrial dysfunction levels were also reported when accounting for biological sex and maternal ethnicity[84]. Other avenues for mitochondrial abnormality in the neo- natal brain include early-life stress, iron and thyroid deficiencies, and exposure to morphine and caffeine [22,98–101].

Despite the variety of circumstances in which neonatal populations can experience mitochondrial abnormalities, the multi-scalar effects of mitochondrial dysfunction on the developing brain remain largely unexplored and many studies of mitochondrial abnormalities as outcomes of specific injuries and disease states focus on specific brain regions or individual cell types[15,102–110]. Here, we leverage an organotypic whole-hemisphere (OWH) brain slice platform to model mitochondria-driven dysfunction in the neonatal brain. OWH slices reorganize in structure throughout culture and in response to biological stimuli, providing a dynamic system to study the brain environment[25,28,33,37,75]. Moreover, OWH slices provide a balance between experimental throughput and native representation of the brain environment and limit animal-to-animal variability, with the opportunity to generate on average 20 OWH slices per hemisphere. We have demonstrated that OWH slices obtained from postnatal (P) day 10 rats, term equivalent to the human neonate, retain viability and metabolic activity up to two weeks in vitro[75]. This postnatal age and culturing window are well-suited to study healthy and abnormal mitochondrial dynamics in the neonatal brain.

To systemically drive mitochondrial abnormality, we expose OWH slices to low-grade doses of mitochondrial toxin rotenone (ROT), a potent inhibitor of respiratory chain protein Complex I, canonically used to study mitochondrial dysfunction in models of neurodegeneration [111–113]. We use ROT to inflict mitochondrial damage and examine the tissue-level, extracellular, cell-type, organelle, and RNA-level responses to repeat ROT exposure and single ROT exposure in two distinct brain regions over 6 days in culture. Our results high- light severity-, time-, and region-dependent responses and establish ROT exposure in term-equivalent OWH cultures as a model system complimentary to traditional in vivo or in vitro ROT models.

2.2 Methods

2.2.1 Animal work and ethics statement

All animal work was performed in accordance with the recommendations in the Guide for the Care and Use of Laboratory Animals of the National Institutes of Health (NIH). Animals were handled according to approved Institutional Animal Care and Use Committee (IACUC) protocol (#4383–02) of the University of Washington, Seattle, WA, USA. The University of Washington has an approved Animal Welfare Assurance (#A3464–01) on file with the NIH Office of Laboratory Animal Welfare (OLAW), is registered with the United States Department of Agriculture (USDA, certificate #91-R-0001), and is accredited by AAALAC International. Every effort was made to minimize suffering. All work was performed using Sprague–Dawley (SD) rats (virus antibody-free, Rattus norvegicus, IGS, Charles River Laboratories, Raleigh, NC, USA) that arrived at postnatal (P) day 5 with a nursing dam. Before removal from the dam at P10, each dam and her pups were housed under standard conditions with an automatic 12 h light/dark cycle, temperature range of 20–26 °C, and access to standard chow and sterile tap water ad libitum. The pups were checked for health daily. All animal studies for this work were routinely started in the mornings to eliminate any influence of time of day. To eliminate the influence of sex-based differences, all animals used were female.

2.2.2 Preparation of coronal OWH brain slice cultures

Healthy female SD P10-P11 rats were injected with an overdose of 100µL pentobarbital (Commercial Beuthanasia D, 390 mg/mL pentobarbital, administered > 120–150 mg/ kg) intraperitoneally. Once the animal was unresponsive to a toe pinch with twee- zers, it was decapitated with surgical scissors. The brain was removed rapidly under aseptic conditions and submerged in ice cold dissection media consisting of 100% HBSS (Hank's Balanced Salt Solution, no Mg^{2+}, no Ca^{2+}), Thermo Fisher Scientific, Waltham, MA, USA), 1% Penicillin–Streptomycin (Thermo Fisher Scientific), and 0.64% w/v glucose (MilliporeSigma, Burlington, MA, USA). Whole brains were split into hemispheres with a sterile razor blade and sliced coronally into 300 µm-thick sections with a McIlwain tissue chopper (Ted Pella, Inc., Redding, CA, USA). Individual slices were separated in ice cold dissection media using sterile fine tip paint brushes and transferred onto 30-mm 0.4-µm-pore-sized cell culture inserts (hydrophilic PET, CellTreat Scientific

Products, Pepperell, MA) before being placed in a non-treated 6-well plate (USA Scientific Inc., Ocala, FL, USA) containing 1 mL pre-warmed (37 °C) slice culture media (SCM; 50% MEM [minimum essential medium, no glutamine, no phenol red, Thermo Fisher Scientific], 41.75% HBSS [with Mg^{2+}, with Ca^{2+}], 5% horse serum [heat inactivated, New Zealand origin, Thermo Fisher Scientific], 1.25% HEPES [Thermo Fisher Scientific], 0.575% w/v glucose, 1% GlutaMAX Supplement, and 1% Penicillin–Streptomycin). Slices were cultured in a sterile CO_2 incubator (Thermo Fisher Scientific) at 37 °C with constant humidity, 95% air and 5% CO_2. Proper aseptic techniques and standard checks that are published for maintenance of OWH slice cultures were used to avoid contamination through 10 days in culture[31,75]. Media was routinely checked for cloudiness and slices were visually checked daily for changes in transparency, discoloration, swelling, or volume loss. Slice samples that did not meet quality criteria were discarded from studies.

2.2.3 ROT exposure in OWH slices

ROT (MW=394.4 mg/mmol) is initially dissolved in 250 µL dimethylsulfoxide (DMSO) which we define as RDMSO (DMSO containing ROT) at 39.44 mg/mL for a stock concentration of 100 mM. Because the solubility and stability of ROT in aqueous media is limited, stock RDMSO was further diluted in DMSO to 1 mM RDMSO and stored in 15 µL aliquots at—20 °C before further dilution into SCM to make ROT-doped SCM (RSCM, defined as SCM containing ROT). For each exposure, RSCM was always made fresh without exposure to light and limited freeze–thaw cycles. RDMSO aliquots (1 mM) were thawed and diluted into pre-warmed 37 °C SCM at 1:100 to achieve 10 µM RSCM, and further diluted 1:200 for 50 nM RSCM. RSCM solutions were inverted to mix without vortexing. All slices are obtained from P10 female rats; all slices are cultured 4 days to restore viability after tissue ex-plantation. At 4 days in vitro (4DIV), SCM is replaced with RSCM at 50 nM (Fig. 2.1). For the repeat-hit exposure, slices are incubated with RSCM for 2 days and replaced with RSCM at 2-day increments out to 10DIV. For the single-hit exposure, slices are incubated with RSCM for 2 days and replaced with healthy media at 2-day increments out to 10DIV. Our healthy control slices are slices cultured without ROT, with media changes at identical time points.

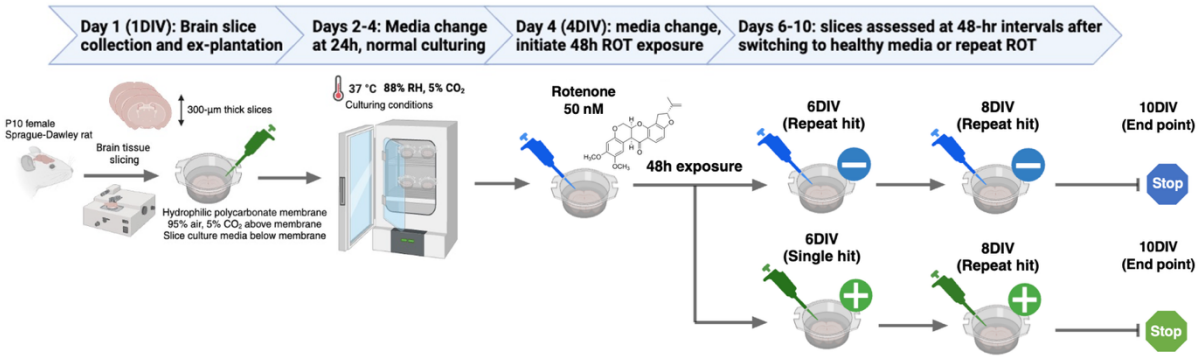

Figure 2.1. Schematic of OWH slice preparation and ROT experimental workflow. 300-µm thick coronal OWH slices are prepared from P10 female rats. Slices are plated on polycarbonate membrane inserts above culture media. Media is changed < 30 min after ex-plantation onto membrane inserts and at 24 h (2DIV) before 48 h of ROT exposure (red pipette). Every 48 h starting at 6DIV, slices are given healthy media (green) or repeat hits of ROT (blue) through 10DIV (end point for single- and repeat-hit exposures)

2.2.4 Lactate dehydrogenase (LDH) assay for whole-slice cytotoxicity

To measure whole-slice cytotoxicity in response to ROT exposure, one brain slice was plated per insert, with 3 total slices per treatment condition. Culture supernatants were collected acutely, at 4DIV, then every 2 days out to 10DIV. At 4DIV, slice media was replaced with 1 nM, 50 nM, 100 nM, or 10 µM RSCM. Supernatants were collected and repeatedly replaced with RSCM every 48 h, which we designate as a repeat-exposure regime with the suffix '-R' following the ROT concentration. All supernatant samples were immediately stored at−80 °C. Supernatant samples were removed and thawed at room temperature to conduct LDH assays (601,170, Cayman Chemical, Ann Arbor, MI, USA). Following the manufacturer's instructions, 100 µL of LDH reaction buffer was added to 100 µL of sample supernatant in triplicate to 96-well plates on ice, and the plates were transferred to a stir plate in a 37 °C incubator. After 30 min, absorbance at 490 nm was measured on a Synergy H1 multimode microplate reader to detect the production of colorimetric formazan. Background absorbance readings of 200 µL SCM (no LDH reagent added) were subtracted from all absorbance values.

2.2.5 Propidium iodide (PI) staining for % cell damage

To measure regional cell death, slices were stained with 1 mL of 5 µg/mL PI (Thermo Fisher Scientific) in SCM for 45 min at standard culture conditions. At the conclusion of each ROT exposure media, ROT media was immediately removed and placed with PI-SCM staining solution. The staining solution was placed underneath the insert. Slices were washed twice for 3 min each with sterile 1xPBS at room temperature, followed by a 1 h wash with 37 °C SCM at culturing conditions, and then formalin fixed for 1 h with 10% formalin phosphate buffer (Thermo Fisher Scientific). Following two final washes with room temperature 1xPBS, slices were stored cov- ered at 4 °C until ready for use. Within 1 week, slices were stained for 30 min with 0.1 µg/mL 4',6- diamindino- 2-phylindole (DAPI; Thermo Fisher Scientific) in 1xPBS at room temperature. Slices were washed twice for 3 min each with 1xPBS prior to imaging. Two-channel 40 × con- focal images (oil immersion, 1.30 numerical aperture, Nikon Corporation, Minato City, Tokyo, Japan) were obtained for PI and DAPI. For every slice, 5–10 images were acquired from both the cortex and midbrain. Image acquisition settings were consistent for all images and conditions. For each image, DAPI+cell nuclei (total cells) and PI+cell nuclei (dead cells) that were also DAPI+were counted manually in ImageJ (NIH) after applying an Otsu threshold and fluorescent cutoff to aid in visualization consistent with image processing methods in prior work[31,34,37,75,114]. The background fluorescent cutoff was kept consistent across all images. The PI + /DAPI + cell ratio was expressed as the percentage of dead cells in an individual image.

2.2.6 Live-slice MitoTracker staining and complex I imaging

To compare mitochondrial responses across healthy and ROT-exposed OWH slices, we leveraged MitoTracker (MT) DeepRed (ThermoFisher M22426, Waltham, MA), a fluorescent probe which accumulates in mitochondria in a membrane-potential dependent manner when staining live tissue. At the conclusion of each time point, live brain slices from P10 female rats were stained with MitoTracker. First, 5 drops of Hoescht NucBlue live nuclear stain are added to 1 mL pre-warmed 37 °C SCM. To add the MitoTracker stain, 1 mM MitoTracker stock solution in DMSO, MitoTracker was diluted to a working solution of 500 nM in pre-warmed 37 °C Hoescht- doped SCM (0.5 µL MitoTracker in 999.5 µL SCM). 1 mL Hoescht-

MitoTracker-SCM was added below the membrane insert and 100 µL was applied on top of each brain slice followed by a 1 h incubation at 37 °C with constant humidity, 95% air, and 5% CO2. Slices were washed once with warmed SCM for 3 min, and then immediately fixed in formalin for 1 h. Following fixation, we washed slices twice in 1 × PBS for 3 min. Next, we co-stained the OWH slices with a complex I antibody (Abcam EPR11521B, Cambridge, MA) at 1:250 dilution in PBS supplemented with 1% Triton X-100 and 3% goat serum overnight at 4 °C. The next day, the OWH slices were washed twice with 1 × PBS for 3 min each time, then were incubated in an AlexaFluor 488 goat anti-rabbit (ThermoFisher Scientific Cat # A11034) secondary antibody solution at 1:500 dilution for 2 h at room temperature in PBS with 1% Tri- ton X-100 before DAPI staining. For confocal imaging, a 10×tilescan of each slice was obtained to provide a representative region map, followed by additional images at 240x (60×lens with 4×zoom) for representative mitochondrial morphology and complex I association. All slice imaging was completed within 1 week of fixation.

2.2.7 Reverse-transcriptase quantitative polymerase chain reaction (RT-qPCR)

RNA was extracted from OWH slices for RT-qPCR, using the protocol adapted from the methods used by Nguyen et al. OWH slices (3 per insert) were cultured on the same membrane with SCM as described[34]. At each specified time point, slices were removed from inserts and were immediately preserved in RNALater (Thermofisher, Waltham, MA, USA) and kept at 4 °C prior to processing to prevent RNA degradation. The RNA from homogenized brain slices were extracted with TRIzol reagent, pelleted at 15,000 × g, washed several times with ultrapure diethylpyrocarbonate (DEPC)-treated water and 70% ethanol, and the RNA final concentration was measured using a NanoDrop. cDNA was diluted to 20 ng/µL with ultrapure RNA-free water. RNA was transcribed into cDNA using Thermofisher (Waltham, MA, USA) Reverse Transcription RNA to cDNA kit. qPCR was run using the transcribed cDNA and BioRad (Hercules, CA, USA) SYBR Green Master Mix that binds to double-stranded DNA to quantitatively track the progress of DNA amplification in real-time. We examined expression of complex I encoding subunit NDUFS-1, SIRT-6 for mitochondrial regulation, MFF-1 and MFN-1 for fission and fusion, BCL-2 and AIFM-1 as mitochondrial apoptotic process markers, and MMP-9 as a probe for protease-driven remodeling of the extracellular

matrix (ECM) (Table 2.1). Tom20 (mitochondrial mem- brane protein) was used as a reference housekeeping gene. The qPCR runs at 95° for 30 s, 95 °C for 5 s, and then 60 °C for 30 s for 40 cycles.

Table 2.1. Genes and associated primers screened with RT-qPCR in ROT-exposed slices.

Role	Name	Description	NCBI Reference	Sequence
Housekeeping	Tom20	Housekeeping gene, mitochondrial biomass	NM_152935.2	F-ACTCCCATTCTTCCACCTTTG R-CCCTGTTGCTGTAGCCATATT
Mitochondrial gene regulation	SIRT-6	Nuclear genes for mitochondrial products	NM_001031649.1	F-TGCCAGCAAGGTTCTTACTAC R-GATGATCTCCTGTGCGACTTT
	MFN-1	Mitochondrial fusion transcription factor	NM_138976.2	F-TCCTCTTCCTCAGTGCTAGTT R-CAGACCGTCCACTTCACATTAG
	MFF-1	Mitochondrial elongation factor 1	NM_130894.4	F-GACAAAGGTGCCTTCAGTAGAT R-CACGGTTCCGGTAGTAAGAAAG
Apoptosis	Bcl-2	Mitochondrial apoptosis regulator	NM_017059.2	F-AGGCGAATTGGCGATGAA R-CTTCTTCCAGATGGTGAGTGAG
	Aifm1	Mitochondria-associated apoptosis inducing factor	NM_031356.2	F-CATACATGCGACCTCCTCTTT R-CACTCCCTCTCGTTTGACTTT
ECM remodeling	MMP-9	Matrix metalloproteinase 9	NM_031055.2	F-CGCCAACTATGACCAGGATAAG R-GTTTAGAGCCACGACCATACAG

2.2.8 Immunofluorescence staining and confocal microscopy of mature neurons and microglia in formalin-fixed OWH slices

OWH slices were prepared, stained with PI, and formalin fixed in the same manner they were for PI staining and imaging studies. Following fixation, OWH slices were incubated with primary antibodies for Iba1 (microglia) or NeuN (neurons). For microglia staining, OWH slices were incubated overnight (16 h) at 4 °C in anti-Iba1 (rabbit anti-Iba, Wako Cat #019–19,741) at 1:250 dilution in 1×PBS containing 1% Triton X-100 and 3% goat serum. The next day, the OWH slices were washed twice with 1×PBS for 3 min each time, then were incubated in an AlexaFluor 488 goat anti-rabbit (ThermoFisher Scientific Cat # A11034) secondary antibody solution at 1:500 dilution for 2 h at room temperature in the same buffer conditions as the primary antibody. For mature neuron staining, OWH slices were incubated overnight at 4 °C in anti-NeuN (rabbit anti- NeuN) at 1:500 dilution in 1×PBS containing 1% Triton X-100 and 3% goat serum and

washed as described for NeuN. Following two 3-min washes with 1×PBS wash, cellular nuclei were stained with a 0.1 µg/mL solution of DAPI in 1×PBS for 30 min at room temperature. Following two 3-min 1 × PBS washes, OWH slices were stored at 4 °C until they were imaged. Two-channel 40×confocal images (oil immersion, 1.30 numerical aperture, Nikon Corporation, Minato City, Tokyo, Japan) were obtained. For every slice, 5–10 images were acquired from both the cortex and midbrain. Image acquisition settings were consistent for all images and conditions. Separate ImageJ macros were run to determine the localization of the AF488 somatic markers with PI+and DAPI+nuclei, keeping identical Otsu thresholding settings used to quantify PI/ DAPI ratios, as well as a 20-pixel size cutoff. The degree of PI+co-localization with the individual cell stains was quantified by dividing the number PI+nuclei associated with the AF488 stain by the number of DAPI+nuclei associated with the AF488 stain.

2.2.9 Nanoparticle preparation and characterization

40 nm fluorescent carboxylate (COOH)-modified poly- styrene latex (PS) nanoparticles (PS-COOH) (Thermo Fisher Scientific) were covalently modified with methoxy (MeO)- poly(ethylene glycol) (PEG)- amine (NH_2) (5 kDa MW, Creative PEGWorks, Durham, NC, USA) by carboxyl amine reaction as previously described and with no changes to prior protocol[115]. The hydrodynamic diameter and polydispersity index (PDI) of the resulting PEG- conjugated fluorescent nanoparticles were measured via dynamic light scattering (DLS) and the ζ-potential by laser Doppler anemometry. Both DLS and laser Doppler anemometry were performed using the Zetasizer Nano ZS (Malvern Panalytical, Malvern, UK). Particles were diluted to~0.002% solids in filtered (0.45 µm, Whatman, Maidstone, UK) 10 mM NaCl, pH 7.0, prior to measurement.

2.2.10 Multiple-particle tracking and analysis in live ex vivo slices

For MPT experiments in live brain slices, one slice was plated per insert (N = 2–3 slices per experimental condition). Particles were tracked in ROT-exposed slices immediately after each exposure window, with all tracking completed within 2 h of the end of the exposure window, including particle incubation time. At the specified timepoints in Fig. 1, SCM was exchanged for 1 mL prewarmed (37 °C) SCM containing 40 nm PS-PEG nanoparticles (100 µg/mL) and Hoechst (5 drops/mL, NucBlue Live ReadyProbes Reagent, Hoechst 33,342, ThermoFisher Scientific). 900µL of nanoparticle-Hoechst-SCM

solution was added below the insert and 100 µL was added dropwise to the top of the slice. OWH slices were incubated for 1 h at standard culture conditions then washed once with 1 mL warm (37 °C) SCM for 3 min each. Following the wash, OWH slices were transferred to an imaging dish and kept in a temperature-controlled incubation chamber maintained at 37 °C, 5% CO_2, and 88% relative humidity during the imaging session. All video acquisition was completed within 1 h. Three videos were collected and quantified from the cortex and midbrain of each slice. Videos were collected at 67 frames-per-second, and 100 × magnification (oil immersion, 1.45 numerical aperture, Nikon Corporation) for 651 frames via fluorescent microscopy using a cMOS camera (Hamamatsu Photonics, Hamamatsu City, Japan) mounted on a confocal microscope. Nanoparticle trajectories, trajectory MSDs, and $D_{b,eff}$ values were extracted from microscopy videos via a lab-developed Python package diff_classifier for parallelized and reproducible MPT workflows as previously described with no change in protocol[68,75,116].

2.2.11 Statistical analysis

All statistical analyses were carried out in GraphPad Prism (GraphPad Software Inc). For all tests run, differences were defined as statistically significant at $p<0.05$, which corresponds to a single asterisk (*) on significance brackets in all figures. Multiple asterisks denote significance values below 0.05, where two asterisks refer to $p<0.01$, three asterisks refer to $p<0.001$, and four asterisks refer to $p<0.0001$. The significance cutoffs apply to statistics in all figures. The D'Agostino-Pearson omnibus K2 test was first used to test for normality for all data- sets (normality QQ plots are provided in Fig. S1-S3). If we were unable to reject the null hypothesis that data were sampled from a population that follows a Gaussian distribution, we either ran an ordinary one-way ANOVA or Brown-Forsythe and Welch ANOVA test, depend- ing on if we could assume equal standard deviations. If we were able to reject the null hypothesis that the data were taken from a normally distributed population, we used the Kruskal–Wallis test for significance. In these instances, we applied Dunn's method to correct for multiple comparisons.

2.3 Results

2.3.1 Culture time drives dose-dependence of the extent of ROT-induced injury in OWH brain slices

Typically, ROT-exposure models involve multiple low- grade exposures over days to weeks to study chronic effects of mitochondrial abnormalities. To first deter- mine if we could sustain ROT-driven injury in our term equivalent OWH slices over longer times without com- promising overall OWH slice health, we measured LDH released from OWH slices during 6 days of ROT expo- sure, starting at 4DIV. Based on evidence that nanomolar concentrations (> 20 nM) are reported to inhibit complex I activity in vitro, exposures for in vitro models range from 1-200 nM, and upper-limit in vitro cytotoxicity levels are reported between 1–20 μM in various models [28,102,105,107,111,117–124], we selected four concentrations to screen overall OWH slice health following repeated exposure (R): 1 nM-R, 50 nM-R, 100 nM-R, and 10 μM-R. From 6DIV through 10DIV, one-way ANOVA of concentration showed that 10-μM-R was the only group to result in significant injury independent of culture time (p<0.05). To demonstrate the effects of ROT concentration and culture time, we performed a two-way ANOVA to show that the effects of culture time, ROT concentration, and time-concentration interaction are all significant (p < 0.0001). After 48 h of exposure (6DIV), all concentrations resulted in significantly higher LDH release compared to healthy control levels (p<0.0001), with the 1 nM-R injury less significant (p < 0.01). At 8DIV, a similar trend was observed where every concentration except 1 nM-R resulted in significantly higher LDH release compared to healthy OWH slices (p<0.0001) (Fig. 2.2A). The 1 nM-R group showed significant injury by 10DIV (p<0.01) but remained closest in value to healthy control levels. By 10DIV, all other ROT concentrations resulted in significantly higher LDH release compared to healthy controls, with 50 nM-R resulting in the most consistent injury relative to healthy OWH slices over the culturing window.

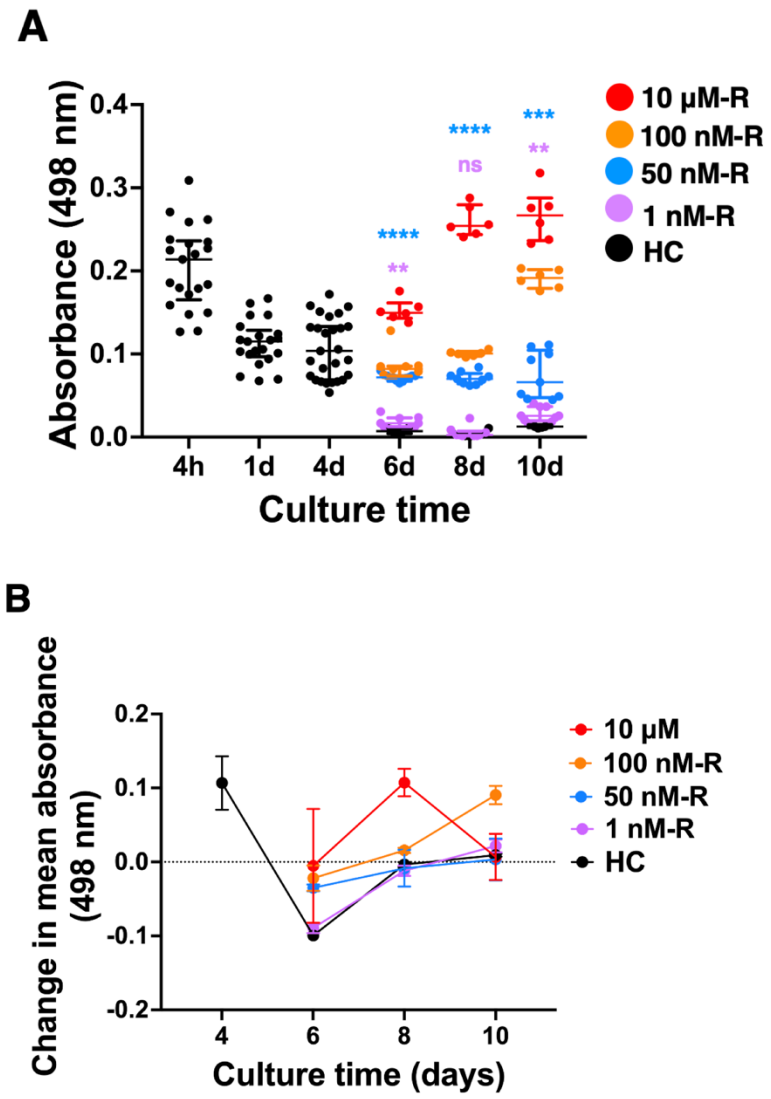

Figure 2.2 Overall OWH slice health in response to ROT measured by LDH absorbance. (**A)** Whole-slice cytotoxicity screening experiment for lactate dehydrogenase (LDH) concentration in supernatants from OWH slices exposed to 1 nM-R through 10 µM-R ROT through 10DIV. Color-coded significance indicators represent ANOVA results for respective ROT concentrations compared against healthy OWH slices from 6DIV – 10DIV. $^{**}p < 0.01$, $^{***}p < 0.001$, $^{****}p < 0.0001$. (**B)** Differential LDH absorbance by exposure level from 4DIV – 10DIV. Data points represent the difference in mean absorbance between time points for each exposure group. Each data point represents a technical replicate (n = 3) from three to six separate OWH slices (N = 3–6)

To better visualize the effect of culture time on the injury profile, we plotted mean differential LDH absorbance between each DIV starting at 4DIV (Fig. 2.2B). We observed that differential LDH release from 1 nM-R and 50 nM-R groups paralleled HC LDH release through 10DIV, but the 100 nM-R and 10 µM-R differential LDH release profiles diverged at 8DIV. Additionally, 8DIV represented an inflection point after

which the change in absorbance was positive. The 50 nM-R exposure level resulted in injury relative to healthy OWH slices with minimal temporal dependence, compared to 100 nM-R and 10 μM exposures. We concluded that 50 nM ROT is an ideal candidate to drive injury in OWH slices through 10DIV, with an inflection response in the whole-slice response occur- ring at 8DIV. We also moved forward with a 10 μM ROT exposure to be used as a positive control or more significant cell death.

2.3.2 ROT exposure alters mitochondrial responses in OWH slices in a regime-dependent manner

After identifying a sufficient ROT exposure level to cause injury but not kill the OWH slice, we qualitatively analyzed mitochondrial morphology, fluorescence-dependent membrane potential, and spatial orientation in ROT-exposed OWH slices at the 8DIV inflection point in whole-slice health following 50 nM-R exposure. We hypothesized that repeated expo- sure to the toxin would result in more morphological and fluorescence shifts from bright punctae to less-fluorescent, dispersed objects with more diffuse signal, as well as less cellular localization of the mitochondria. We did not expect ROT exposure to interfere with the fluorescence of the complex I signal due to the ROT binding site being within the mitochondrial inner membrane, but we did expect more extracellular distribution of complex I signal following changes to mitochondrial integrity due to cell death. Additionally, following the results in Fig. 2.2 and evidence that ROT- driven injury is dose- and time-dependent[117], we incorporated a single-exposure group (S) to compare mitochondrial responses and injury patterns as a function of the number of exposures to the toxin. The fluorescence intensity of complex I did not appear affected by the vehicle but showed more extracellular presence (Fig. 2.3A), likely as a result of cell death. Regional differences were most pronounced following repeat expo- sure in ROT-exposed slices. OWH slices given 50 nM-S exposure showed mitochondrial populations that more resembled healthy OWH slices, evidenced by quantity of nuclei, but with a more heterogeneous distribution of mitochondrial fluorescence.

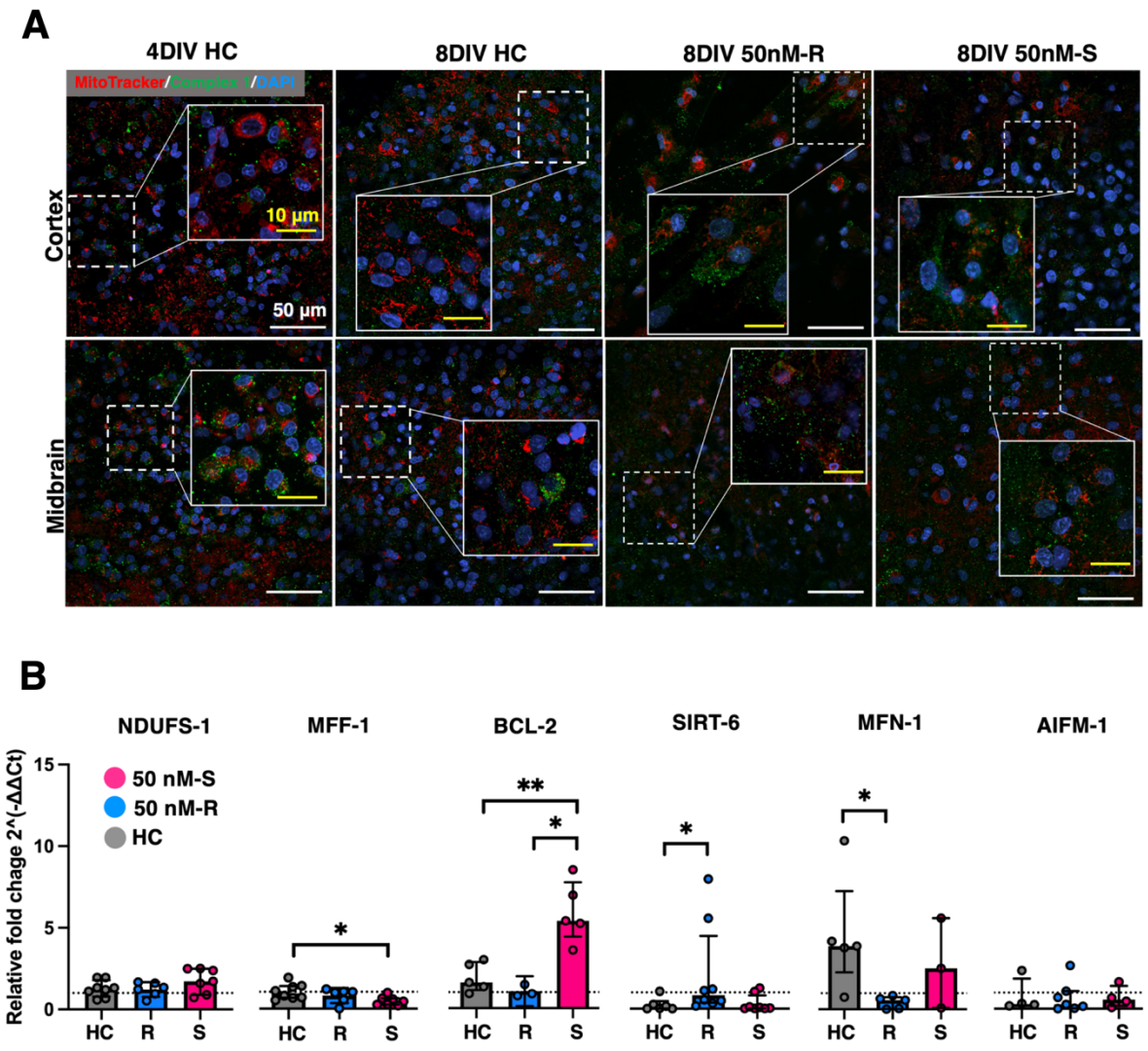

Figure 2.3. Mitochondrial responses during ROT exposure. **(A)** Representative images of live mitochondria (red) in the midbrain of healthy and ROT (50 nM, 10 µM) exposed slices (N=1-2 OWH slices per group, 5-10 representative images taken at 240x magnification in the midbrain). Cell nuclei (blue) are stained with DAPI. Scale bars: 10 µm in all images**. (B)** 8DIV fold change expression relative 4DIV HC samples for complex I, mitochondrial gene regulatory markers, morphology markers, and mitochondrial apoptosis regulatory markers for healthy OWH slices (HC), repeat-exposed 50 nM (50 nM-R), and single-exposed 50 nM (50 nM-S).

We used RT-qPCR to quantify fold changes in expression of genes encoding for complex I (NDUFS-1), mitochondrial fission and fusion (MFF-1, MFN-1), mitochondrial regulatory marker SIRT-6, and mitochondrial- activated apoptosis (BCL-2, AIFM-1). Expression was calculated relative to mitochondrial membrane protein Tom20 as a housekeeping gene to control for anticipated changes in mitochondrial biomass during culturing. Complex I expression aligned with images and showed consistent signal independent of ROT exposure. 50 nM-R resulted in comparable expression relative to healthy OWH slices

(Fig. 2.3B, Table 2.1). While the results were not statistically significant (p=0.322), 50 nM-S resulted in an elevated expression of complex I, which may reflect a compensatory response. We observed lesser expression of fission marker MFF-1 in 50 nM-S OWH slices relative to healthy controls (p<0.05) and upregulation of fusion marker MFN-1 in 50 nM-R OWH slices (p<0.05) which might suggest a shift away from pro-fission states. Repeat exposure did not result in less expression of BCL-2, but 50 nM-S resulted in significantly higher expression com- pared to the HC (p<0.01) and 50 nM-R (p<0.05), which could indicate that the degree of exposure influences the ability to regulate apoptotic markers.

2.3.3 DAPI and propidium iodide (PI) staining captures time-dependent regional changes in cell density and cytotoxicity

After confirming the effects of ROT exposure on whole- slice mitochondrial morphology and RNA expression, we used DAPI, a marker of all cell nuclei and PI, a marker of damaged cell nuclei, to quantify how cortical and midbrain cell populations responded to ROT exposure over time. We first aggregated all data for % cell damage and total nuclei counts for all experimental groups and observed responses that mirrored LDH results (Fig. 2.4A-B). PI/DAPI analysis showed consistent injury through 10DIV resulting from 50 nM exposure. The difference in injury between single and repeat exposure also became more pronounced after 8DIV (p<0.0001). For all DAPI counts, healthy OWH slices retained higher populations than all ROT groups with the exception of 6DIV. The DAPI profile also revealed an inflection response at 8DIV for 50 nM-S where nuclei increased significantly (p<0.01), an effect which was not seen for 50 nM-R and there was less injury over time for a single exposure. A significant difference in total nuclei between 50 nM-R and 50 nM-S was not observed until 10DIV (p < 0.05).

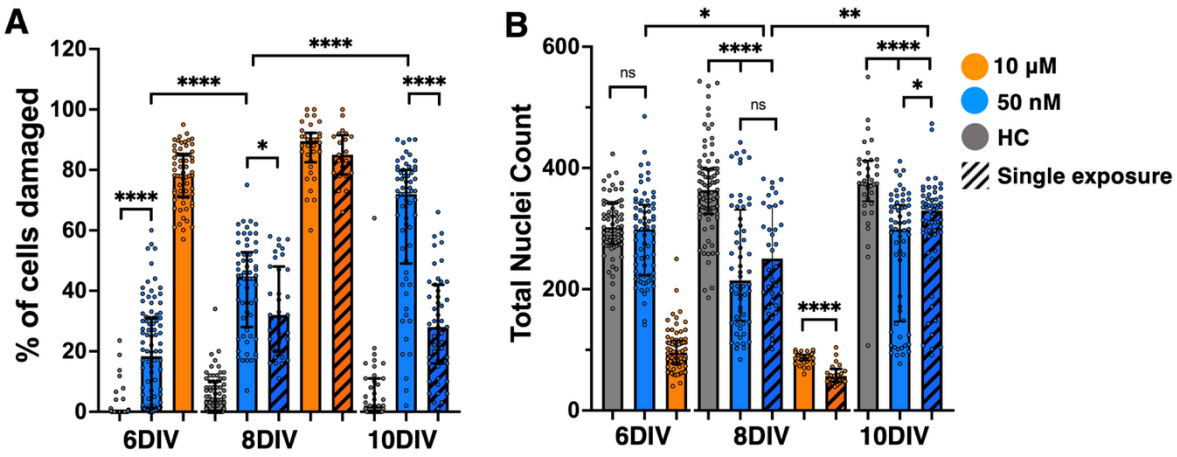

Figure 2.4 Aggregate data from all PI/DAPI experiments. **(A)** % cell damage and **(B)** total nuclei counts for all 40x images taken in the cortex and midbrain of OWH slices in response to 50 nM and 10 µM ROT for single and repeat exposures. Nuclei in images from N=3-6 slices were quantified, and each data point represents the result from an individual image.

To explore the regional responses to number of exposures and expand on the analysis from whole-slice LDH assessments and aggregate PI/DAPI data, we split the data by region. Representative images in each region captured the temporal dependence of cell density and % cell damage in response to ROT (Fig. 2.5A, C). Quantification of % cell damage and total cell counts revealed more subtle regional differences. The degree of injury experienced by cortical cells was consistently higher for a repeat exposure. Cortical cells appeared to recover more strongly by 10DIV (9.5% damaged cells) compared to midbrain cells following a single exposure (40% damaged cells) (Fig. 2.5B). On the other hand, in response to 50 nM-R, midbrain cells experience increasing cell damage through 10DIV (68%), comparable to % cell damage in the cortex (74%), but significantly lower (p<0.05) (Fig. 2.5D). Despite the sustained increase in injury, midbrain cell populations generally outnumbered cortical populations (Fig. 2.5E). 10 µm ROT reduced overall cell density significantly (p<0.0001) with very little slice available for analysis by 10 DIV (Fig. 2.5F). By 8 DIV, both repeat and single expo- sure ROT drove a significant decrease in overall nuclei counts compared to HC.

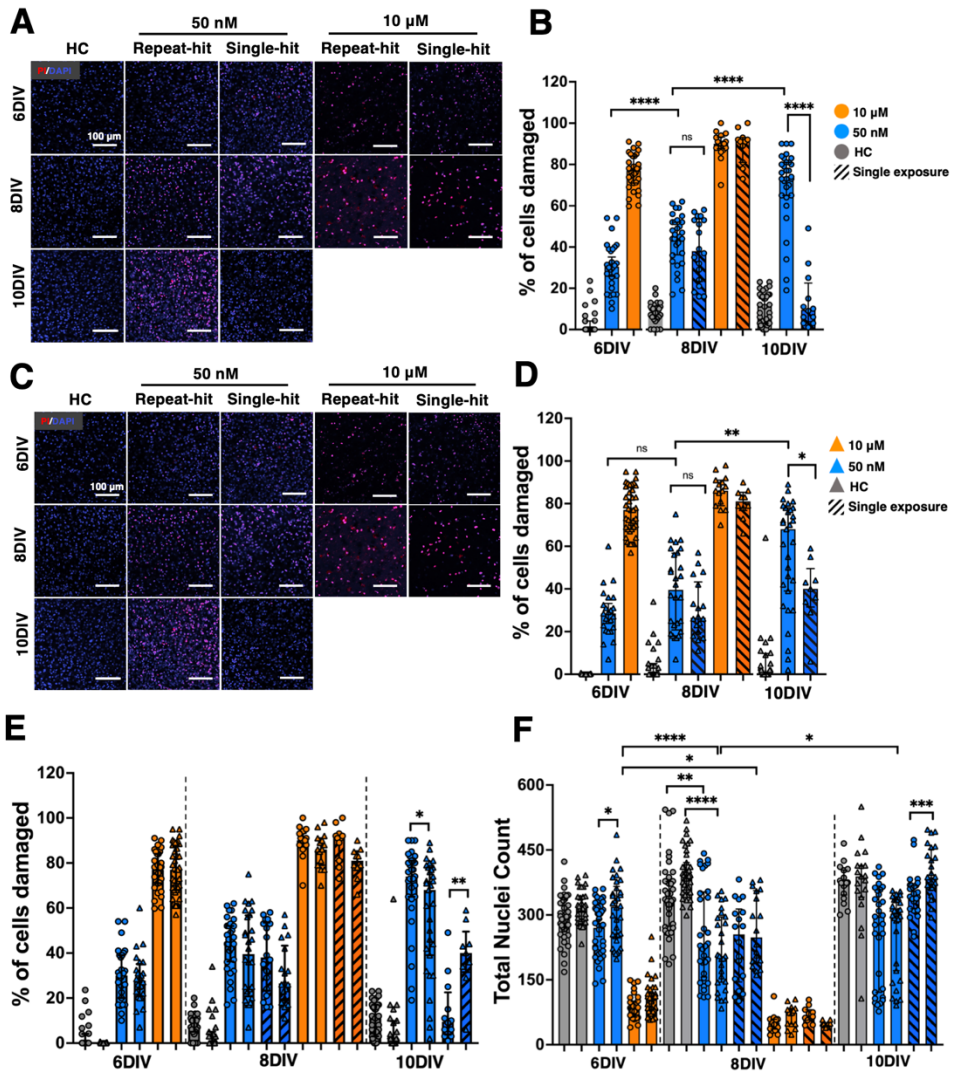

Figure 2.5. Qualitative and quantitative representations of total cell density and percent of damaged cells for all assessment points. PI/DAPI imaging for representative changes in total cell density and distribution of damaged cells in the **(A)** cortex and **(C)** midbrain (N=3-6 slices per condition, n=5-10 images per region per OWH slices taken at 40x magnification). Quantification of percent cell damage in the **(B)** cortex and **(D)** midbrain. Summative regional quantification of total % cell damage **(E)** and number of nuclei counts **(F)** for all groups counted manually in ImageJ following an Otsu threshold and 20-pixel size cutoff. PI-positive nuclei localized to Otsu-thresholded DAPI nuclei were manually counted with a background fluorescence cutoff kept consistent across all experimental groups.

2.3.4 Mature neurons and microglia respond differentially and in a spatiotemporal manner in response to ROT exposure

To gain deeper insight into the cellular responses that may be driving these outcomes, we co-stained OWH slices with somatic markers for mature neurons (NeuN) (Fig. 2.6) and microglia (Iba1) (Fig.

7). Representative NeuN images are shown in Fig. 2.6A. Region-dependent neuronal damage was observed as a function of culture time (Fig. 2.6B-C). In both regions, NeuN+/PI+co- localization increased consistently between 6 and 10DIV (p<0.001 for 50 nM-R in both regions) in accordance with PI/DAPI results. Additionally, in alignment with apparent recovery response observed in cortical cells following 50 nM-S, the increase in % damage between 6 and 10DIV for 50 nM-S was less significant (p<0.05). The increase in NeuN+damage through 8DIV was not significant (p=0.3585 in CTX, p=0.4116 in MD), nor dependent on the number of exposures, but we observed regional differences from 8 to 10DIV for both exposure regimes (Fig. 2.6D). While PI+co-localization with NeuN in the cortex was highest at 10DIV for both exposure regimes (77% 50 nM-R, 70% 50 nM-S), the increase from 8DIV was not significant (p=0.092 repeat exposure, p=0.230 single exposure). Only in the midbrain did both 50 nM-R and 50 nM-S drive significant increases in NeuN damage, with slightly steeper increase in response to 50 nM-R (p<0.01 single exposure, p<0.001 repeat exposure). For both exposure regimes, 8DIV is a critical time point during the culturing window beyond which we saw significantly higher PI+/NeuN co-localization in both regions, as well as the effect of number of exposures in the midbrain. A 10 μM exposure resulted in significant NeuN + cell death across both brain regions (Fig. S2.4).

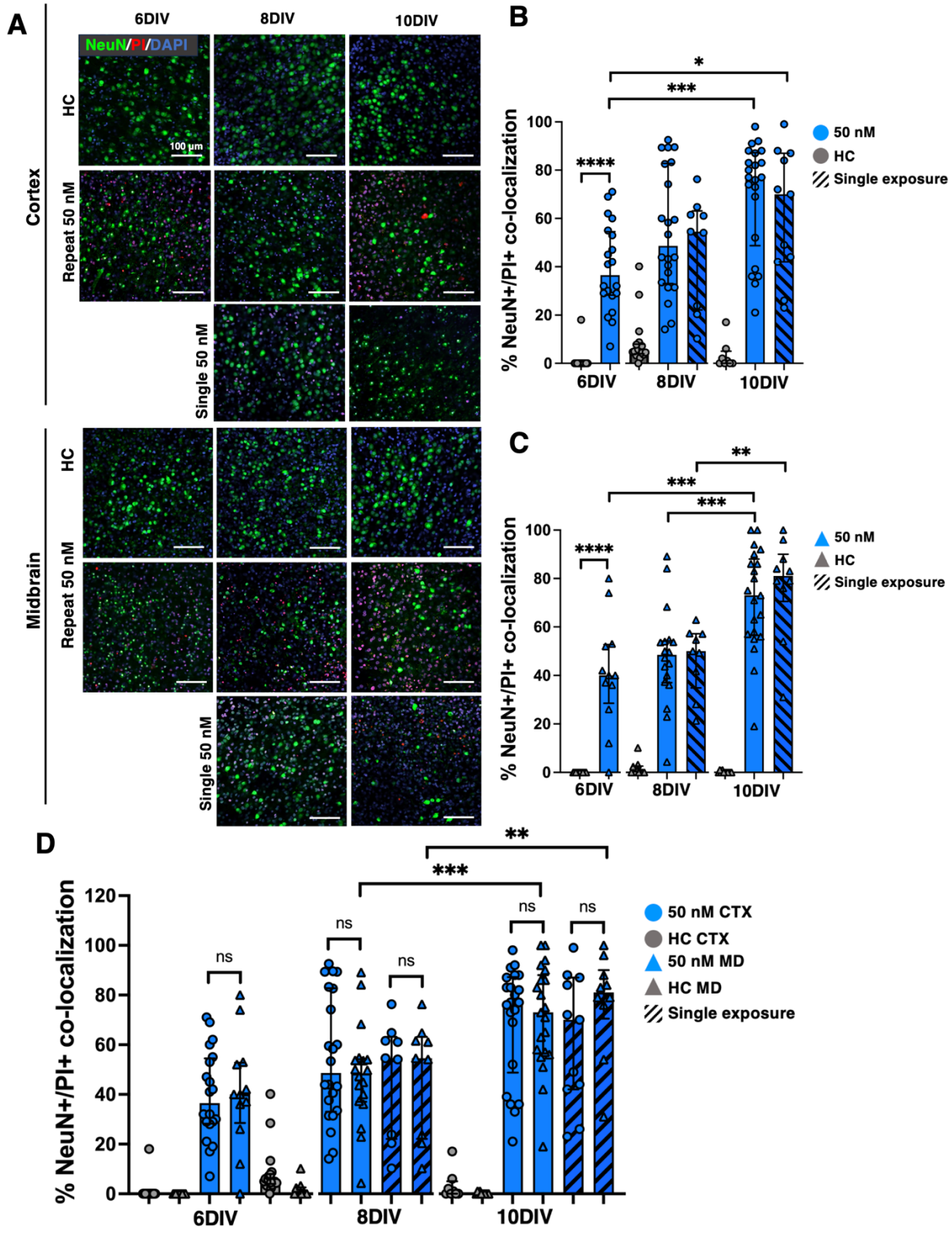
A
6DIV
8DIV
10DIV
NeuN/PI/DAPI
Cortex
HC
Repeat 50 nM
Single 50 nM
100 µm
Midbrain
HC
Repeat 50 nM
Single 50 nM
B
% NeuN+/PI+ co-localization
6DIV
8DIV
10DIV
50 nM
HC
Single exposure
C
% NeuN+/PI+ co-localization
6DIV
8DIV
10DIV
50 nM
HC
Single exposure
D
% NeuN+/PI+ co-localization
ns
6DIV
8DIV
10DIV
50 nM CTX
HC CTX
50 nM MD
HC MD
Single exposure

Figure 2.6. Representative images of NeuN+ neurons in the **(A)** cortex and midbrain of OWH slices (N=2-3 OWH slices used for each treatment group for each cell type, and n=8-12 images taken at 40x magnification per condition in each region). All OWH slices were previously co-stained with PI and and stained with DAPI after the NeuN staining regimen. Quantification of NeuN+ neuron density in the cortex **(B)** and midbrain **(C)** of OWH slices. **(D)** Quantification of PI+/NeuN+ co-localization in the cortex and midbrain of OWH slices.

Through 10DIV, microglia in healthy OWH slices qualitatively displayed heterogeneous morphology with visible branching, reflective of a less inflammatory state, and both regions saw a pronounced shift in morphology to include a distribution of amoeboid cells following ROT exposure (Fig. 2.7A), reflective of a more pro-inflammatory state[125]. The presence of pro-inflammatory phenotypes was dependent on DIV and the number of exposures. At 8DIV, microglia in both regions of OWH slices given 50 nM-R adopted primarily amoeboid distributions, with median circularities 0.599 and 0.567 in the cortex and midbrain, respectively. Microglia OWH slices given 50 nM-S sustained median circularities closer to healthy controls (0.356 CTX, 0.325 MD), and qualitatively showed a more mixed-morphology population similar to healthy controls. By 10DIV, microglia in both regions of slices given a single exposure appeared to shift towards heterogeneous morphology populations more consistent with healthy controls. Quantitative data on circular- ity and aspect ratio of microglial populations confirmed that significant morphological differences separated the midbrain of single-exposure and healthy OWH slices by 10DIV ($p < 0.01$) (Fig. S2.6).

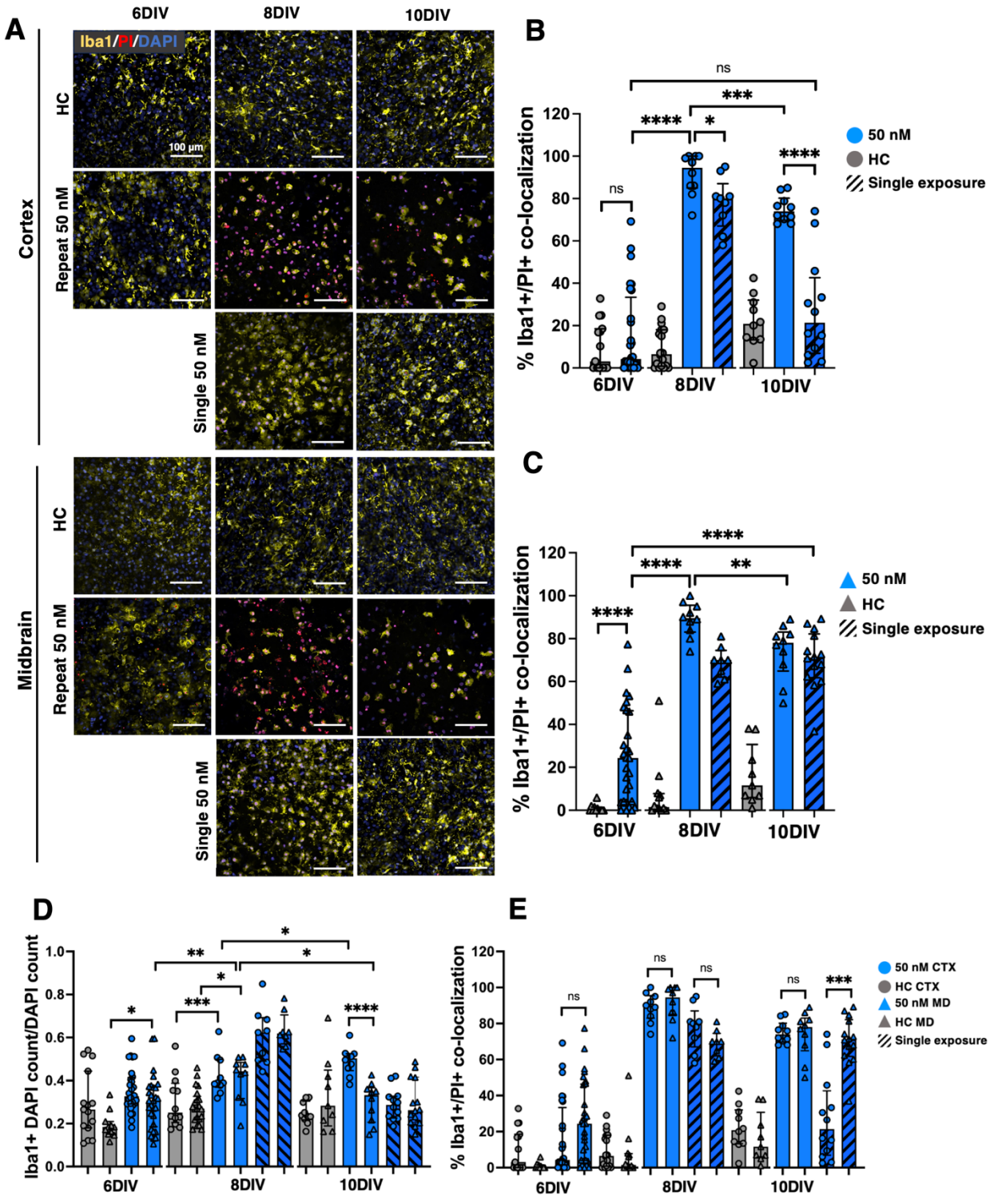

Figure 2.7. (A) Representative images of Iba1+ microglia in the cortex and midbrain of OWH slices (N=2-3 OWH slices used for each treatment group for each cell type, and n=8-12 images taken at 40x magnification per condition in each region). All OWH slices were previously co-stained with PI and stained with DAPI after the Iba1 staining regimen. Quantification of Iba1+ microglia density in the **(B)** cortex and **(C)** midbrain of OWH slices. **(D)** Quantification of Iba1 density (DAPI+/Iba1+ co-localization) in the cortex

and midbrain of OWH slices. **(E)** Quantification of PI+/Iba1+ co-localization in the cortex and midbrain of OWH slices.

Microglial co-localization with PI+nuclei increased significantly by 6DIV in the midbrain (p<0.0001), whereas the cortex was more resistant over the first 48 h of response. By 8DIV, however, both regions saw a com- parable increase in Iba1 + /PI + co-localization independent of the number of exposures (Fig. 2.7B-C). Both regions saw significant decline in Iba1+/PI+co-localization from 8 to 10DIV, although the decrease in the midbrain was less significant (p < 0.01) compared to that observed in the cortex (p<0.001). Within the 50 nM-S group, the regional differences in PI+co-localization over the culturing window were most distinct by 10DIV. Microglial co-localization with PI+nuclei in the cortex recovered through 10DIV (21.4%), while microglia the midbrain sustained more PI + co-localization (71.2%). Additionally, PI+co-localization in the cortex between ROT-exposed microglia at 6DIV and 50 nM-S microglia at 10DIV was close in value but not significant (p=0.0567). The oppo- site was observed in the midbrain, where the midbrain showed significantly higher PI + co-localization by 10DIV following a single exposure (p<0.001) compared to levels at 6DIV (Fig. 2.7E). Generally, microglia in the midbrain retained higher PI + co-localization regardless of the number of exposures. A single exposure demonstrated that cortical microglia initially show stronger resistance and ultimately recovered close to healthy levels, but still experience a peak in PI+co-localization at 8DIV regard- less of the number of exposures. Similar to the NeuN cellular response, 10 μM ROT exposure resulted in high microglial death (Fig. S2.5).

Both regions of ROT-exposed OWH slices displayed elevated microglial densities relative to healthy OWH slices by 8DIV, with 50 nM-S microglial density (0.624 CTX, 0.619 MD) outnumbering those in 50 nM-R OWH slices (0.389 CTX, 0.443 MD). Cortical microglial density increased only slightly from 8 to 10DIV following repeat exposure (+0.115, p<0.05) and decreased significantly by 10DIV following a single exposure (-0.337, p<0.0001), but remained higher than microglial density in the midbrain following repeated exposure (0.332).

A single exposure resulted in a reduction in microglial density by 10DIV, but the reduction was only significant in the midbrain (p<0.01). However, despite the lesser number of microglia, PI+co-localization remained significantly higher in the midbrain by 10DIV. Contextualizing the responses of both neurons and

microglia highlights region-dependent susceptibility and inflammatory changes depending on time in vitro and the number of ROT exposures. Summative tables of median (±IQR) % PI+co-localization of neurons and microglia, as well as microglial density are provided for healthy slices (Table S2.1), single 50 nM ROT exposure (Table S2.2), repeat 50 nM ROT exposure (Table S2.3), and single and repeat 10 μM exposure (Table S2.4). Summative analysis of Iba + , NeuN + , and PI + quantification is visualized in Fig. S2.7.

2.3.5 Extracellular microstructure dynamically and regionally changes as a result of ROT exposure

To characterize steric and micro-viscosity changes in the extracellular microenvironment in response to ROT exposure compared to normal OWH slice culturing, we performed MPT with 40 nm PS-PEG nanoparticle probes at each time point throughout ROT exposure. Nanoparticle probe physicochemical properties are reported in Table S5. Distributions of $D_{b,eff}$ were split by region and plotted over time in response to 50 nM-R and 50 nM-S (Fig. 2.8A-B). In the cortex, the trend in particle diffusion through 10DIV mirrored that which was seen in previous studies in healthy P10 OWH studies[75]. Following 48 h of 50 nM ROT exposure, particles in the cortex moved significantly slower ($D_{b,eff}$=0.230 μm^2/s) compared to those in healthy OWH slices at 6DIV. Quantifying local viscosity in the cortex at 6DIV revealed a more viscous microenvironment following ROT exp o sure, which increased follow ing 50 nM-R at 8DIV ($D_{b,eff}$ = 0.324 μm /s). Particles diffused even slower in OWH slices following 50 nM-S, although particles in the cortex of 50 nM-S OWH slices moved faster at 8DIV compared to their diffusion at 6DIV. By 10DIV, particles in the cortex of 50 nM-R OWH slices showed faster diffusion ($D_{b,eff}$=0.135 μm^2/s) compared to particles in healthy OWH slices.

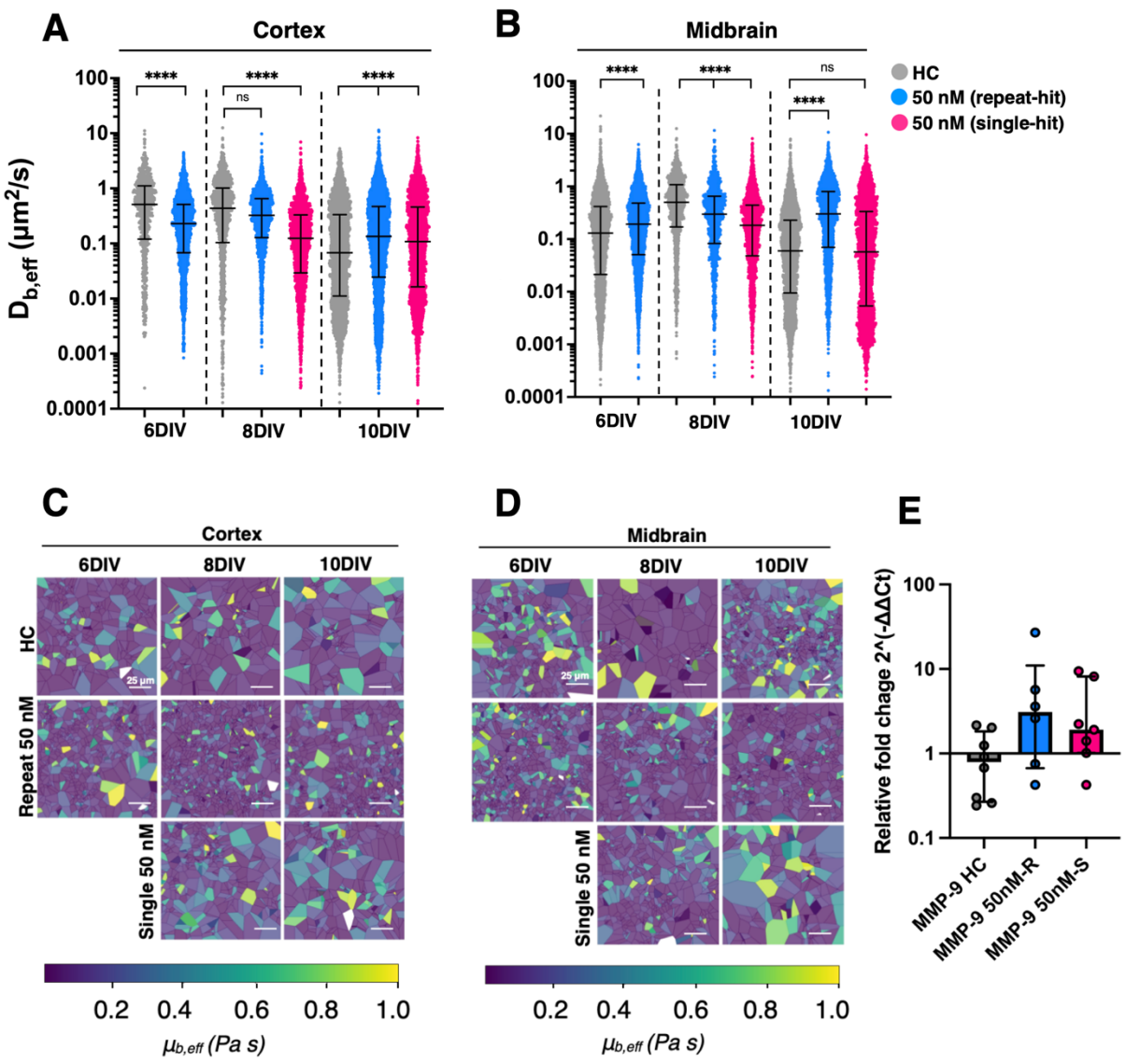

Figure 2.8. Distributions of effective diffusion coefficients ($D_{b,eff}$) comparing particle diffusion in healthy and 50-nM exposed OWH slices through 10DIV in the **(A)** cortex and **(B)** midbrain. Representative mosaic heatmaps of Stokes-Einstein viscosities (Pa s) in the **(C)** cortex and **(D)** midbrain experienced by 40 nm PS-PEG particles at 37°C. Particles were tracked in 2-3 slices per each condition, with 3-5 videos were collected in each region per condition, resulting in > 2,000 trajectories per condition. All videos were acquired at 67 frames per second, 100x magnification, and within 1 hour following particle incubation. Representative effective diffusion coefficients and viscosities are calculated at a trajectory lag time of τ = 0.1 s. Mean-squared displacement profiles from 0 < τ = 1.0s for all groups are provided in supplemental Figure 6. **(E)** Expression of MMP-9 at 8DIV for 50 nM-R and 50 nM-S, as quantified by RT-qPCR, where each data point corresponds to group of three OWH slices pooled together for RNA extraction.

The effect of ROT on particle diffusion in the midbrain was initially opposite that which was observed in the cortex but mirrored the cortex through 10DIV. By 8DIV, particle behavior in the midbrain resembled

the trends observed in the cortex, with slower diffusion for 50 nM-R and 50 nM-S, respectively. Additionally, at 10DIV, not only did the trends in particle diffusion in the midbrain mirror those in the cortex, but the differences relative to diffusion in healthy OWH slices were more pronounced (Fig. S8). Micro-rheology of the local extracellular diffusion environments in each condition, represented as a brain effective viscosity $\mu_{b,eff}$ (Pa s), was calculated (Table 2.2) and visualized using representative mosaic heatmaps. Viscosity calculations revealed a similar trend between both regions for a single-hit exposure, where the increase in viscosity at 6DIV remained relatively constant through 8DIV, but increased sharply at 10DIV. Repeat exposure also resulted in microenvironment viscosity values more consistent with those calculated in healthy tissue at 10DIV.

Table 2.2 Median effective brain Stokes-Einstein viscosities ($\mu_{b,eff}$ x 10^2, Pa s) calculated at a trajectory lag time of τ = 0.1 s with average hydrodynamic diameter 54.8 nm and T = 37°C.

Region	Cortex			Midbrain		
DIV	6DIV	8DIV	10DIV	6DIV	8DIV	10DIV
HC	1.75	2.06	13.2	6.90	1.79	14.9
Single-hit	3.90	7.23	8.23	4.66	3.02	2.97
Repeat-hit	DNC	2.76	6.64	DNC	4.90	15.7

We screened expression of matrix metalloproteinase-9 (MMP-9) at 8DIV in HC, 50 nM-R and 50 nM-S OWH slices to probe the relationship between ROT-driven remodeling of the extracellular matrix (ECM) and particle behavior. We anticipated that that higher levels of the protease would lead to ECM breakdown and lessen steric resistance to diffusion, expected that MMP-9 expression would correlate with particle diffusivity, especially since the particle diffusion pattern in both regions was similar. However, ROT-exposed slices at 8DIV saw higher expressions of MMP-9 in both exposure groups relative to healthy OWH slices despite slower particle diffusion. We observed an increase in MMP-9 expression from 50 nM-R relative to HC OWH slices (p = 0.059) and a slightly lesser increase from 50 nM-S relative to HC OWH slices (p = 0.072).

2.8 Discussion

ROT exposure is commonly used in models of the central nervous system to study the relationship between mitochondrial abnormalities and neurodegenerative pathologies. Emerging clinical evidence also

points to mitochondrial integrity as one mediator of the developing brain's response to stress and injury, and therefore we extended a ROT model framework to neonatal OWH brain slices. To our knowledge, ROT exposure has not been previously investigated in organotypic brain tissue cultures containing multiple brain regions at term equivalency. This study establishes the utility of ROT in OWH slice cultures as a compliment to in vitro and in vivo ROT models, and also demonstrates the exposure regime and time dependence of multi-scalar responses to the mitochondrial poison (Fig. 2.9).

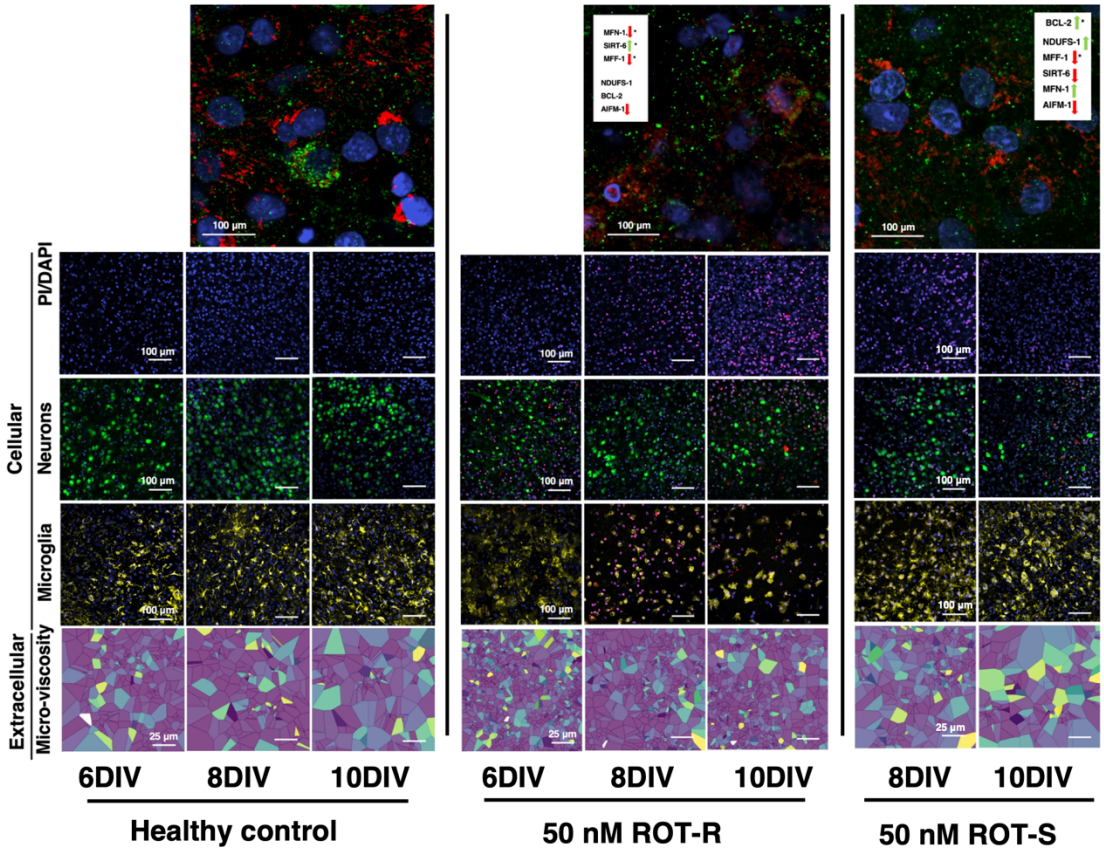

Figure 2.9. Summary of multi-scalar results as a function of culture time and number of 50 nM ROT exposures. Changes in gene expression at 8DIV relative to healthy OWH slices for each experimental group reported in MitoTracker/Complex I images (green arrows = increase, red arrows = decrease, asterisks = significance level). Representative images of aggregate cortex and midbrain data for each measurement below.

Our results showed an injury dependence on both ROT exposure level and culture time. We initially did not expect to see any significant injury from 1 nM ROT because the IC_{50} for ROT-complex I binding in rat brain tissue is reported to range between 8.2 – 19.9 nM, depending on region[83]. We also estimated an

intracellular concentration of at least 10 nM to inhibit complex I based on estimates of complex I levels in astrocytes (2.2×10^5 molecules/cell, 6.6×10^4 μm^3/cell volume) and assuming a 1:1 binding stoichiometry[126,127]. However, at10DIV, the injury from 1nM exposure was significant, suggesting a time dependence. The accumulation of injury resulting from repeated exposure to sub-IC_{50} ROT has also been shown in other model systems[117]. Our LDH results for the 1 nM group parallel these findings. The 50 nM and 100 nM groups showed similar injury levels at 6DIV, which aligns with the similar levels of acute injury (24 h) observed in SH-SY5Y neuron cultures for these exposure levels[122]. The difference in injury between the 50 nM and 100 nM groups diverges significantly between 6 and 10DIV, which highlighted the compounding effects of exposure level and exposure time on ROT injury in OWH slices. The time-dependent injury, despite sub-threshold exposure, may be attributed to ROT accumulation in the lipophilic environment of the mitochondrial inner membrane. While the level of injury from 50 nM expo- sure remained consistent, the relative change in injury from 100 nM exposure increased through 10DIV and approached 10-μM injury levels. Imaging data showing varied distribution of mitochondrial health across injured groups also suggested that our exposure regime was sufficient to drive changes in mitochondria without fully knocking out function. This distinction informed our choice to use 50 nM ROT to explore regional and multi-scale responses in a regime of consistent low- grade injury and utilize 10 μM as a positive control for ROT-driven cell death.

Prior to this study, most in vitro ROT organotypic models focus on individual subcortical structures. We anticipated regional differences due to evidence of region-dependent metabolic activity and region-specific outcomes from mitochondrial impairment[91–93,95,97], which can affect the developing brain through a variety of avenues[20,22,98–101,128,129] . Complex I levels in rat brain tissue are also shown to be region- and cell-type dependent[130,131] and ROT-complex I IC_{50} concentrations vary regionally, with the highest reported in midbrain structures (19.9 nM) [83]. Relative regional susceptibilities have not been extensively explored in culture, but midbrain and striatal tissue homogenates experienced greater loss in glutathione peroxidase activity following ROT incubation compared to frontal cortex and hippocampal homogenates[132]. Therefore, while we expected and confirmed multi-region cytotoxicity profiles would mirror the trends in whole-slice cyto- toxicity data, we also anticipated regional differences. Time in culture defined by DIV accelerated the

regional differences more than any other factor in the change in cell death following single or repeat 50 nM exposure. Through the lens of total cell numbers, culture time also accelerated regional differences and showed an apparent inflection response at 8DIV.

We hypothesized that the tradeoffs been cell numbers and % cell damage may be attributed to the microglial response to neuronal damage, an effect which has previously been shown in vitro[120]. The comparable neuronal cytotoxicity levels between single-hit and repeat-hit ROT over the culturing window might be attributed more to microglial interactions, since microglia are thought to be more resistant to complex I driven injury. ROT promotes reactive oxygen species (ROS) generation directly in neurons and via microglial activation, so we expected initial neuronal cytotoxicity followed by a microglial response and increased neuronal damage over time. We saw this within the first 48 h of 50 nM ROT exposure with comparable neuronal damage between the two regions alongside an increase in microglial co-localization with PI + nuclei. Despite comparable neuronal injury, the mid- brain showed a higher density of microglia, a response that peaked at 8DIV. Interestingly, this time point is also where the inflection responses in neuron cytotoxicity occurred, after which midbrain neurons experienced a steeper increase in injury compared to cortical neurons independent of the number of exposures. The degree of injury between the two regions was not significant, but achieving significant damage within 6 days following 50 nM ROT exposure aligns with a study using organotypic substantia nigra cultures where a single 50 nM exposure comparably shortened dopaminergic neuron processes and changed morphologies after 1 week[117]. While these results indicate that midbrain cells may be more susceptible to ROT exposure at longer culturing times, the interactions driving this susceptibility remain speculative. Microglial densities decreased by 10DIV—more so for a single exposure compared to a repeat exposure— and the remaining microglia in the midbrain retained significantly higher PI+co-localization, suggesting a more lasting effect of the inflammatory response. Further work performing analysis on microglia co-localized with PI using spatial transcriptomics or single cell sequencing techniques could further parse out cell–cell interactions contributing to time-dependent regional differences in cell damage.

Alterations to the extracellular microenvironment are also seen in models of injury and disease states that involve mitochondrial abnormalities. Changes to the extracellular microenvironment can occur

through structural remodeling of the ECM, such as rearrangement, degradation, or deposition, protein expression, fluctuations in local ionic strength and pH, changes in extracellular space volume due to cell swelling, death, proliferation, morphological changes, all of which happen dynamically in healthy and injurious states[64]. Mitochondria play specific roles in activating pathways that result in altered ECS volume and ECM properties, which can affect the behavior of extracellularly diffusing probes. Mitochondrial dysfunction can drive dysregulation of intracellular ion concentrations, which can result in neuronal and glial cell swelling and effectively decrease ECS volume[130]. By 8DIV, there was a morphological shift to a distribution of pro-inflammatory cells in ROT- exposed slices, and an increase in microglial density. This inflammatory shift likely contributes to ECM remodeling through the release of pro-inflammatory cytokines and enzymes like metalloproteinases, further impacting the extracellular microenvironment. Complex I inhibition in vivo is also shown to result in upregulation of ECM- digesting enzymes, such as MMPs 3 and 9[131]. MMPs degrade proteolytic backbones of the brain ECM and can alter the viscous environment experienced by extracellularly diffusing probes, an effect which has been shown in tissue from an in vivo synucleinopathy model[74]. Higher MMP activity in response to ROT could result in an increase in viscosity from increased concentrations of digested or fractionated ECM proteins, an effect we did measure in our MPT studies which could slow diffusion. MMP-9 is well-studied in the brain and has enzymatic affinity towards constituents of the extracellular matrix as well as roles in neural cell adhesion and organization[133,134]. We suspect the latter may help explain why our MMP-9 expression results contradicted our hypothesis, as cytoarchitecture remodeling was likely needed to compensate the microglial responses at this time point. MMP-9 activation can also represent a concerted effort of other MMPs [135] and we chose MMP9 as an initial catch-all probe for the presence of microenvironment- remodeling molecules as it pertains to altered nanoparticle diffusion.

We can assess the change in diffusivity through the lens of cell density, which we expect to show proportionality with effective diffusivity. The decrease in cell density from 6DIV through 8DIV aligns with increased particle diffusivity in both regions, and the recovery of cell density through 10DIV following a single exposure aligns with decreased particle diffusivity over time. Diffusivity trends for repeat exposure are less explained by changes in cell density, where diffusivity continued to increase through 10DIV in the midbrain (but not the cortex) despite nonsignificant changes in cell density. This discrepancy may be

explained by the microglial response from 8DIV through 10DIV. Higher PI+co-localization and density of microglia in the midbrain could explain the regional variability in particle diffusion observed in our study. Microglial density in the midbrain was higher than the cortex, compared to comparable density at 8DIV. Additionally, higher density of microglia with pro- inflammatory morphologies may effectively decrease extracellular volume fraction and correlate with lower particle diffusivity. Disruption to cellular energy metabolism has extracellular consequences, and changes in ECM stiffness can also alter mitochondrial morphology and integrity[40]. Our MPT results in OWH slices supported these findings, capturing differences in tissue microstructure resulting from ROT exposure and mapping these data with cellular and mitochondrial behavior. Changes in ECM stiffness can also alter mitochondrial morphology and integrity[136]. Downregulation of MFF-1 for ROT groups relative to healthy tissue defied our expectations, but we also have to recognize that the timescales of ECM remodeling and RNA expression are likely very different, and standalone expression may not be enough to describe the full state of the system. For example, the upregulation of MFN-1 at the same time point which might suggest a compensatory response, despite a stiffer microenvironment. While there are multiple avenues by which diffusing nanoparticles experience a different microenvironment, these data are limited to descriptive and correlative analysis. Future work could probe causational relationships that contribute to diffusive differences by quantifying hyaluronan fractionation and ECM protein expression, nanoparticle uptake and clearance, osmotic pressure and ionic strength, and cell-specific proliferation [40,52,74,75,137,138].

This study established a complimentary model system to common in vitro and in vivo ROT models to study mitochondrial dysfunction in the neonatal brain with high experimental throughput. We demonstrate the ability of OWH slice cultures exposed to ROT to capture time-, region-, and severity-dependent responses across relevant scales. However, it is important to acknowledge some key limitations of the model and its interpretations. It remains a challenge to synthesize and interpret data collected across a range of length and time scales. The high-throughput nature of the organotypic platform naturally lends itself to focused mechanistic studies to help resolve the length and time scales over which slices recapitulate these functional states. In terms of model design, the scope of these studies does not capture other aspects of mitochondrial responses in the neonatal brain, primarily the influences of sex and developmental age where we might expect different outcomes. Mitochondrial electron transport chain

(ETC) protein expression, respiratory capacity, and susceptibility to oxidative stress is shown to vary with sex, developmental age, and region[97,139]. These characteristics are also shown to be injury dependent. In another study comparing sex differences in neonatal hypoxic-ischemic injury, P8 female rats showed stronger recovery in mitochondrial ETC protein expression following treatment[94]. Other studies generally highlight higher resistance to oxidative stress and less ROS leakage in female rodents, with some hypothesizing higher differentiation in mitochondria as a reason for higher resilience[96]. The decision to use healthy female rats at P10-P11 comes from previously published work[75]. We would expect sex-based differences in response to ROT based on reported sex-based differences in mitochondrial differentiation and electron transport chain protein expression. Therefore, to eliminate the influence of sex-based differences, we only used female tis- sue donors. Future work can incorporate male rats and different postnatal ages into the study design to consider sex-based and age-based differences if it is desired to implement ROT exposure to study therapeutic efficacy of drugs that target mitochondrial regulation in neonates or pediatric populations. While the postnatal age used in this study is well-suited for longer culturing times, we also recognize the limitations in focusing on a single developmental age. Developmental age-based differences should be considered, but for OWH slices specifically, the tradeoff between donor age and long-term culturability must also be acknowledged[75].

Most ROT models study the effects on neurons and how microglial interactions modulate neuronal survival, therefore we chose to focus our studies to these cell types. Microglia are shown to depend more on energy support from mitochondrial oxidative phosphorylation (OXPHOS) compared to other glial cell types[82,140]. However, it is also likely that other neural cells interact with neurons and microglia in ways that contribute to the regional and exposure-dependent differences seen[82,102,127,141]. Future work should consider other cell types, such as astrocytes and oligodendrocytes, when studying neonatal mitochondrial abnormalities or developing cell- targeted treatments. Astrocytes are thought to depend less on OXPHOS and more on glycolytic machinery, rendering them less susceptible to a complex I-based insult[82]. Astrocytes are also known to participate in intercellular transfer of mitochondria, which may be neuroprotective or trigger cell death depending on directionality and the cell types involved[142]. Oligodendrocytes utilize both forms of energetic machinery, but rely more on mitochondrial OXPHOS for the intense energy cost of myelination (3.3×10^{23} ATP/1 g myelin), which position them as an important cell type to study in a regime

of neurodevelopmental mitochondrial dysfunction[143]. However, studying oligodendrocyte response to ROT may be more robust in an OWH slice model with higher white-to-gray matter ratios, such as the ferret or piglet brain. Improved understanding of the roles of multiple cell types in mitochondrial response following complex I inhibition could reveal other avenues for therapeutic intervention and evaluation of mitochondrial performance in developmental brain injury.

2.9 Conclusions

We adapted the complex I inhibitor ROT for driving mitochondrial dysfunction in neonatal brain slices from term-equivalent rodents, focusing on establishing a robust experimental framework using the OWH culture platform. We identified 50 nM ROT as effective dose to induce consistent injury without compromising overall slice health. By 8DIV, we observed distinct responses following a repeat and single exposure of 50 nM ROT that had compounded effects over culture time. Notably, both exposures induced mitochondrial morphological changes and spatial disorientation at 8DIV. Expression at 8DIV of select genes related to mitochondrial regulation, morphology, and apoptosis pathways suggested an effect of exposure level on ability to activate apoptotic pathways and restore morphology. At the cellular level, cortical cells in response to ROT showed sustained increases in cytotoxicity, contrasting with an initially subdued injury profile in the midbrain. Quantifying neuronal damage, microglial localization with damaged cells, and microglial density suggested differences in microglial responses and microglia-neuron interactions that contribute to regional differences in cell damage and density in response to exposure regime and culture time. Behavior of extracellularly diffusing nanoparticle probes also revealed regional, time-, and exposure-dependent differences that can be explained in part by changes in microglial density, morphology, and pro-inflammatory consequences. These findings underscore the complex interplay of region-specific vulnerabilities and time in response to mitochondrial dysfunction. Future research can explore sex and OWH donor age-related variables, other cell types, and mitochondrial oxygen consumption and glycolytic function to enhance our under- standing of mitochondrial responses in the presence of pathology in the developing brain.

Chapter 3. Rotenone disruption of mitochondria increases susceptibility to secondary oxygen-glucose deprivation injury

Butler, B.*, Bennett, K.*, Brandon, OC., Kimerling, J., Schimek, N., Magoon, M. J., Boyle, P. M., and Nance, E.

*authors contributed equally to this work

This work is being prepared for submission to a peer-reviewed journal.

3.1 Introduction

Cerebral ischemia (CI) is a severe neurological injury characterized by lack of blood flow to the brain. CI limits delivery of oxygen and nutrients and disrupting metabolic function, leading to neuroinflammation and tissue death. Nearly 90% of CI cases result in ischemic stroke, with an average mortality rate of 1 in 6 as the fifth leading cause of death and co-morbidity[144]. Risk and mortality rate of ischemic stroke are modulated by lifestyle factors and conditions such as hypertension, obesity, and diabetes[145]. The primary risk factor is age, where mortality rates are much higher for elderly patients, especially for those with pre-existing co-morbidities[146].

Ischemic stroke patients with dementia suffer a mortality rate nearly 4 times higher than stroke patients without cognitive impairment[2]. Another study showed nearly 2 times higher incidence rate of Alzheimer's disease in stroke survivors[144]. Current standards-of-care, such as administration of tissue plasminogen activator or mechanical thrombectomies, target removal of clots rather than systemic factors influencing cell response[144]. There are currently no preventative therapies or curative therapies for survivors that mitigate secondary stroke risk or onset of neurodegeneration. Therefore, understanding the pathophysiology of ischemic stroke in the presence of co-morbidities could reveal new therapies and improve standards-of-care for affected populations.

Cellular metabolism, in the form of mitochondrial function, is a critical aspect of the pathophysiology of ischemic stroke. Mitochondrial dysfunction is well-documented as an acute metabolic outcome and therefore an emergent target for therapeutic intervention following ischemia[87,147–151]. The connections between mitochondrial state and inflammatory responses of microglia are beginning to be unveiled, with multiple studies showing that ischemia-driven mitochondrial dysfunction leads to pro-inflammatory

microglial activation responsible for long-term tissue damage[152,153]. However, it's less understood how pre-existing mitochondrial abnormalities alter this process, despite many of the primary risk factors for ischemic stroke being connected to mitochondrial abnormalities.

One clinical study showed that lower levels of mitochondrial DNA copy number showed to lead to higher stroke risk and worse outcomes, which were also shown to be dependent on age, sex, income of country, and modality of the stroke[23]. Presumably, existing mitochondrial dysfunction could alter ischemia pathophysiology in a few ways. One, the recovery from CI injury could be less effective if mitochondria are unable to produce ATP as well even after oxygen returns, making the recovery more cumbersomects for quantum dots [154]. At the same time, the CI injury, which is known to activate mitophagy, could promote clearance of mitochondria (that are previously inhibited) and allow for fusion of new mitochondria to assist with the response post CI[152]. Regardless, few studies explore how CI-like injury patterns are altered by pre-existing mitochondrial dysfunction. Most studies to date focus on the effect of CI on mitochondria or the role of mitochondrial dysfunction resulting from CI injury in contributing to CI injury outcomes[155–159] . To our knowledge, there is limited analysis on how pre-existing mitochondrial dysfunction alters susceptibility to CI, with one study predicting effects of mitochondrial disorders on stroke outcomes[148].

Therefore, we used an organotypic whole-hemisphere slice model (OWH) of oxygen-glucose deprivation (OGD) to examine how the presence of mitochondrial inhibitor rotenone (ROT) changes the response of OWH slices to OGD injury. OWH brain slices are a useful model for the effects of mitochondrial dysfunction on CI outcomes because they recapitulate regional CI injury patterns shown in vivo, provide access to high-throughput experimentation, and minimize animal-to-animal variability. We first showed that the combined stimuli of OGD and ROT changes cell damage profiles compared to OGD alone, which was dependent on order and timing of the ROT insult. To gain more insight to the combinatorial and time-dependent effects of ROT exposure, we characterized mitochondrial dynamics and levels of hypoxia-inducible factor subunit 1α (HIF-1α) alongside a panel of genetic markers for mitochondrial function, radical oxygen species management, inflammation, and cell death. We found that the gene expression patterns varied differently between longer-term application (24h) or shorter-term application (2h prior, or simultaneously), where shorter-term application resulted in more OGD-like responses. We also quantified pro-inflammatory microglia morphology shifts, noting the most significant changes for shorter-term

exposure groups. Both aligned with mitochondria image-based data specifically for microglia, showing a prominent connection between mitochondrial metabolism and pro-inflammatory activation the closer ROT is applied relative to OGD. This study shows the effect of mitochondrial dysfunction on CI injury patterns and establishes precedent for more investigation with other model systems and the therapeutic benefit of mitochondria-targeting therapies in patients at risk for CI injury.

3.2 Methods

3.2.1 Animal work and ethics statement

All animal work was performed in accordance with the recommendations in the Guide for the Care and Use of Laboratory Animals of the National Institutes of Health (NIH). Animals were handled according to approved Institutional Animal Care and Use Committee (IACUC) protocol (#4383–02) of the University of Washington, Seattle, WA, USA. All work was performed using Sprague–Dawley (SD) rats (virus antibody-free, Rattus norvegicus, IGS, Charles River Laboratories, Raleigh, NC, USA) that arrived at postnatal (P) day 5 with a nursing dam. Before removal from the dam at P10, each dam and her pups were housed under standard conditions with an automatic 12 h light/dark cycle, temperature range of 20–26 °C, and access to standard chow and sterile tap water ad libitum. The pups were checked for health daily. All animal studies for this work were routinely started in the mornings to eliminate any influence of time of day. To eliminate the influence of sex-based differences, all animals used were female.

3.2.2 Preparation of coronal OWH slice cultures

Healthy female SD P10-P11 rats were injected with an overdose of 100µL pentobarbital (Commercial Beuthanasia D, 390 mg/mL pentobarbital, administered > 120–150 mg/ kg) intraperitoneally. Once the animal was unresponsive to a toe pinch with tweezers, it was decapitated with surgical scissors. The brain was removed rapidly under aseptic conditions and submerged in ice cold dissection media consist- ing of 100% HBSS (Hank's Balanced Salt Solution, no Mg^{2+} , no Ca^{2+}) , Thermo Fisher Scientific, Waltham, MA, USA), 1% Penicillin–Streptomycin (Thermo Fisher Scientific), and 0.64% w/v glucose (MilliporeSigma, Burlington, MA, USA). Whole brains were split into hemispheres with a sterile razor blade and sliced coronally into 300 µm-thick sections with a McIlwain tissue chopper (Ted Pella, Inc., Redding, CA, USA). Individual slices were separated in ice cold dissection media using sterile fine tip paint brushes

and transferred onto 30-mm 0.4-µm-pore-sized cell culture inserts (hydrophilic PET, CellTreat Scientific Products, Pepperell, MA) before being placed in a non-treated 6-well plate (USA Scientific Inc., Ocala, FL, USA) containing 1 mL pre-warmed (37 °C) slice culture media (SCM; 50% MEM [minimum essential medium, no glutamine, no phenol red, Thermo Fisher Scientific], 41.75% HBSS [with Mg^{2+} , with Ca^{2+}] 5% horse serum [heat inactivated, New Zealand origin, Thermo Fisher Scientific], 1.25% HEPES [Thermo Fisher Scientific], 0.575% w/v glucose, 1% GlutaMAX Supplement, and 1% Penicillin–Streptomycin). Slices were cultured in a sterile CO_2 incubator (Thermo Fisher Scientific) at 37 °C with constant humidity, 95% air and 5% CO_2. Proper aseptic techniques and standard checks that are published for maintenance of OWH slice cultures were used to avoid contamination through 10 days in culture[75]. Media was routinely checked for cloudiness and slices were visually checked daily for changes in transparency, discoloration, swelling, or volume loss. Slice samples that did not meet quality criteria were discarded from studies.

3.2.3 Oxygen-glucose deprivation (OGD) in OWH slice cultures

OGD media consisted of 120 mM sodium chloride (NaCl, MilliporeSigma), 5 mM potassium chloride (KCl, MilliporeSigma), 2 mM calcium chloride (CaCl2, MilliporeSigma), 1.25 mM monosodium phosphate anhydrous (NaH2PO4, MilliporeSigma), 2 mM magne- sium sulfate (MgSO4, MilliporeSigma), 25 mM sodium bicarbonate (NaHCO3, MilliporeSigma), and 20 mM HEPES in DI water. OGD media was sterile filtered (0.2 µm), titrated to pH 7.4 with 1 M hydrochloric acid (Thermo Fisher Scientific) or 1M sodium hydroxide (Thermo Fisher Scientific), bubbled with nitrogen gas (Praxair, Danbury, CT, USA) for at least 10min, and pre-warmed to 37°C prior to use. To initiate OGD, the SCM supernatant was removed, and each well was rinsed once with 1mL OGD media then replenished with 1mL fresh OGD media. The membrane inserts were then placed back in the well. The 6-well plates with OGD samples were placed in a Hypoxia Incubator Chamber (STEMCELL Technologies, Vancouver, Canada) and placed in a 37°C incubator. The chamber was flushed with nitrogen gas for at least 10min then clamped shut to prevent O_2 from entering. An oximeter was sterile-cleaned and included in the hypoxic chamber to confirm hypoxia prior to starting the timer for OGD. Slices were incubated in the chamber for the remainder of their treatment duration (30 minutes). Following OGD, wells were replenished with 1mL fresh SCM. The 6-well plates were then returned to standard culture conditions. For plates containing inserts with multiple cells per insert, supernatants were collected and assessed using LDH assay. Single-slice inserts were live-labelled for

microglia (at least 5 hours before OGD media conditioning) and mitochondria (one hour before OGD media conditioning) and fixed immediately after OGD.

3.2.4 Rotenone (ROT) exposure for combinatorial injury in OWH slices

ROT (MW=394.4 mg/mmol) slice culture media (RSCM) is prepared as described previously[35]. RSCM at 50 nM is applied topically (200 µL) at five timepoints relative to OGD: -24h, -2h, 0h, and +24h. ROT exposure time is defined as the time after the topical application of ROT to the slice (Table 3.1). Taking care to minimize light exposure and degradation of ROT stock and solutions, 200µL of 50nM ROT in 37°C 25% SCM was made fresh each application and applied topically to each slice with a cut pipette tip to minimize mechanical damage to the slice from application. 200µL of warmed 25% SCM was applied to control slices as a sham at the desired time point.

Table 3.1. Summary of injury groups and abbreviations for each used in the text.

Injury group	Control group	Description
24R + O	24R	ROT applied 24h before OGD
2R + O	2R	ROT applied 2h before OGD
OGD + R	R	ROT applied immediately after OGD
OGD + 24R	24R	ROT applied 24h after OGD
OGD	--	OGD only injury control
	HC	Healthy controls (no OGD or ROT)

3.2.5 Isolation and characterization of protein fractions from OWH slices

Protein fractions were recovered from phenol-ethanol supernatants of RNA isolations that were obtained using the TRIzol method as reported previously[160]. The phenol fraction (~0.5 mL) was first spun at 12,000xg for 10 minutes at 4°C to separate out any remaining aqueous fraction, which was discarded. Ethanol was added 1:1 to the remaining organic fraction, shaken to mix, and left to incubate at room temperature for 10 minutes before spinning at 3,200xg for 5 minutes to precipitate RNA. The supernatant was collected and transferred to cellulose dialysis bags (MWCO 3.5 kDa) and dialyzed against 0.1% SDS (>100 mL/sample) for 22 hours with changeouts at 16 h, 4h, and 2h. At the final changeout, the supernatant was extracted and discarded, and the globular protein mass was resuspended in 1 mL of solubilization buffer (4 M urea, 0.5% SDS in 500 mM Tris-HCl, pH 8.0). Protein solutions were characterized by a bicinchoninic acid assay (Pierce, product info) by 1:1 dilution in 1% SDS to minimize interference of urea

and Tris-HCl in the BCA assay according to manufacturer instructions on diluent compatibilities. A standard calibration curve was obtained and utilized to calculate protein concentrations.

3.2.6 Dot-blot immunodetection of Complex I in OWH slice protein fractions

PVDF low-fluorescence intensity membranes were cut into small squares and 3-4 mm circles were drawn with pencil then traced with a hydrophobic pen to limit sample spreading in between lanes corresponding to individual samples. Separate squares were used for the different groups for the primary antibody anti-Ndufs1 (Abcam). Membranes were soaked in 100% methanol at room temperature for 1 minute, washed in DI water for 5 minutes, then left in TBST buffer until proteins were ready to load. Protein samples were diluted to equal concentrations and 2 µL sample (~1 ug protein) were pipetted into the circles to maintain the same protein mass for all blots. After adding samples, membranes were allowed to dry completely (1.5 h). Prior to blocking, dry membranes were soaked again in 100% methanol for 1 minute then replaced with a 5% skim milk TBST blocking buffer for one hour at room temperature. Following blocking, membranes were soaked membrane-side down in parafilm-covered Petrie dishes overnight at 4°C in primary antibody solution (1:500) diluted in 5% skim milk TBST. After primary incubation, blots were removed by three 5-minute washes with TBST at room temperature. Membranes were then transferred to new Petrie dishes with secondary antibody solution (1:4000) membrane-side down for 1.5 h at room temperature on a shaker. Membranes received three 5-minute TBST washes prior to imaging (Azure biosystems).

3.2.7 Live-labeling of mitochondria and microglia in OWH slices

Microglia and mitochondria in all OWH slices were labeled live prior to fixation and secondary staining. To stain microglia, anti-rat Cd11b-FITC (BioLegend) was diluted 1:200 into SCM and allowed to incubate in live slices for at least four hours (1 mL beneath, 100 uL topically). Following Cd11b-FITC labeling, slices were washed 1x with SCM for 3 minutes then replaced with new staining media containing 500 nM MitoTracker DeepRed (1 mL beneath, 100 µL topically). Slices were washed once again with SCM for 3 minutes then immediately fixed in formalin for one hour at room temperature. Slices were washed 2 times with PBS for three minutes each prior to storage at 4°C, covered from light.

3.2.8 Lactate dehydrogenase (LDH) assay for whole-slice cytotoxicity

To measure whole-slice cytotoxicity, 2-3 brain slices were plated per insert with 1 mL 25% SCM below the membrane, with 6 total slices per treatment condition. Culture supernatants were first collected 24h before the OGD time, the day of OGD for all groups that would receive injury, and then 24h after the OGD time for all groups. Supernatants were stored at -80°C until all samples were ready for analysis. Supernatant samples were removed and thawed at room temperature to conduct LDH assays (601170, Cayman Chemical, Ann Arbor, MI, USA). Following the manufacturer's instructions, 100 µL of LDH reaction buffer was added to 100 µL of sample supernatant in triplicate to 96-well plates on ice, and the plates were transferred to a stir plate in a 37 °C incubator. After 30 min, absorbance at 490 nm was measured on a Synergy H1 multimode microplate reader to detect the production of colorimetric formazan. Background absorbance readings of 200 µL SCM (no LDH reagent added) were subtracted from all absorbance values.

3.2.9 Quantitation of % cell damage from nuclei in formalin-fixed OWH slices

OWH slices were fixed for 1 hour in 10% formalin phosphate buffer (Thermo Fisher Scientific), stained with 4′,6-diamidino-2-phenylindole (DAPI), stored, and imaged as described previously. DAPI-stained OWH slice images were analyzed using a previously described custom Python-based pipeline for automated nucleus detection and pyknotic classification[39]. Briefly, images were preprocessed by intensity normalization and high-pass Gaussian filtering, followed by nucleus detection using the Laplacian of Gaussian method. Eight morphological and intensity-based features were extracted for each nucleus, and a random forest classifier trained on independent manually annotated datasets was used to identify pyknotic nuclei. Full methodological details, including image processing parameters and classifier development, are provided in our earlier work[34]. Cell nuclei were separated into three categories based on morphometric features and fluorescence intensity: healthy, abnormal, and pyknotic. Percent cell damage in each image was quantified as the number of pyknotic and abnormal nuclei divided by the total number of nuclei.

3.2.10 Reverse-transcription quantitative polymerase chain reaction (RT-qPCR)

RNA was extracted from OWH slices for RT-qPCR with methods described previously[34]. At each specified time point, slices were removed from inserts and were immediately preserved in RNALater (Thermofisher, Waltham, MA, USA) and kept at -20 °C prior to processing to prevent RNA degradation. The

RNA from homogenized brain slices were extracted with TRIzol reagent, pelleted at 15,000 × g, washed several times with ultrapure diethylpyrocarbonate (DEPC)-treated water and 75% ethanol, and the RNA final concentration was measured using a NanoDrop. RNA was transcribed into cDNA using a Thermofisher (Waltham, MA, USA) Reverse Transcription RNA to cDNA kit. cDNA was diluted to 20 ng/μL with ultrapure RNA-free water. qPCR was run using the transcribed cDNA and BioRad (Hercules, CA, USA) SYBR Green Master Mix that binds to double-stranded DNA to quantitatively track the progress of DNA amplification in real-time. We examined RNA expression of markers for two panels: we surveyed a panel of inflammation and cell death markers (PARP-1, TNF-α, caspase-3, HIF-1a, housekeeping gene GAPDH) and mitochondrial markers (MFF-1, MFN-1, NDUFS-1, BCL-2, FIS-1, MT3, housekeeping gene Tom20) (Table 3.2). The qPCR runs at 95° for 30 s, 95 °C for 5 s, and then 60 °C for 30 s for 40 cycles. All primers were run in duplicates across samples where Cq values were averaged, and wells that did not show amplification were not included in averaging.

Table 3.2 Genes and associated primers screened with RT-qPCR in OGD/ROT OWH slices.

Name	Description	NCBI Reference	Sequence
Tom20	Housekeeping gene, specifically for mitochondrial biomass	NM_152935.2	F-ACTCCCATTCTTCCACCTTTG R-CCCTGTTGCTGTAGCCATATT
GAPDH	Housekeeping gene	NM_017008.4	F-GTCAAGGCTGAGAATGGG R-CTGGAAGATGGTGATGGG
FIS-1	Mitochondrial fission transcription factor 1		F-CAAGAGCACGCAGTTTGAATAC R-TCAGGATTTGGACTTGGACAC
MFN-1	Mitochondrial fusion transcription factor 1	NM_138976.2	F-TCCTCTTCCTCAGTGCTAGTT R-CAGACCGTCCACTTCACATTAG
MFF-1	Mitochondrial elongation factor 1	NM_130894.4	F-GACAAAGGTGCCTTCAGTAGAT R-CACGGTTCCGGTAGTAAGAAAG
Bcl-2	Mitochondrial apoptosis regulator	NM_017059.2	F-AGGCGAATTGGCGATGAA R-CTTCTTCCAGATGGTGAGTGAG
NDUFS-1	Complex I genetic encoding subunit		F-AGGAGCTGGCACAGATTTAC R-AGAGTCTCCTAGATGGTCGTATC
MT3	Metallothionein-3		F-TCCTACTGGTGGTTCCT R-GCACACTTCTCACATCCT
HIF1a	Hypoxia-inducible factor subunit 1α		F-TGTGGCTACAAGAAACCG R-TTGATGGATGAGGAATGGG
TNFa	Tumor necrosis factor α	NM_012675.3	F-CCT CAG CCT CTT CTC ATT C R- GGA ACT TCT CCT CCT TGT T
PARP-1	(Poly)ADP ribose polymerase 1		F-TCCCAGAACAAGGACGAAGC R-CCTCACACACGACTCGAACA

Casp-3	Caspase-3	NM_012922.2	F-GAGCTTGGAACGCTAAGA R- CTGACTTGCTCCCATGTAT

3.2.11 HIF-1a imaging for hypoxia quantitation in formalin-fixed OWH slices

Formalin-fixed slices were permeabilized for 1 h in 0.5% Triton X-100 in TBST followed by 30 minutes incubation in blocking buffer (1% BSA , 5% goat serum in TBST) at room temperature. Following permeabilization and blocking, slices were left to rest tissue-side down on 500 µL of H1F1α primary antibody solution (ThermoFisher Scientific, Cat # PA1–16601, diluted 1:250 in blocking buffer) overnight at 4 °C. The next day, the OWH slices were washed three times for 5 minutes each with blocking buffer, then were incubated in 500 µL of an AlexaFluor 488 goat anti-rabbit (ThermoFisher Scientific Cat # A11034) secondary antibody solution at 1:500 dilution for 2 h at room temperature in the same buffer conditions as the primary antibody. Following two 3-min washes with 1×PBS wash, cellular nuclei were stained for DAPI as described previously. OWH slices were stored at 4 °C until they were imaged. Three-channel 40×confocal images (oil immersion, 1.30 numerical aperture, Nikon Corporation, Minato City, Tokyo, Japan) were obtained. For every slice, 5–10 images were acquired from both the cortex and midbrain. Image acquisition settings were consistent for all images and conditions.

3.2.12 Quantitation of MitoTracker object density and nuclear distances

Quantitation of MitoTracker DeepRed object density and nuclear distances were used as image-based assays of mitochondrial state. Because MitoTracker accumulates in live mitochondrial membranes only, number of objects detected in fixed tissue serves as a measurement of active mitochondria in the cell. Distances between MitoTracker objects and cell nuclei serves as a measurement of mitochondrial dynamics, as mitochondria can shift between being nuclear-localized and more dispersed between cells in response to stimuli. For OWH slices that were live-incubated with MitoTracker prior to formalin fixation, images were taken at 40X magnification and processed to identify MitoTracker objects. ND2 images were converted to the tiff image format and split by color channel into red for MitoTracker, green for CD11b or HIF1a (depending on the slice) and blue for DAPI channels. Objects in the MitoTracker channel were segmented into binarized masks by thresholding the image based on pixel intensity. Pixels with an intensity greater than 99% of the intensity distribution for a given image were foreground, and all other pixels were

background and excluded. Foreground objects less than 10 pixels were excluded from the binary mask using the Scikit-Image function remove_small_objects. Objects in the DAPI channel were thresholded as described above.

The distance between objects in the DAPI channels and objects in the MitoTracker DeepRed channel was done by first pre-computing the centroid and ideal radius of each nucleus in the image, assigning each a unique label, and creating a spatial kd-tree of the centroids using Scipy's cKDTree. The centroid and ideal radius of each object in the red channel was calculated, and kd-tree was queried to determine the single nearest nucleus centroid for each MitoTracker object. Multiple MitoTracker objects could be assigned to the same nucleus, but multiple nuclei could not be assigned to the same MitoTracker object. Density (normalized to DAPI count) and relative dispersion (distance between MitoTracker object and nuclei, in microns) of MitoTracker objects was compared between OGD and all other treatment groups. Dispersion was quantified as the centroid distance (microns) between the centroids of all MitoTracker objects and centroids of all nuclei in an individual image.

3.2.13 VAMPIRE analysis of microglial morphometric features

ND2 images were converted to the tiff image format, and the green CD11b channel was extracted. Objects in the green channel were segmented using the Li threshold from Scikit-Image. The Scipy function binary_fill_holes was applied to the output of the Li threshold to fill in holes, and objects less than 71 pixels were excluded from the mask. Masks were saved as tiff files, and an 80:20 split was used to divide images into training and test sets. Visual Aided Morpho-Phenotyping Image Recognition (VAMPIRE) software, written in Python, was used to train a model with 5 shape modes and 50 registration coordinates on the training set of images, and the model predicted the shape modes of the cells in the test set images[161]. Scikit-Image's regionprops function was used to calculate the morphological features of cells within all images.

3.2.14 Statistical analysis

All data were assumed to not be normally distributed, and nonparametric analyses were used. LDH data were analyzed by the Kruskal-Wallis test in GraphPad Prism. Cell death was compared across treatment groups using linear mixed-effects models with treatment group as a fixed effect and a random

effect for slice to account for multiple observations within each slice. Comparison of nuclei properties (σ, average intensity, weighted intensity, total intensity, ideal radius, eccentricity, perimeter, area) across groups was performed using linear mixed models with fixed effects of treatment group and random effects of slice and image to account for repeated measures within a given slice, and multiple nuclei being in an image. Pairwise comparisons used estimated marginal means. Gene expression fold-changes were compared across experimental conditions. Predefined pairwise contrasts (OGD vs. control and OGD vs. each treatment group, as well as ROT vs. each respective combinatorial group) were evaluated using the Kruskal–Wallis test, followed by Dunn's post hoc test with adjustment for multiple comparisons. Differences in microglial morphology were compared across experimental conditions. The Kruskal-Wallis test was used to test for global significance between all treatment groups, followed Dunn's post doc test with Benferrori used to adjust for multiple comparisons. A probability (p) value less than 0.05 was considered significant. Statistical analyses were performed in R Version 4.5.0 (Vienna, Austria) and GraphPad Prism version 10.5.0 (GraphPad software, San Diego, CA, USA).

3.3 Results

3.3.1 ROT-OGD injury increases cell damage compared to OGD alone with time-dependent effects

Prior work subjected OWH slices to individual hits of OGD or ROT to measure cell death and metabolic activity. Here we screened OWH slices for % cell damage for ROT exposure before, during, and after OGD to understand how the mitochondrial toxin changes the response to OGD recovery at 2h, 24h, and 48h post OGD. In the 2h post OGD injury group, we found significant differences in % cell damage resulting from the combinatorial injury slices except for the 2R+O group, but the differences were not distinguishable at this timepoint from the effect of ROT alone. Compared to OGD alone, ROT applied 24h before (24R + O), the same time (ORST), and immediately after (OGD+R) all showed significantly higher % damage ($p < 0.001$, $p = 0.001$, $p = 0.03$, respectively). However, there was the same significant increase in % damage for 24h ROT alone relative to OGD ($p < 0.001$).

In the 24-hour post OGD injury group we found no significance between OGD control and injury conditions or ROT control groups. The OGD control vs OGD+24R group had the highest P-value of 0.843 showing that these two groups are more likely to show a difference due to random variation rather than a

true effect. In the 48-hour post OGD group we found a statistical significance between the OGD control group and -24R + OGD and ORST groups ($p < 0.001$ for both). In the OGD control vs -2R + OGD groups there was a p-value of 0.63 showing that differences between these groups are also more likely due to random variations in the slices than the injury schema.

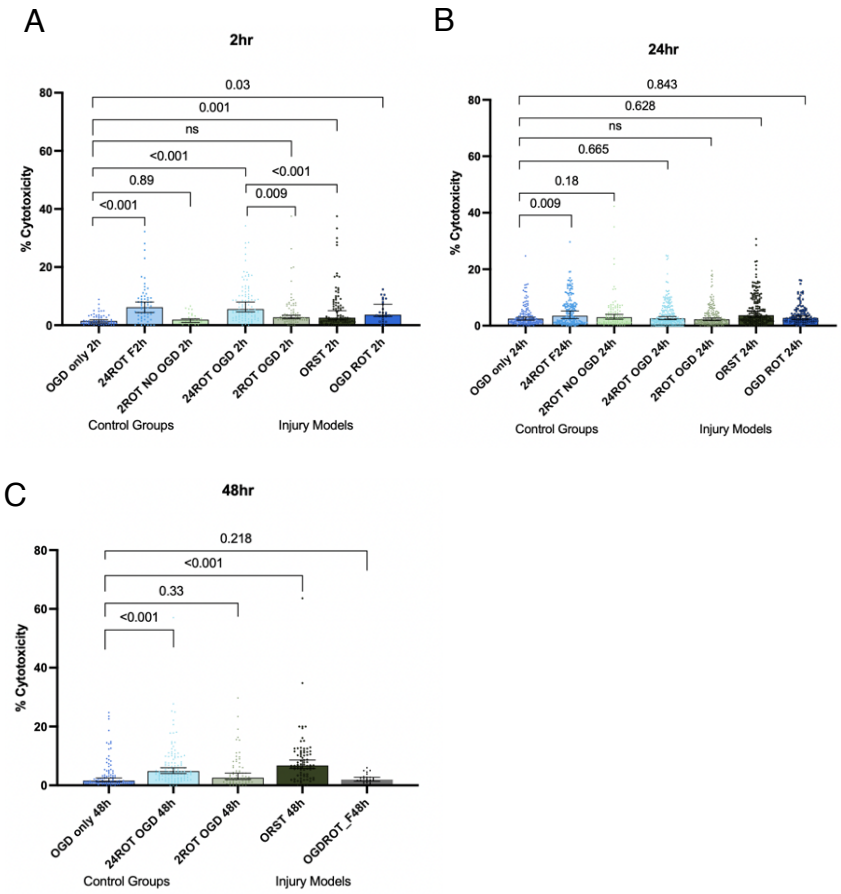

Figure 3.1. Whole-slice % cell damage in response to each injury group at (A) 2h after OGD, (B) 24h after OGD, and (C) 48h after OGD. Each data point represents % of damaged nuclei in an individual image across n=6-12 biological replicates for each group. A linear mixed-effects model with a random effect by slice was performed in R to determine significance, defined as $p < 0.05$.

3.3.2 Mitochondrial properties and cellular response pathways 24h after OGD highlight combinatorial injury effects and show exacerbation of OGD-driven response

Cell damage data highlighted two important aspects of the combined injury scheme that result in a different recovery pattern at 48h: the first being that the combined stimuli change the course of OGD response compared to that of OGD alone, and the second being that there is a time effect of when ROT is applied relative to OGD. To gain more insight into the impacts of combinatorial stimuli affecting OWH slice

response at 48h, we assessed mitochondrial properties and hypoxia levels, two functional variables associated with both injury schemes, in addition to expression of genetic markers for relevant mitochondrial and cell-death processes.

The presence of ROT led to significantly lower relative density of MitoTracker objects for the 2R+O ($p < 0.0001$) and ORST groups ($p < 0.0001$) (Fig. 3.2A). However, the difference between OGD alone and ROT applied 2h before the OGD time without OGD (2R) was not significant ($p = 0.184$). OGD produced higher median distances between nuclei and MitoTracker objects compared to 2R+O, 2R, and ORST groups (all $p < 0.0001$). There were no apparent differences in median distances between 2R and the combinatorial groups ($p > 0.9999$ ORST, $p = 0.5714$ 2R+O). For median distances, whether ROT was applied 2h in advance of OGD or at the same time did not affect relative dispersion of mitochondrial objects, this was affected only by the presence of OGD. OGD produced the highest relative fluorescence of HIF1a fluorescence of all ROT groups, but both 2R+O and ORST groups showed significantly less ($p < 0.0001$) HIF1a fluorescence relative to OGD compared to the difference between OGD and 2R ($p < 0.0397$). However, unlike the trends in mitochondrial density and dispersion, there were significant differences in relative HIF1a fluorescence between 2R+O and ORST compared to 2R ($p = 0.0129$ and $p < 0.0001$, respectively).

The effect of combinatorial injury, as well as differences between ROT and OGD alone, were represented across a panel of genetic markers for mitochondrial dynamics, inflammation, and cell death. While OGD and ROT alone act differently, the effect of the combinatorial injury is most seen between 2R+O and ORST. Generally, 24h after OGD alone, HIF1a is upregulated and mitochondria in a more fission-like state (downregulations of FIS-1 and MFF-1). Apoptotic and inflammatory processes also display downregulation at this timepoint following the injury. ROT alone (2R) also shows HIF1α upregulation (higher compared to OGD, albeit insignificant), but also upregulation of apoptotic and inflammatory processes, and mitochondria in a more fusion-like state (upregulation of MFN-1). 2R+O followed the same pattern of OGD, showing apoptotic and inflammatory downregulation and a fission-like state for mitochondria. ORST showed similar responses to 2R+O for TNFα, PARP, and Casp-3, however showed upregulation of anti-apoptotic BCL-2. Additionally, ORST was the only group that showed upregulation of both fission and fusion markers, as well as complex I-encoding subunits (NDUFS-1).

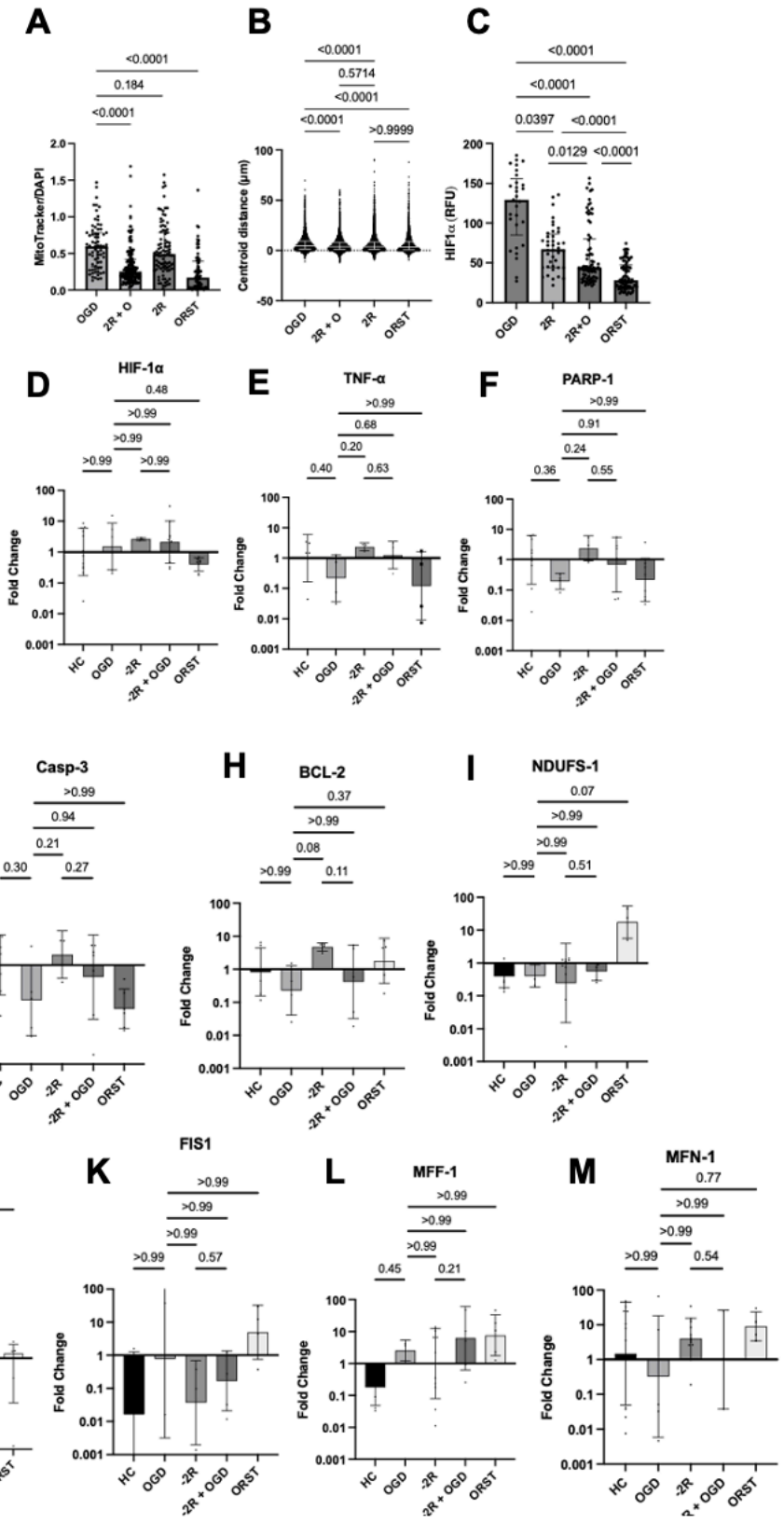
A
<0.0001
0.184
<0.0001
MitoTracker/DAPI
OGD
2R + O
2R
ORST
B
<0.0001
0.5714
<0.0001
<0.0001
>0.9999
Centroid distance (μm)
C
<0.0001
<0.0001
0.0397
<0.0001
0.0129
<0.0001
HIF1α (RFU)
D
HIF-1α
0.48
>0.99
>0.99
>0.99
>0.99
Fold Change
HC
OGD
2R
2R + OGD
ORST
E
TNF-α
>0.99
0.68
0.20
0.40
0.63
F
PARP-1
>0.99
0.91
0.24
0.36
0.55
G
Casp-3
>0.99
0.94
0.21
0.30
0.27
H
BCL-2
0.37
>0.99
0.08
>0.99
0.11
I
NDUFS-1
0.07
>0.99
>0.99
>0.99
0.51
J
AT3
>0.99
0.43
0.37
0.96
0.71
K
FIS1
>0.99
>0.99
>0.99
>0.99
0.57
L
MFF-1
>0.99
>0.99
>0.99
0.45
0.21
M
MFN-1
0.77
>0.99
>0.99
>0.99
0.54

Figure 3.2. Combinatorial group comparison at OGD time. Mitochondrial image-based assessment for (A) density, where each data point represents an individual MitoTracker object in an image and (B) relative nuclear distance (microns), where each data point represents an individual distance between a MitoTracker object and a nearby nucleus and (C) HIF1 α fluorescence where each data point represents absolute HIF1 α signal in an individual image. (D-M) fold-change expression data where each datapoint represents fold-change expression of the marker from RNA pooled from a group of three slices for a total of n=6 RNA samples per group. Image based data and RT-qPCR data were compared using a Kruskal-Wallis test in GraphPad prism to determine significance, defined as $p < 0.05$.

3.3.3 Extending ROT exposure time relative to OGD affects mitochondrial performance more and pro-inflammatory expression less

Comparing OGD to combinatorial injuries around the same timepoint demonstrated that the combination does change the course of OGD response and that the timing does matter. To further investigate the time effect, we analyzed the same responses following a 24h pre-treatment with ROT (24R+O) and compared it to OGD and 24h of ROT alone (24R). Similar to 2R+O, 24R+O also led to a significant decrease in mitochondrial density relative to OGD ($p < 0.0001$). However, this time, ROT alone produced a significant decrease in mitochondrial density as well ($p = 0.0002$), even slightly more so compared to its combinatorial counterpart 24R+O ($p = 0.025$). However, there was no significant difference in median mitochondrial distances between OGD and ROT alone ($p > 0.9999$). OGD generated the highest median mitochondrial distances, however when combined with ROT (24R+O), this generated the lowest distances. In the same fashion as the 2R+O and ORST timepoints, OGD generated higher relative HIF1 α fluorescence compared to 24R+O ($p = 0.0032$) and 24R ($p = 0.0051$), with the combinatorial group showing the lowest relative HIF1 α fluorescence of the three groups.

Gene expression data following longer ROT exposure also showed a different landscape. Both 24R and 24R+O led to downregulation in HIF1α compared to both OGD and 2R exposure, with 24R showing significantly lower HIF1α expression compared to 2R ($p = 0.05$). Inflammation and cell death markers were also generally downregulated, whereas 2R showed upregulations for all. Compared to 24R, although to slightly different degrees, the same trend of downregulation was followed for expression of TNFα ($p=0.06$), PARP ($p=0.14$), and Casp-3 ($p = 0.009$). Anti-apoptotic BCL-2 also showed downregulation for 24R+O relative to 24R, although not quite significant ($p=0.21$). A significant downregulation was seen for NDFUS-1 expression ($p = 0.02$). Downregulation was seen for all genetic markers in response to 24R and 24R+O. The only exception for 24R was MFF-1, showing significantly higher expression compared to 24R+O ($p = 0.05$). The 2R group only showed downregulation of MT3 and NDUFS-1 but to a lesser extent as 24h

groups. With longer exposure time, pro-inflammatory expression was subdued, but mitochondrial performance appears worse.

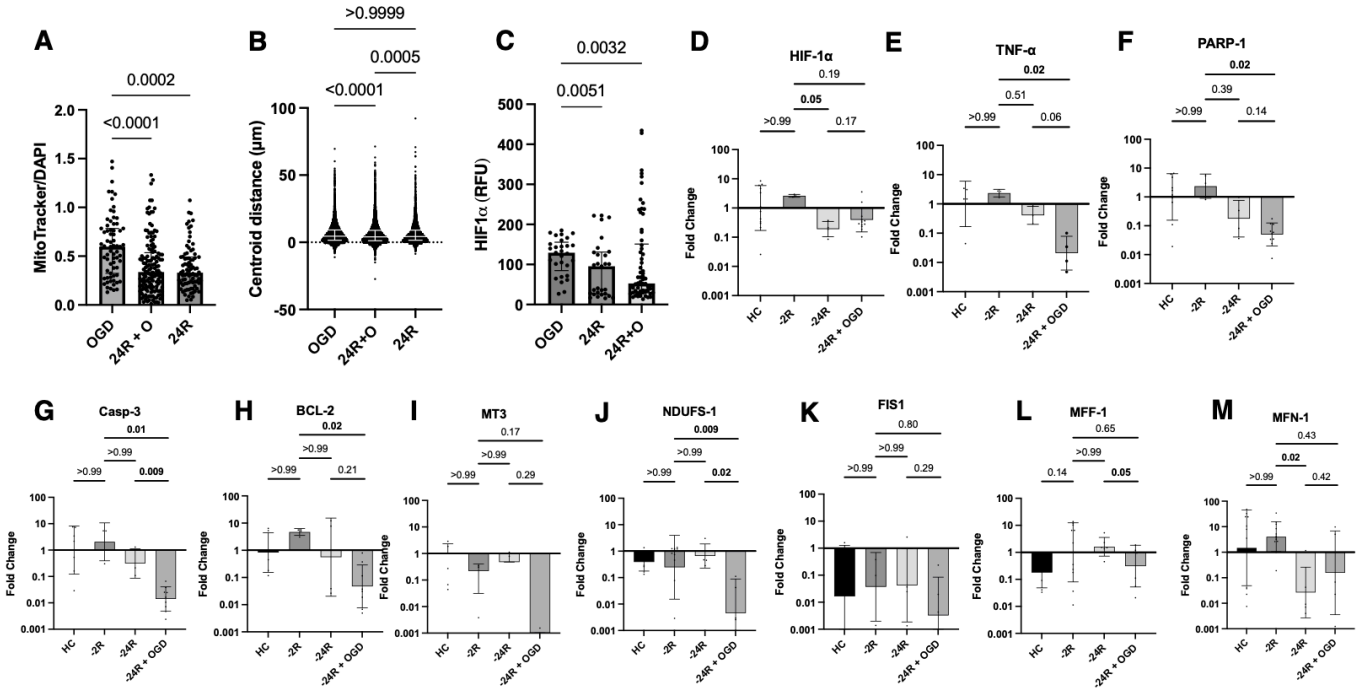

Figure 3.3. Combinatorial group comparison 24h prior to OGD. Mitochondrial image-based assessment for (A) density, where each data point represents an individual MitoTracker object in an image and (B) relative nuclear distance (microns), where each data point represents an individual distance between a MitoTracker object and a nearby nucleus and (C) HIF1a fluorescence where each data point represents absolute HIF1a signal in an individual image. (D-M) fold-change expression data for the panel of primers in Table 3.1 where each datapoint represents fold-change expression of the marker from RNA pooled from a group of three slices for a total of n=6 RNA samples per group. Image based data and RT-qPCR data were compared using a Kruskal-Wallis test in GraphPad prism to determine significance, defined as $p < 0.05$.

3.3.4 Shorter exposure times relative to OGD drive higher pro-inflammatory phenotypic shifts in microglia

The results above highlight a complex inflammatory landscape outlined by differences in mitochondrial dynamics and hypoxia levels, which is modulated by the combinatorial injury schemes. To explore the connection between these results and cell damage, we studied phenotypic trends in microglia as a function of mitochondrial and nuclear state. First, features of microglial morphology were compared between OGD and all injury groups. Using Python-based image processing[161], we computed circularity, area, perimeter, and aspect ratio of microglia live-labelled with Cd11b. We found quantitative differences in

all features across all treatment groups, with area and circularity showing the most significant comparisons. Median perimeter and aspect ratio showed less significant differences between OGD and combinatorial groups. Microglia in the ORST group displayed higher area, circularity, and perimeter. Microglia in 24R+O and 2R+O groups displayed lower values for the same features with less statistical significance. Microglia in the 2R+O group showed the opposing trend in morphometric features relative to OGD, and had more significant changes relative to OGD compared to 24R+O.

Aspect ratio remained unchanged as a function of injury group with the exception of ORST, which showed significantly smaller aspect ratios compared to all other injury groups. Degree of circularity and area were the two morphometric features with the most significant changes between groups. Median microglial area for combinatorial injury was only significantly different than those of OGD only for the 2R+O (lower, $p < 0.05$) and ORST (higher, $p < 0.05$) groups. Only for ORST was median area higher when comparing combinatorial injury to ROT alone, otherwise ROT resulted in lower median areas at each respective combinatorial treatment timepoint. For circularity, only microglia in 2R+O and ORST groups showed significant differences compared to OGD alone, with the 2R+O group showing lower median circularity ($p < 0.05$) and the ORST group showing higher median circularity ($p > 0.05$). The 24R+O group did not show any difference in circularity relative to its ROT-only control, but 2R+O and ORST displayed significantly lower and higher median circularities, respectively ($p < 0.05$ for both). Microglial perimeter displayed very little differences between groups, with 24R+O being the only lower perimeter measured compared to 24R.

When sorting median distances between nuclei and microglia only by microglial nuclei, only the ORST group showed a reduction in median distance compared to OGD and to all other groups. The 2R+O also displayed opposing behavior with slightly higher median distances, but the result was not significant ($p = 0.5367$). All other injury groups showed nearly identical median distances and distributions, with the note that sorting by microglial nuclei showed higher distances compared to all nuclei. In terms of density of MitoTracker objects surrounding microglia, the only groups with significant changes relative to OGD only were 2R+O ($p < 0.0001$) and ORST ($p=0.0028$). In contrast to density of MitoTracker objects surrounding all nuclei, OGD did not produce any significant differences in density compared to 24R or 24R+O, nor was there a difference between 24R and 24R+O. The same trend persisted between OGD and 2R+O and

ORST, where OGD showed higher densities compared to both, and 2R showed higher densities compared to 2R+O and ORST. Across microglial morphometric trends and when contextualized with mitochondrial properties, the 2R+O and ORST groups showed the most prominent effects of OGD.

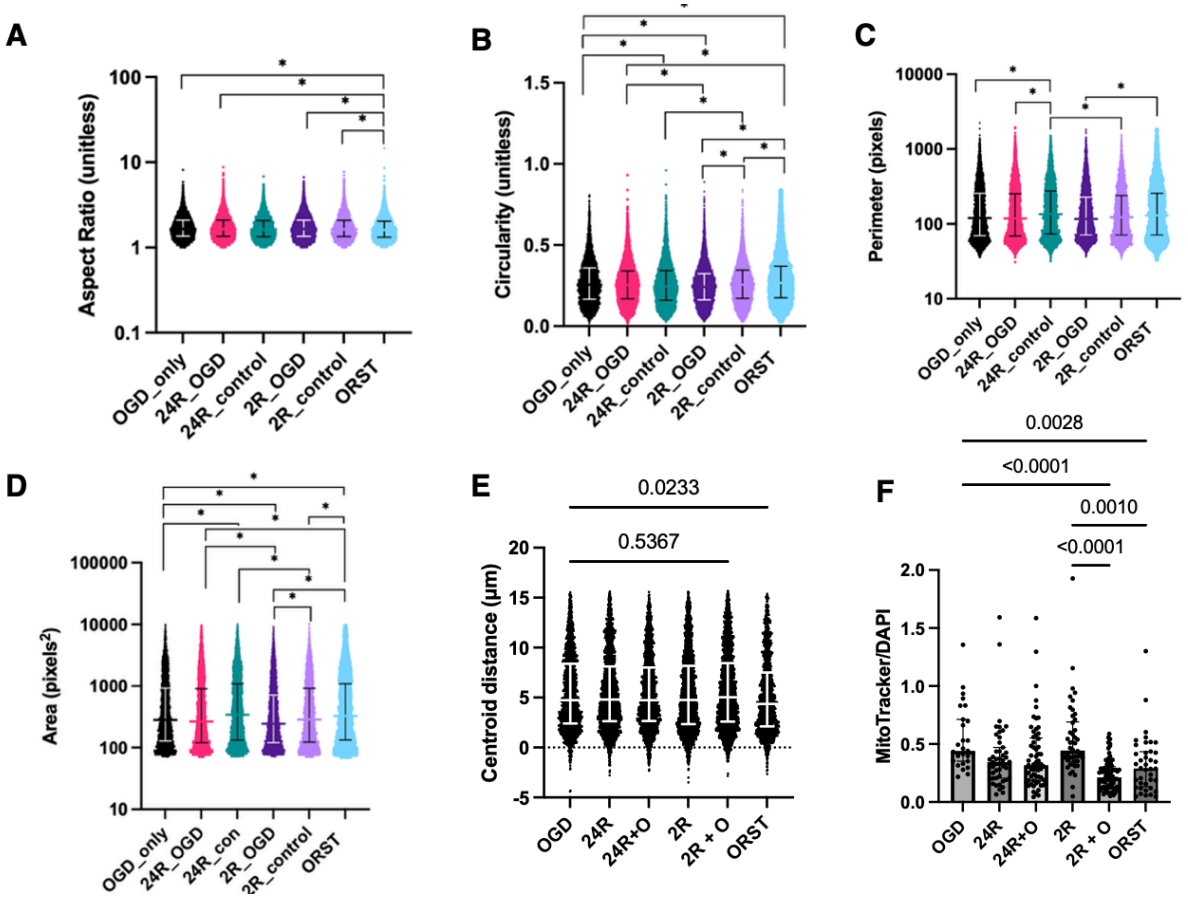

Figure 3.4. Combinatorial group comparison at OGD time and 24h prior to OGD for microglial morphometric features (A) aspect ratio (unitless), (B) circularity (unitless), (C) perimeter (px) and (D) area (px^2). Each data point represents a microglia from an individual image. Mitochondrial image-based assessment for (E) nuclear distances and (F) density where each data point represents an individual MitoTracker object in an image and a relative nuclear distance (microns) in images from n=3 slices each group. Morphometric data was compared using a linear mixed-model in R and image-based was compared using a Kruskal-Wallis test in GraphPad prism, with significance cutoff in both defined at $p < 0.05$.

3.4 Discussion

Mitochondria are critical organelles in the brain's response to ischemic conditions, specifically regarding their roles in inflammation and recovery. Mitochondrial abnormalities also accompany pre-existing conditions or co-morbidities that are shown to increase risk and severity of CI. However, less is known

about how existing mitochondrial abnormalities change the landscape of the brain's inflammatory response to ischemic conditions and lead to less favorable outcomes. Existing mitochondrial dysfunction can alter ischemia pathophysiology in a few ways. One, the recovery from CI injury is shown to be less effective because the injury hinders the ability of mitochondria to produce ATP even after oxygen returns[154]. At the same time, the CI injury, which is known to activate mitophagy, can promote clearance of mitochondria (that are previously inhibited) and allow for fusion of new mitochondria to assist with the response post CI[152]. Most studies to date focus on the effect of CI on mitochondria or the role of mitochondrial dysfunction resulting from CI injury in contributing to CI injury outcomes[155–159] .

Here, we investigated the effect of existing mitochondrial dysfunction on the brain's inflammatory response to ischemic conditions in an OWH slice model of hypoxia-ischemia pre-treated with mitochondrial complex I inhibitor ROT. We showed that ROT pre-treatment leads to more severe cell damage compared to OGD alone, as a function of application time prior to OGD and recovery time after OGD. This effect was seen for all pre-exposure times within 2h of OGD injury and only for 24h pre-treatment and same-time application 48h after injury. However, 24h pre-treatment and same-time application showed unique effects on mitochondrial properties and microglial inflammatory responses despite both interfering with OGD recovery at 48h.

We performed a screening study to evaluate OWH slice health over time in response to different ROT application times relative to OGD. Without combinatorial treatment, we saw results consistent with previous findings in our OGD and ROT OWH slice models: 30 minutes of OGD does shows an injury peak at 24h and recovers by 48h; 50 nM ROT developed injury after 24h and persisted through 48h. ROT alone (48h total following application time) and 24h pre-treatment produced more injury compared to 24h after OGD, also consistent with previous findings[35,75]. We note that OWH slice response and recovery from OGD depends strongly on ROT application time and the effect of pre-treatment time does not follow a linear relationship, with the 24h, 2h, and same-time applications being of particular interest. Introducing combinatorial injury changed the course of OGD response early and after longer times. Interestingly, only the 2h pre-treatment did not show any differences from OGD alone at any time point. This was especially notable at the 2h timepoint; however, only 24h pre-treatment and same-time application led to lasting injury at 48h. While both application times achieved this, it is likely that the response landscape is different due

to the difference in time of ROT exposure relative to OGD. We hypothesize that this may be related to a difference in inflammatory state at the time of OGD, modulated by ROT exposure time.

The 24h pre-treatment of ROT likely primes OWH slices for ischemic injury via microglial activation, an effect which is consistently observed in vitro and in vivo over comparable exposure levels and timescales[35,118,120,124]. The effect of immune cell activation on ischemic injury responses has been explored and pre-treatment with inflammatory vehicles has even shown neuroprotection against hypoxia-ischemia *in vivo* following pre-treatment with pro-inflammatory lipopolysaccharide[162]. However, the effect of the timing of pre-existing inflammation on the ischemic brain has not been extensively explored. Our results show that the effect of mitochondria-driven inflammation is time-dependent. This may be due to the OGD occurring before the window at which ROT shows phenotypic evidence of activated microglia. While one study reported presence of pro-inflammatory signaling factors in a BV-2 cell line 3h after 1 μM ROT[163,164], most report pro-inflammatory phenotypes in vitro over days to weeks[35,107,118,124]. In our study, cells are still operating at a metabolic deficit at the time of OGD which can ameliorate any compounding injury.

While parsing out the mechanism of metabolic deficit in OWH slices is beyond the scope of the study, we can speculate why there is a muted effect of this specific cadence of combinatorial injury. When ROT blocks NADH oxidation, this can offset redox ratios (specifically NADH/NAD+) leading to ROS generation, metabolic shifts, and distress signaling [165,166]. Compromised electron transport chain (ETC) activity also limits processing of glycolysis products. Momentarily halting glycolysis via OGD may help balance the redox ratio by NAD+ production via excess lactate dehydrogenase[167,168]. There is clearly a distinct role of time in complex I-driven mitochondrial dysfunction because same-time application showed a very different outcome. We can reason that simultaneous disruption of OXPHOS feedstock and its machinery may limit the time window for compensatory responses, although studies exploring the kinetics of pathological onset following complex I dysfunction are limited and mainly rely on mathematical models[169,170]. The nonlinearity of the effect of ROT pre-treatment time on OGD recovery highlights a specific role of mitochondrial dynamics on the brain's response to ischemic conditions acutely and over time.

We imaged microglia in OWH slices 24h after OGD and quantified morphometric feature shifts to better understand how varying ROT exposure time alters inflammatory responses following OGD. We observed that morphometric features were most affected by shorter application time windows (2h pre-

treatment, same-time application) and that those feature shifts were consistent with their respective cell damage outcomes. However, for 24h pre-treatment, morphometric features showed pro-inflammatory behavior on par with OGD and ROT alone, demonstrating that inflammatory phenotypes alone cannot explain the higher cell damage at 48h. The timing of ROT exposure drives different inflammatory states at the time of OGD and affects the response to hypoxic-ischemic conditions[171]. ETC damage alters oxygen levels and affects how cells respond to hypoxia via HIF-1α signaling[166,172,173]. OGD in OWH slices is shown to increase HIF-1α levels alongside glial activation and cell damage[75]. Multiple studies have demonstrated that inhibiting HIF-1α pathways improve the response to hypoxia-ischemia[174]. Notably, it has also been shown that introducing inflammation via LPS or interferon-γ prevents upregulation of HIF-1α under hypoxia and leads to protective effects[162]. ROT has also been shown to limit upregulation of HIF-1α under hypoxia [175,176]. For example, 24h pre-treatment may increase available oxygen, which could make the effect of OGD less severe. Limiting the HIF-1α pathway could explain why 24h pre-treatment shows an apparent recovery to normal OGD injury levels 24h after injury.

Another explanation is that complex I inhibition may shift microglia towards a glycolytic metabolism, which is shown to be more associated with pro-inflammatory behavior[165,177]. Glucose deprivation may prevent more pro-inflammatory behavior by limiting glycolysis, which would be consistent with comparable morphometric feature data as well as an apparent recovery after 24h. However, while 24h pre-treatment may be helpful in the short-term, our results show that inflammation resulting from longer time under mitochondrial dysfunction does not prevent longer-term recovery despite limiting HIF-1α or accelerating pro-inflammatory phenotypic shifts. Additionally, HIF-1α has been shown to have a positive effect on later stages following ischemic events[178–180]. We showed that ROT alone drives a decrease in HIF-1α over time, which could be depriving cells of any longer-term benefit. Same-time application suppressed HIF-1α the most yet showed the most pro-inflammatory microglia and a consistent increase in cell damage over time. HIF-1α levels were higher for 2h pre-treatment yet did not drive distinguishable injury relative to OGD. We suspect that the shift away from OXPHOS metabolism, as well as its duration, determine the modality of the cellular response to hypoxic-ischemic conditions[169]. This would need to be confirmed with mechanistic assays for prevalence of OXPHOS and glycolysis, as well as cell-specific injury analysis for cells like neurons, which cannot sustain a shift to primarily glycolytic metabolism[140]. Additionally, other classes of

mitochondrial inhibitors exist that affect mitochondrial integrity in other ways besides ROS generation. Timing is evidently critical for how OWH slices develop inflammatory states and respond to OGD under mitochondrial dysfunction. Our results show that mitochondrial dysfunction interferes with inflammatory and hypoxic signaling that are involved in normal recovery from ischemic conditions.

Mitochondria are responsible for several signaling pathways that dictate cell fate, including programmed cell death and how cells respond to hypoxia[81,149,166]. Dysregulation in their natural equilibrium between fission and fusion states is associated with several pathologies and is shown to be induced by ROT and OGD[155,181]. We assayed mitochondrial responses 24h after OGD and observed that ROT application time affects mitochondrial dynamics and determines alignment with microglia and gene expression data for OGD recovery. As expected, ROT exposure reduced mitochondrial densities in all groups, which was consistent with other image-based quantifications of mitochondrial objects in response to ROT exposure. Longer exposure times had the least impact on density and highest impact on dispersion, along with the most subdued expression of fission/fusion markers. Coupled with the lowest degree of phenotypic shift relative to OGD, we observe a blunted response that may explain the increase in cell damage at 48h. Fusion is a process that is shown to be subdued by complex I inhibition[182], and OGD is shown to promote pro-fission states as lower resources force mitochondria to redistribute and operate more efficiently[15,155].

We also observe that for 24h pre-treatment, OGD suppresses expression of complex I-encoding factors (NDFUS-1) compared to ROT alone. Therefore, we hypothesize here that the longer exposure time suppresses fusion and prevents a compensatory response to OGD-driven fission, resulting in longer-term cell damage. Same-time application showed the lowest density and most closely packed to nuclei, even when accounting for mitochondria specifically associated with microglia. The simultaneous injury was undoubtedly severe. However, gene expression data showed active mitochondria via upregulation of fission and fusion markers. It's unclear how fission/fusion dynamics are affected by the combined injury over a shorter time scale, but the lesser density with high activity alongside the highest pro-inflammatory microglial phenotypic shifts shows a compensatory response. We suspect that severe damage forces cells to aggressively discard damaged and synthesize new machinery[154,155]. Only for same-time application was there an upregulation of fission, fusion, and NDUFS-1. Our gene expression data shows that mitochondrial

injury manipulates the inflammatory and pro-apoptotic cell signaling pathways involved with OGD response, although this was seen predominantly for 24h pre-treatment.

Our results collectively demonstrate a complex landscape between mitochondrial dysfunction and recovery from ischemic conditions. Here, we highlight some contradictory findings and limitations of the study. The 24h pre-treatment group not showing significantly higher injury compared to OGD 24h after injury is difficult to rationalize. This could be the effect of secondary mitochondrial failure, a phenomenon known to occur following ischemic injury where metabolic stress emerges after apparent recovery and contributes to ongoing damage[170,183]. However, OGD alone does not replicate the same injury profile. Perhaps the most important is the 2h pre-treatment condition, because it showed a reduction in mitochondrial density and activity (via gene expression) but a shift away from pro-inflammatory microglial phenotypes. It also resulted in the second-most decrease in HIF-1α levels relative to OGD 24h after injury, which challenges the speculation that the 2h pre-treatment mirrors the OGD injury response.

While the effect of mitochondrial dysfunction on CI injury has not been extensively explored, and we report OWH slices as a tunable system to do so, there are important limitations that motivate the use of complimentary model systems and methods to further explore these dynamics. For example, changes in vascular integrity and blood flow are important aspects of CI pathophysiology which OWH slices cannot readily replicate. Several of the studies highlighted above that point to positive or negative roles of HIF-1α expression in recovery from hypoxia-ischemia are done *in vivo* and specifically reference new vessel generation (angiogenesis)[178]. Mitochondrial integrity in the neurovascular unit also likely plays a role in the pathophysiology of CI injury[150,184,185] and this is not an effect we can explore in OWH slices. Combining ROT exposure with OGD enables high-throughput experimentation of various combinations to probe the interplay between mitochondria and hypoxia-ischemia. However, the experimental tunability between ROT and OGD in OWH slices carriers the cost of oversimplification. The specificity of ROT is beneficial to achieving mitochondrial damage and outcomes of ROT exposure reflect *in vivo* pathologies related to mitochondrial dysfunction[35,103,113,117,122,186], but it does not necessarily represent the development and nuance of mitochondrial dysfunction *in vivo*. Rather, ROT acts as an “on” switch for complex I deficiency, which replicates outcomes of mitochondrial failure, but is not the only cause.[21,170,187–189] Development of mitochondrial dysfunction is a complicated, long-term process that is not fully understood, and is therefore

difficult to replicate in vitro. Our results how mitochondrial damage from complex I inhibition changes the course of recovery to ischemic conditions but simplifies the metabolic landscape that might exist in patients with risk factors related to mitochondrial dysfunction. Ultimately, our results encourage further investigation into the impacts of mitochondrial dysfunction on response to hypoxia-ischemia, using *in vivo* models or different *in vitro* systems that enable more mechanistic insight.

3.5 Conclusion

This study created a model system to study the relationship between CI-like injury and mitochondrial dysfunction, specifically to study how mitochondrial dysfunction influences the course of CI-like injury response. We have shown that combining OGD and ROT injuries by varying application time of the ROT relative to OGD in OWH slices, analyzed through the perspective of metabolic function, can provide insight into these conditions. Mitochondrial distress in response to the combinatorial injuries is more destructive and has a poorer recovery compared to stand alone injury conditions, with the greatest level of damage occurring when both conditions present at the same time (ORST). A difference of 2h in application time relative to OGD was enough to show distinct behavior in degree of pro-inflammatory microglial shifts. Further exploration of this time point at the ORST condition has shown that treatment of active degeneration during the ischemic condition could be most effective while the mitochondrial fission and fusion factors are both upregulated indicating that the cells are attempting to mount a healthy response to the injuries. This effect was not seen for longer pre-treatment or 2h pre-treatment. Mitochondrial activity is differentially impacted by OGD at various times after ROT, leading to different levels of microglial activation responsible for greater cell damage over time. The uniquely active mitochondria in response to simultaneous OGD may be responsible for the sustained pro-inflammatory state seen exclusively in ORST. Collectively, our results point to a distinct role in how mitochondrial dysfunction regulates response to CI-like injury, and supports the utility of the ex vivo platform to probe disease processes in the presence of pre-existing conditions or co-morbidities.

Chapter 4. Nano-based probes for the brain extracellular microenvironment

Filteau, J.R.*, **Butler, B.*,** Schimek, N.*, and Nance, E.

*authors contributed equally to this work

This chapter is published in full in Nance, E. (eds) Engineering Biomaterials for Neural Applications. Springer, Cham. https://doi.org/10.1007/978-3-031-11409-0_2.

4.1 Introduction

The brain is our most complex organ and governs all physiological function, from cognition and emotion to movement, and stress response. Much of the brain's function is determined by complex interactions of cells within the brain parenchyma, the functional unit of brain tissue critical for supporting and protecting cells. In fact, trauma or disease to the brain parenchyma can result in a loss of cognitive function, and in severe cases, death[190–193]. Several studies have shown microstructural changes to the brain parenchyma resulting from a variety of injury and disease states, such as traumatic brain injury (TBI), Alzheimer's and Parkinson's Diseases, depression, and aging[194]. As a result, brain microstructure has garnered significant attention in recent years from scientists and engineers as a neurological and micromechanical sink – an unexplored frontier for disease progression and a critical barrier to therapeutic delivery in the brain.

Through the lens of brain microstructure, we highlight the existing technologies and key considerations for engineers probing the brain microenvironment to study changes in brain development, aging, response to disease or injury, and response to treatment. In this chapter, we provide an overview of the microstructure of the brain and an analysis of existing engineered and biological models of the brain microenvironment. We next highlight the design of nano-based materials to probe the brain microenvironment and important methodologies used to quantify nanoprobe behavior in this complex, dynamic space. Lastly, we discuss the emerging use of data science tools in combination with nanoprobes to elucidate insights about brain microstructure and response of the brain microenvironment to local stimuli.

4.1.1 Microstructure of the Brain Extracellular Space

The brain parenchyma is comprised of neurons and glia, separated by an extracellular space (ECS), and structurally supported by an extracellular matrix (ECM)[194]. The ECS is a narrow, tortuous environment that resembles porous media (Figure 1A-B)[46,195]. From a therapeutics standpoint, the ECS is the final environment through which a drug must diffuse before uptake into cells. An understanding of geometry is therefore critical in the design of drug delivery vehicles to the brain. The geometry of the ECS is typically described by three parameters: volume fraction α, width d_{ECS}, and tortuosity λ (Figure 1C)[46]. Early efforts to characterize brain microstructure focused on quantifying these parameters and inspired the development of novel techniques to probe their heterogeneity.

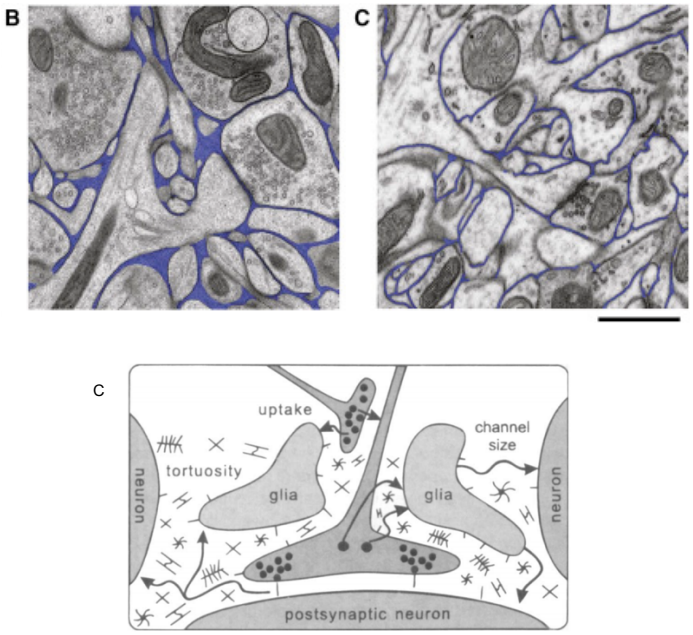

Figure 4.1. Electron microscopy of ECS, colored in blue, in cryo-fixed tissue slices before (A) and after (B) chemical fixation. Adapted from and reprinted with permission from (103). (C) Schematic of ECS parenchyma highlighting geometric parameters, tortuosity, and width around cells of the central nervous system (glia, neurons) and constituents of the extracellular matrix (branched chain structures). Adapted from and reprinted with permission from (102).

Volume fraction is reported as the ratio between ECS volume and total brain tissue volume ($\alpha = V_{ECS}/V_{Tissue}$). Studies measuring ECS volume fraction pioneered investigation of the dynamics of the ECS. Real-time iontophoresis (RTI) (discussed in Section 4.2.2) with the tetramethylammonium ion (TMA^+) provided the first snapshots of the ECS in chemically fixed tissue. By quantifying the area occupied by a

TMA^+ radiotracer , Nicholson and Syková found approximately 20% ($\alpha = 0.20$) of healthy brain volume is attributed to extracellular space (Figure 2). In an *in vivo* adult rodent model of acute ischemia, RTI measurements of ECS volume fraction showed a five-fold decrease ($\alpha = 0.04$) compared to measurements in healthy adult rats[48]. Furthermore, RTI measurements in healthy neonatal rats showed a 40% decrease in volume fraction from postnatal day 4 (P4) to P21. Identifying bulk changes in microstructure highlighted the complexity of the design space for treating conditions such as neonatal ischemia, observing that both acute injury and neonatal development influence extracellular microstructure.

Tortuosity is proportional to the ratio of free-media diffusivity D to local ECS effective diffusivity D^* and is defined as $\lambda = (D/D^*)^{1/2}$. Tortuosity is therefore one metric to describe the extent to which ECS diffusion deviates from free diffusion, with higher values corresponding to more restricted diffusion. In the same adult rodent *in vivo* ischemia model used for measuring volume fraction, Nicholson and Syková applied TMA^+ iontophoresis to determine a healthy-brain tortuosity of $\lambda = 1.50$, with an increased value of $\lambda = 2.07$ observed from acute ischemia. After 17 days of neonatal development, tortuosity was found to decrease from $\lambda = 1.60$ (P4) to $\lambda = 1.54$ (P21) in healthy rats[196]. Early efforts to characterize ECS tortuosity showed the important caveat that increased ECS volume does not inherently mean increased diffusivity, that disease state and developmental age modulate diffusion differently, and that studying the complexity of the parenchyma in these environments would require engineered probes sensitive to microstructural changes.

The width of the ECS serves as a representation of the effective pore sizes in the brain parenchyma, a measurement of the average spacing between brain cells and underlines the heterogeneity of ECS microstructure. Initial studies by Thorne and Nicholson in 2006 used dextrans and quantum dots (one type of engineered nanoscale probe) to predict the distribution of *in vivo* ECS width in rats to range from 38–64 nm[197]. However, later studies in 2008 by Thorne *et al.* emphasized that the material of the diffusion probe strongly influences diffusion measurements. Diffusivities of two fluorescently labeled proteins, lactoferrin and transferrin, with similar molecular weights, were quantified in rat brains *in vivo*. Lactoferrin, with increased affinity to bind ECM proteoglycans (Section 1.1.1) compared to transferrin, showed 60% lower median diffusivity[198]. Nance *et al.* discovered in 2012 that nanoparticle probes, when coated with a dense layer of (poly)-ethylene glycol (PEG), minimally interact with the brain

microenvironment and avoid protein adhesion. This led to the discovery of pore sizes up to 225 nm in *ex vivo* human brain tissue, with 30% of all ECS more sizes greater than 110 nm[199]. This finding of larger pore sizes was confirmed and expanded upon in 2017 by Godin *et al*., who showed that single particle tracking of single walled carbon nanotubes in the living mouse brain ECS revealed pores sizes up to 700 nm in width[200]. As methods for quantifying ECS width in living tissue evolve, the heterogeneity of the ECS will continue to be revealed.

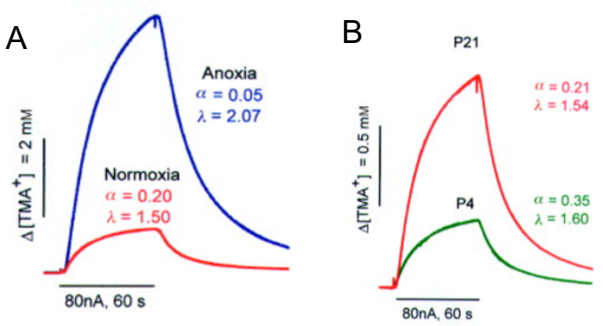

Figure 4.2. TMA^+ outputs of ECS volume fraction and tortuosity show decreased volume fraction and increased tortuosity from normal to low-oxygen conditions (A) and decreases for both parameters with increasing postnatal (P) age (B) in an *in vivo* rat ischemia model. Adapted from and reprinted with permission from (168).

4.1.2 ECM Structure

The ECM, which fills the ECS, serves as a scaffold structure composed of various proteins and cross-linked proteoglycans. It is composed of three parts: a basement membrane exterior to vascular endothelial cells; a neural interstitial matrix that provides structural support and spacing for cells; and perineuronal nets (PNNs) that surround and support interneurons (Section 1.2)[201]. The basement membrane is comprised of laminin, type IV collagen, fibronectin, and a heparan sulfate proteoglycan[201]. The neural interstitial matrix is comprised of a proteoglycan matrix cross-linked by covalent bonds and link proteins. The class of brain ECM proteoglycans primarily consist of hyaluronan chains, which are covalently bound to sulfated disaccharide chains (glycosaminoglycans, or GAGs) known as chondroitin sulfate proteoglycans (CSPGs)[201]. The prominence of hydroxyl groups on disaccharide chains provides an effective negative negative charge for the ECM[202]. Hyaluronan, or hyaluronic acid (HA), serves as the backbone for CSPG binding and does not contain sulfated chains[51]. This physical cross-linking is capable of stiffening and fluidizing like a standard hydrogel[203,204]. Extracellular proteins such as aggrecan, brevican,

tenascin-R serve as link proteins to further mesh together the dense network of hyaluronan and glycosaminoglycans. Figure 3 illustrates the detailed structure and organization of the ECM.

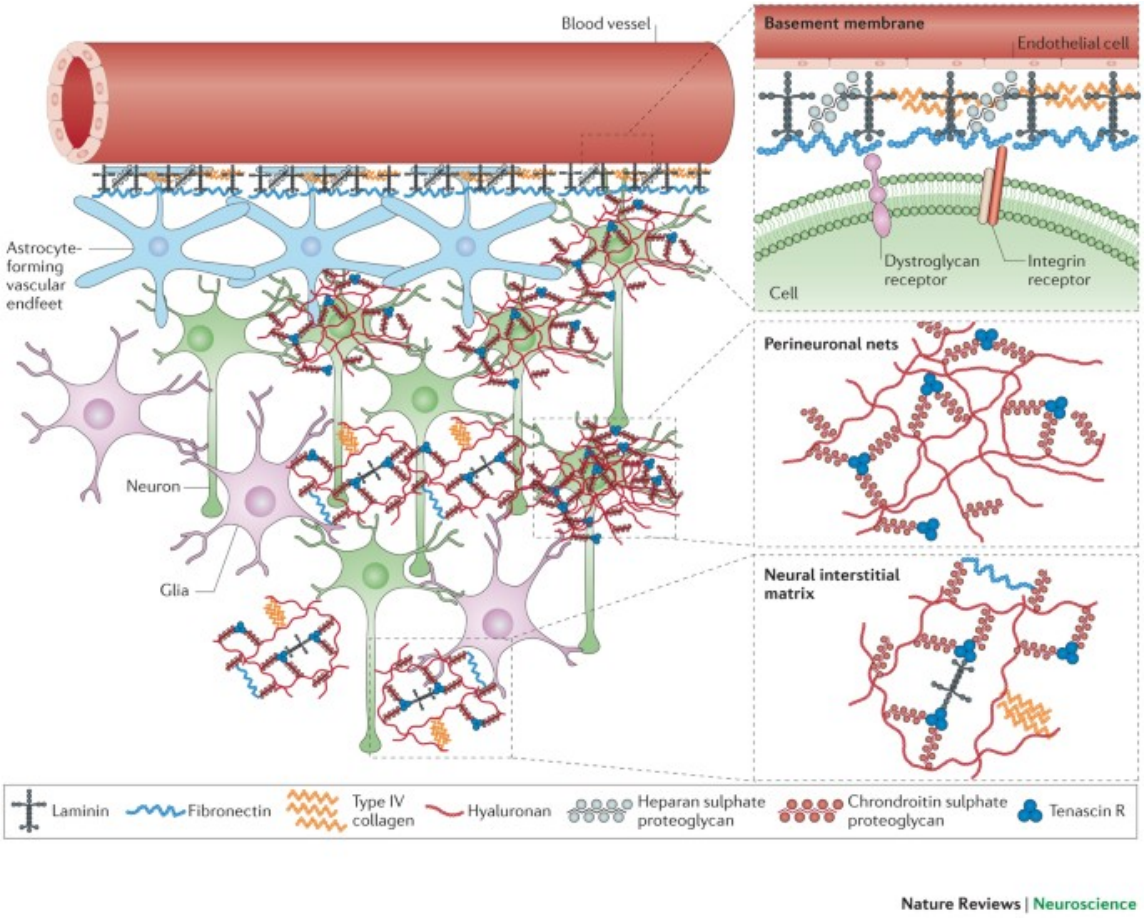

Figure 4.3. Structural arrangements of ECM proteins and proteoglycans: the basement membrane (type IV collagen, laminin, fibronectin and heparan sulfate proteoglycan), perineuronal nets (hyaluranon backbone, Tenascin-R linked CSPGs), and the neural interstitial matrix (hyaluronan backbone, Tenascin-C linked CPSGS, type IV collagen and laminin). Reprinted with permission from Lau *et al.* (174).

4.1.3 Neurobiology of ECS Microstructure

The components of ECM microstructure are implicated in a variety of biological processes. The ECM surrounds resident cells to support intracellular communication, promote cell potentiation, and provide mechanical integrity to brain tissue[201,205201,205]. HA is an important regulator of inflammatory and immune responses within the central nervous system. Its structure provides high affinity to cell-surface binding proteins to facilitate release of inflammatory cytokines and promote migration. Furthermore, HA is known

to play a critical role in embryonic differentiation and tumor development[51], as well as in wound healing[206]. There is a role of CSPGs in maintaining pluripotency in neuronal development and promoting secretion of cytokines for cell division[207,208]. From CSPGs form PNNs, the functional, organized networks around neurons. Another ECM protein, tenascin, is known to be involved in regulating resting microglial surveillance, as well as microglial migration in post-ischemic injury. In neurodevelopment, tenascin helps regulate the proliferation of oligodendrocytes and astrocytes, and there is growing evidence that a relationship exists between tenascin and cellular response in neurodegenerative conditions[43,209,210]. Collectively, ECM proteoglycans all contribute to both resting and disease-state neurobiology in a dynamic manner. Because these structural components have significant overlap with neurobiological dynamics, it is evident that changes in ECM microstructure are correlated with changing biology.

Also present within the ECS is an interstitial fluid (ISF) that is compositionally similar to cerebral spinal fluid (CSF). ISF contains and maintains the concentration of critical ions for synaptic transmission, such as Na^+, K^+, Ca^{2+}, and Cl^- [211] and can influence ECS volume. For example, one study attributed swelling and shrinking of ischemia-afflicted organotypic rat brain slices to changes in ionic strength of the slice bathing medium[52]. It was suggested that the ischemic event permeabilized CNS cell membranes, offsetting the Donnan equilibrium between intracellular fixed negative charges, likely due to local effective negative charges of ECM proteoglycans, and ultimately driving changes in local osmotic pressure[52]. ISF has also been studied in the context of neurodegenerative disease, such as ISF-soluble pathological protein aggregates including amyloid-β in Alzheimer's Disease[212]. Iliff *et al.* investigated clearance pathways of amyloid-β in the mouse brain, before and after the deletion of a gene implicated in astrocyte-mediated interstitial flow[213]. Upon gene deletion, tracking fluorescence of dissolved amyloid-β showed significantly less diffusion compared to non-modified slices, suggesting evidence of ISF paravascular flow. However, future studies contested the presence of bulk flow in the brain interstitial space, attributing glymphatic clearance to diffusion rather than flow[214]. Therefore, it remains debated the extent to which bulk ISF flow may drive convective transport of neurotransmitters and ions, nano-based probes, or therapeutic delivery vehicles within the parenchyma. Independent of the presence of bulk flow, ISF is relevant to ECS neurobiology as a solute bank for ions, neurotransmitters, and pathological proteins.

4.2 Quantifying ECS Microstructural Remodeling

Engineers can assess microstructural remodeling of the brain microenvironment through diffusion, rheology, and composition studies, all of which have important implications in material design. Diffusion is important to consider for neurotransmitters and ions, such as ATP trafficking across the synaptic cleft in neuron firing[154]. Diffusion also plays a key role in design of materials used to probe the brain parenchyma or for therapeutic delivery vehicles, such as nanoparticles[14]. Rheology, the study of how materials deform in response to stresses, is an applicable area of emphasis for the brain parenchyma based on the presence of the hydrogel-like ECM, interstitial ECS fluid, and the ECS volume and geometry. ECM composition analyses can capture the state of ECS structural components as well as detect the presence of key processes involved in structural remodeling. An example of this is seen in age-related neurodegeneration and neuroinflammation, in which the secretion of matrix metalloproteinases (MMPs), enzymes which are known to degrade ECM microstructure, can be fluorescently labeled and imaged in brain tissue[115]. The following subsections will outline diffusion, rheological, and composition studies in more detail and highlight common methodologies.

4.2.1 Diffusion

Changes in ECS diffusion mediated by developmental processes, aging, disease-related or injury-related structural remodeling may be probed by engineered materials. Diffusion is an important parameter in the context of CNS cell-cell communication, solute transport, and therapeutic delivery[59]. Diffusion is directly related to ECS microstructure through parameters such as viscosity (both matrix-related and interstitial)[59], pore size[115], mesh steric hindrance[65], tortuosity[48], and volume fraction[48]. Lehmanküler *et al.* measured differences in ECS parameters in the neocortex and subcortical white matter as rats aged, demonstrating changes in diffusion parameters in the developing brain[215]. A separate study identified anisotropic diffusion in the developing rat corpus callosum[216]. Hindered or otherwise altered diffusion from unrestricted Brownian motion has been shown in brain disease and injury models[217]. For example, measurement of magnetic resonance tracers showed an increase in diffusion in an *in vivo* rat model of Parkinson's Disease[62]. Changes in apparent diffusion coefficient of water, ECS volume fraction, and

tortuosity have been measured in neonatal rat brain after global ischemia[218]. Rats with learning deficits were shown to have decreased extracellular volume and loss of diffusion anisotropy[61].

As we will discuss in Section 3 and 4, the choice of model system and nanoprobe impact measurements of diffusive behavior and should be considered when interpreting data that is generated from diffusion studies in the brain ECS. Additionally, other factors such as the use of anesthesia, or whether a living being is in an awake or sleep state have demonstrated impact on diffusion and perfusion in the brain parenchyma[219,220], and should be considered and further investigated in the application of nanoprobes to the brain ECS.

4.2.2 Rheology

The ways in which the hydrogel-like structure of the ECM may deform in response to disease states has important implications in neurobiology. Mechanotransduction pertains to how cellular and biological processes respond to mechanical stimuli such as structural remodeling of the ECM[221]. Matrix characteristics such as pore size, viscoplasticity and degradability regulate cellular dynamics. Growth, spreading, migration (and others) is influenced by ECM rheology, and vice versa. Cellular dynamics such as growth, spreading, mitosis, and others can exert stresses on ECM microstructure; conversely, the state of the ECM (e.g. stiffness, fragmentation) may also influence the same cellular dynamics, referred to as confinement (Figure 4). The degree to which cellular dynamics are restricted by matrix confinement are functions of pore size, viscoplasticity, and matrix degradability, all of which may be influenced by the progression of disease states (Figure 4)[53].

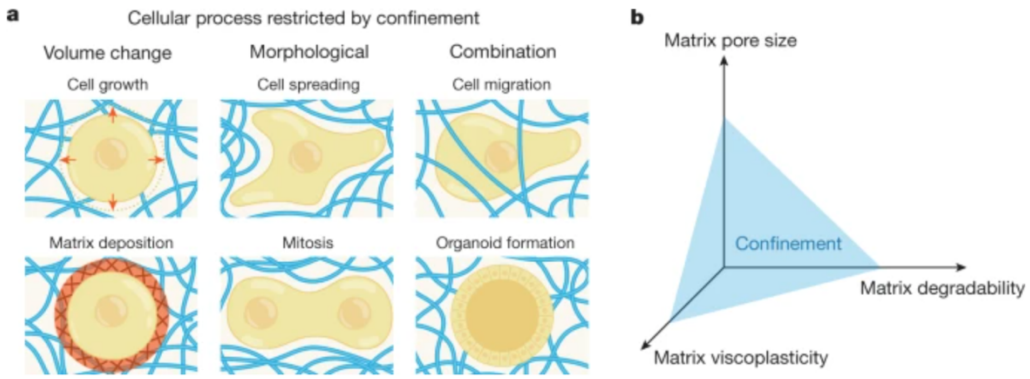

Figure 4.4. (A) Cellular processes that mechanically interact with the ECM, highlighting how morphological changes and dynamics exert mechanical stresses. Fragmented ECM due to MMP digestion may deposit on the surfaces of cells (matrix deposition) to restrict motion or mitotic processes, or a stiffened matrix may restrict cell migration and spreading in general. (B) In 3D culture, confinement of cells within the ECM is a function of matrix characteristics such as pore size, viscoplasticity and degradability. Reprinted with permission from (65).

Elasticity, or stiffness, is a predominant driving force behind mechanotransduction in the ECM. Stiffness is defined as the ratio of stress (force per unit area) over strain (deformation length). Brain tissue and the brain ECM behave as *viscoelastic* materials, having properties of both viscous fluids and elastic solids. In response to stress, ECM has been shown to first demonstrate solid-like elasticity, then dissipate the stored energy in a liquid-like manner[54]. This viscoelastic behavior has gained significant attention as a marker of disease dynamics within the ECS. The interactions between cellular dynamics and rheology of matrix microstructure are influenced by the progression of disease states. For example, viscoelastic alterations are seen in chronic-progressive multiple sclerosis[222], amyloid plaques in transgenic mouse models for Alzheimer's disease[57], and in brain aging[223]. Brain micro-rheology, specifically viscoelasticity, can underscore disease progression from a purely mechanical perspective and is a strong focal point in probing disease dynamics. Local rheology within the brain parenchyma has not been extensively explored, but there is potential for this to be probed by the diffusion of engineered nanoparticles. The Stokes-Einstein relations, fundamental equations of colloidal transport in media, directly relate diffusivity with the effective nanoscale viscosity experienced by a nanoparticle and can serve as a basis for reconciling ECS diffusivity with matrix micro-rheology. Considerations for the design of nanoparticle probes, as well as the technologies used to quantify diffusive behavior, will be discussed in more detail in Sections 4.1 and 4.2.

4.2.3 Composition

The composition of the ECM changes in response a variety of biological processes and can directly impact diffusive ability and brain micro-rheology. Composition can be measured by several techniques, including imaging, western blots, and mass spectrometry. While image-based methods are often considered qualitative or semi-quantitative, they provide a snapshot of ECM protein distribution and presence within the ECS. For example, in a rat binge drinking model, immunohistochemical imaging showed increased expression of ECM proteins and an increase in ECS volume within the orbital front cortex[221]. In an organotypic whole hemisphere brain slice model, fluorescent confocal microscopy captured

reductions in ECM presence following treatment with ECM degrading enzymes hyaluronidase (HYase) and chondriotinase (ChABC) (Figure 5)[68]. The use of fluorescence microscopy in these experiments captured the time dependence of enzyme-mediated breakdown on the scale of hours in *ex vivo* brain tissue. Western blotting can also be used to verify presence of ECM proteins and quantify expression in injury or disease models. From a TBI model in adult male rats, Western blot analyses showed region-dependent (cortex, thalamus, hippocampus, etc.) expression of tenascin and other ECM proteins such as reelin and fibronectin[224]. Additionally, mass spectrometry is capable of identifying and quantifying the presence of biological molecules, such as proteins (proteomics), lipids (lipidomics), and metabolites (metabolomics). Usually, liquid chromatography is used in tandem with mass spectrometry to separate biological molecules prior to analysis. Proteomics has been employed to analyze compositional and abundance difference of ECM proteins in schizophrenia and Alzheimer's disease models[224]. Through lipidomics, pathological aging and age-related neurodegenerative diseases have been studied, revealing differences in lipid content in the brain[225]. Similarly, metabolomic analyses have helped to uncover biomarkers for pathological aging and brain diseases[226].

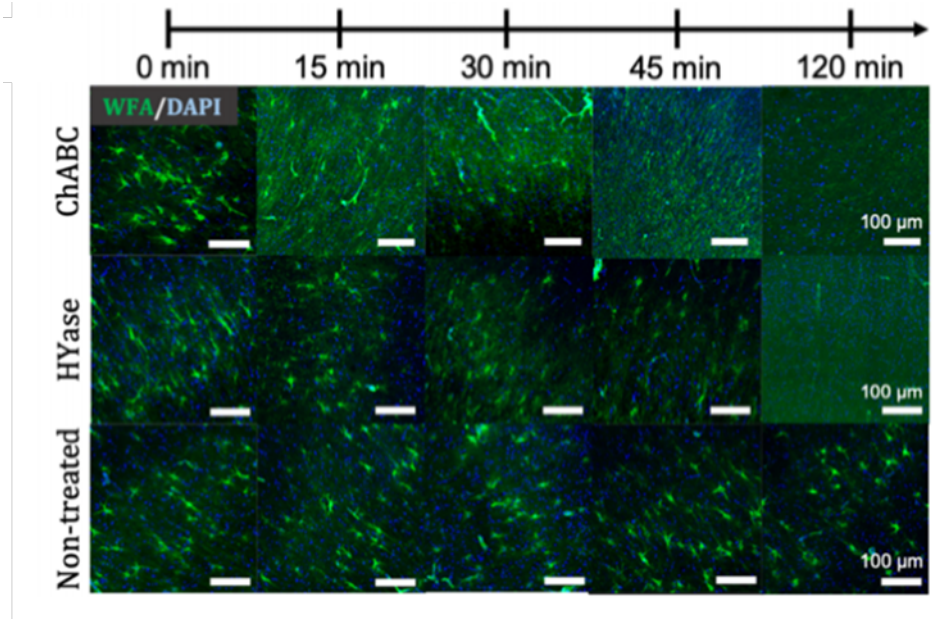

Figure 5. Immunofluorescence microscopy captures degradation of key ECM proteoglycans in response to enzymatic treatments in *ex vivo* rat brain tissue and show qualitatively the temporal dynamics of ECM degradation. Adapted and reprinted with permission from (70).

While diffusion, rheology, and composition studies provide insight into changing biology within the ECS, each also serves as one piece of a highly dynamic, heterogeneous system. It is critical to note that observing changes in, for example, diffusion, does not directly assess changes in ECM composition. Diffusion changes could be due to changes in ECM composition or local ion concentration, microstructural remodeling, or cellular processes. Therefore, changes in the ECS measured by current technologies are often correlative and descriptive rather than mechanistic. Scientists can utilize a combination of model systems, probes, and methodologies to simultaneously capture the complexities and multiple length and time scales of brain ECS biology. The following section will outline existing model systems for probing the brain microenvironment, offering experimental contexts as well as advantages and drawbacks to each.

4.3 Model systems of the brain microenvironment

Model systems used in the study of the brain parenchyma can be separated into three categories: engineered models, *ex vivo* models, and *in vivo* models (Figure 6). Engineered models consist mostly of hydrogel systems designed to replicate the brain microenvironment, but there are also microfluidic systems such as brain on a chip [227] that are becoming more advanced and accessible. *Ex vivo* models are living tissues, representative of a single brain slice to a whole organoid, that are extracted from an animal and used acutely (short window after ex-plantation) or cultured for long-term studies. *In vivo* models use live animals to probe the brain directly, rather than cells or tissue derived from an animal. While generally *in vivo* models most accurately represent the underlying physiology, there are challenges to working with live animals. Logistically, the costs associated with housing animals is high relative to non *in vivo* systems, and the experimental access to the brain microenvironment, in particular the deep brain, is limited. *In vivo* imaging systems used to access the brain are also species limited, with most systems compatible for small animals such as rodents and only a few studies performed with larger animals such as non-human primates[228,229]. *Ex vivo* models are an attractive option because they provide superior experimental access and retain 3-dimensional architecture from the native brain environment. Despite this, *ex vivo* models have been removed from the pressurized environment of the cranium and have no vascular or interstitial flow. Thus, *ex vivo* models are not the best model to study flow in the brain, unless using a specialized culture setup[230]. Engineered systems like hydrogels are highly tunable frameworks capable of recapitulating the brain microenvironment by varying parameters such as gel pore size, gel stiffness, and gel material.

However, as fully synthetic representations of the brain environment, they lack native architecture. Further work should be conducted toward reconciling the differences between model systems. For example, it has been observed that *ex vivo* slices swell shortly after extraction, which likely changes ECS parameters such as pore size when the slices are used acutely. Additionally, *ex vivo* brain slices reorganize their neuronal connections over culture time[231]. Although it has been observed that some cell types retain morphology like those of cells *in vivo*[29], it is unclear how changes in ECM structure compare to natural changes *in vivo*. In this section, we will summarize the model systems used to probe the brain environment and outline work respective to each type of model.

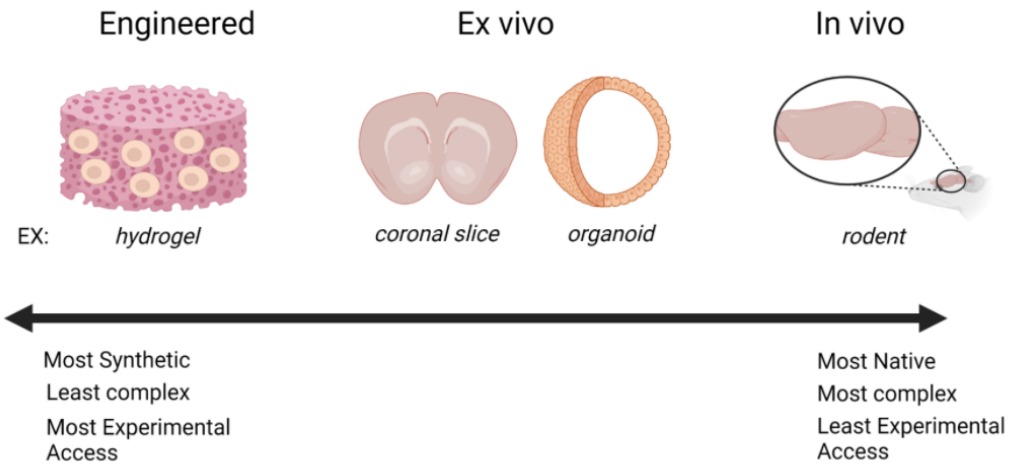

Figure 4.6. Model systems vary in retained native brain architecture, complexity, and experimental access. Created with BioRender.com.

4.3.1 Engineered models

Cell cultures are commonly immobilized into hydrogels of different materials, including polyacrylamide, agarose, and collagen. The simplest system is the case of a single material gel (ie. agarose) at a weight percentage to create a representative matrix of the brain. Although agarose has favorable properties for mimicking the *in vivo* brain environment, it has little effect on the cells immobilized in the gel. Agarose gel at 0.2-0.8% (w/v) have been employed as geometric model systems of the brain ECS, as the pore size of gels in that weight range resembles brain tissue[232]. Polyacrylamide gels also have shown gemoetrical similarities to brain tissue. Researchers found that the injection of a dye into a 3% (w/v)

polyacrylamide gel had similar pressure profiles and volume distribution compared to *in vivo* tests[233], but the use of polyacrylamide with cells introduced toxicity concerns[234]. An alternative material, collagen, has been formed into gels at 0.3% (w/v) to mimic brain stiffness and support neuronal growth, promoting the induction of human pluripotent stem cells[235]. However, collagen is not abundant in the brain unless in the presence of disease, limiting the compositional relevance of this model to the brain microenvironment.

4.3.2 *Ex vivo* models

Thin slices of brain tissue (~300-450 μm) can be harvested from animal donors, or humans[24], and cultured for days to weeks. The two most characterized methods for preparing brain slices are the roller tube and semi-porous membrane techniques, but the latter is more widely used. In addition to easy experimental access to the brain parenchyma, a single animal can yield tens of brain slices with native architecture and cell distribution, allowing high-throughput experiments to probe the brain environment. Researchers can use brain slices to measure changes in the brain structure, such as ECS volume[30], and the diffusive ability of nanoparticles[67,68,236]. Changes in volume and diffusion are capable of informing structural modifications to the ECM, for example in response to brain injury. Slice models reorganize in structure throughout culture and in response to biological stimuli[31], making them a dynamic system to study the brain environment. Brain slices have been used to study the response of a myriad of neurodegenerative disorders and brain disease or injury to measure changes to the ECM that are implicated in many diseases[28,237,238].

Organoids also provide promising *ex vivo* platform to model and probe the brain microenvironment. Organoids are stem cell-derived self-organizing structures that can recapitulate the brain in structure and composition, acting as an effective model of the cellular and organizational makeup of the brain[239]. They tend to be larger in overall volume and thickness than brain slices, which can result in a population of necrotic cells in the center of the organoid if grown too large[239]. One application of organoids is their use as a model for brain cancer, such as glioblastoma, where cells from the cerebral cortex can be grown and model changes to the brain ECM after cancer invasion[240]. The application of probes in organoids has been less extensively studied compared to the use of probes in brain slices but is an anticipated area of growth as the use of organoid models to study neurobiology and neuropathology becomes more prevalent.

4.3.3 *In vivo* models

In vivo work tends to be more costly to conduct than *in vitro* and *ex vivo* methods, but in turn, *in vivo* models have the best representation of the brain environment. This is largely due to the presence of intact native 3D architecture and cell populations, the presence of systemic factors such as the immune system, and the presence of interstitial and vascular flow. *In vivo* models also represent the dynamics of the brain in the context of the dynamics of the whole body and body systems. For example, there are links between events such as hypoxia-ischemia and cardiac function, highlighting an interplay between the brain and heart that may invoke a different cellular response than if the brain was cultured in isolation from the heart[241]. While the presence of biological barriers such a reticuloendothelial clearance and the blood-brain barrier restrict *in vivo* access to many probes accumulating in the brain ECS, researchers have successfully probed the brain environment through use of fluorescent tracers and particles injected locally. Dyes and quantum dots have been used *in vivo* to predict the width of the brain ECS in rodents [46,48] and reveal structural data about the ECS, including geometry and volume. However, many of these studies that probe the ECS in living animals require invasive injection procedures into the ventricular or parenchymal spaces or are limited to superficial brain regions such as the neocortex. Therefore, some biological questions may be more easily probed via a system with easier access, such as *in vitro* or *ex vivo* models.

4.4 Quantitative Imaging Techniques for Nanomaterial-based Probing

As discussed in Section 3, choice of model system is one important aspect of probing the brain ECS. Equally critical is the choice and design of the probe itself. This section will focus on the use of nanomaterials as probes and describe the key engineering considerations for nanoparticle formulations, and the technologies used to quantify nanomaterial behavior in the brain ECS across a range of spatiotemporal resolution.

4.4.1 Considerations for Design of Nanoparticle Probes

Nanomaterials are typically described as having at least one dimension in the nanoscale (1-100 nm). Nanomaterials that have been used to probe the brain parenchyma are polymeric nanoparticles, dendrimers, quantum dots (QDs), and carbon nanotubes[79,242]. Nanoparticle formulations typically seek to control particle size, shape, surface charge, and surface functionality, all of which affect nanoparticle fate

and are important design parameters to consider based on the choice of model system. The following section isolates each characteristic of nanoparticle design, highlighting key studies of the individual design parameters on behavior in the brain ECS.

4.4.1.1 Size

Nanoparticle size is typically reported as the effective average hydrodynamic diameter of a nanoparticle population. Dynamic light scattering (DLS) is the most common method to analyze particle size and size distribution for spherical nanoparticles. For nanoparticles with different geometries, such as carbon nanotubes, Raman spectroscopy is commonly used to quantify size characteristics by inelastic light scattering[243]. DLS measurements can compute effective hydrodynamic diameter on number-averaged, volume-averaged, or intensity basis. Number-weighted distributions are most useful when it is desirable to know the number of particles (e.g. for dosing or perfusion) or when individual particles are to be tracked at high resolution. Size distributions are reported by polydispersity index (PDI). Monodispersity of a nanoparticle population, which indicates a tight distribution around a single effective hydrodynamic diameter, is generally accepted for PDI < 0.1.

Size has been extensively investigated for its impact on nanoparticle fate in the brain microenvironment. In 2012, Nance *et al.* investigated the effect of nanoparticle size in *in vivo* mouse brain and *ex vivo* human brain tissue. Nanoparticle diffusion was quantified in each of these models, with *ex vivo* diffusion data compared against free diffusion in artificial cerebral spinal fluid (ACSF). Polystyrene (PS) nanoparticles functionalized with a dense poly-ethylene glycol (PS-PEG) coating were synthesized to hydrodynamic diameters of 40 nm, 100 nm and 200 nm. Increasing PS-PEG particle sizes showed decreased nanoparticle diffusivity *ex vivo* and *in vivo* (Figure 7A)[77]. A similar trend was shown in *ex vivo* brain slices obtained from adult rats, where 60nm to 240nm PS-PEG nanoparticles showed increasingly hindered diffusion with an increase in size[77,244]. The order of magnitude of computed diffusion coefficients across all three particle sizes in mice, rats, and human tissue was consistent[77,244]. Curtis *et al.* confirmed findings of an inverse relationship between diffusion coefficient and particle size for PS-PEG nanoparticles ranging from 60 nm to 2 μm (Figure 7B)[236]. Additionally, size effe[1,2451,245]. The cost of treat and dendrimer [242,246] penetration within the brain parenchyma have indirectly been studied via biodistribution. Quantum dots functionalized with a dense coating of methoxy-PEG (PEG-OMe) that are 35 nm in size showed rapid

diffusion in *ex vivo* human tissue[77]. Similarly, quantum dots that were less than 20nm in size and functionalized with PEG-OMe were able to readily penetrate within an *ex vivo* rat tissue model[247]. Dendrimer nanoparticles will be discussed in more detail in Section 4.1.3, given that most studies of dendrimer nanoparticles alter surface functionality, which impacts dendrimer hydrodynamic diameter.

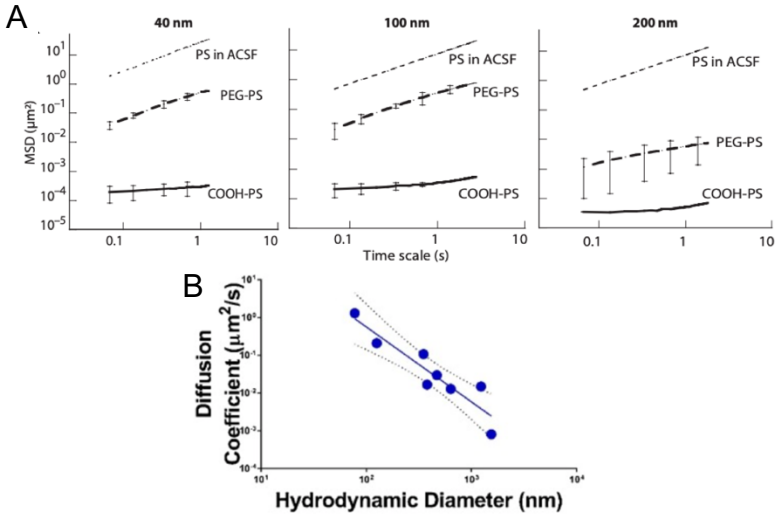

Figure 4.7. (A) Mean-squared displacement (MSD) of PS-PEG nanoparticles of increasing particle size, in *ex vivo* human brain tissue, compared to control MSD of non-PEGylated PS nanoparticles (PS-COOH) in brain tissue and in free ACSF media. Increasing particle sizes showed decrease in mean-squared displacements (MSDs) for all three nanoparticle formulations. MSD is used to compute diffusion coefficients and is therefore correlated with diffusivity. Adapted and reprinted with permission from (12). (B) An inverse relationship between diffusivity and particle size for PS-PEG nanoparticles ranging from 100 – 1000nm. Adapted and reprinted with permission from (209).

4.4.1.2 Surface Charge

Surface charge is another important parameter to consider in nanoparticle design for probing the brain microenvironment. At the nanoscale, nanoparticles within the parenchyma experience electrostatic interactions from the negatively charged ECM[248], alongside steric interactions from matrix fibers [65] and hydrodynamic interactions[248]. Local ion and pH gradients within ISF may also pose additional electrostatic interactions with diffusing nanoparticles.

Surface charge is commonly measured by zeta potential (ζ-potential), a measurement of the electric potential of the effective electrostatic double layer that covers the surface of a nanoparticle. While it should be acknowledged that ζ-potential is a corollary to surface charge and does not offer a direct

measurement, ζ-potential remains the most commonly used method for surface charge characterization. Charge neutrality of a nanoparticle is generally accepted to be within a ζ-potential measurement of ±10 mV.

Several studies have examined the effects of surface charge on nanoparticle fate within the brain parenchyma, and the importance of charge neutrality in nanoparticle formulation. Nance *et al.* showed that diffusion of carboxyl-modified PS nanoparticles (PS-PEG) was severely limited by the exposed negative surface, compared to the neutral surface of densely PEGylated PS nanoparticles[77]. Zhang *et al.* investigated the effects of surface charge on biodistribution of polyamidoamine (PAMAM) dendrimers in the rabbit brain[249]. PAMAM dendrimers were functionalized with hydroxyl (OH) groups (ζ = +4.5 mV) or carboxyl (COOH) groups (ζ = -28.6 mV), controlling for particle size (d_{OH} = 4.3 nm, d_{COOH} = 3.2 nm). Immunofluorescence imaging of COOH-functionalized dendrimers showed high signal within the brain parenchyma, and minimal signal around endothelial cells and within vasculature when particles were administered intra-amniotically to late-gestation fetal rabbits exposed to endotoxin. OH-functionalized dendrimers stayed predominantly within vasculature and did not readily penetrate the parenchyma. However, when particles were administered intravenously to newborn rabbits exposed to endotoxin, COOH-functionalized and OH-functionalized PAMAM dendrimers were able to readily accumulate and distribute within the brain parenchyma to localize in cells, compared to amine-functionalized PAMAM dendrimers which did not accumulate in the brain parenchyma[250]. It was therefore evident that surface charge of the PAMAM dendrimers influenced brain tissue penetration and subsequent cell uptake. Although in these studies, nanoparticle surface charge was the focus, as mentioned in Section 1.1.1, it is important to understand the local charge environments through which nano-based probes or delivery vehicles must transverse, and incorporate this consideration into nanoprobing experiments, as well.

4.4.1.3 Surface Functionality

Nanoparticle surface charge can be imparted by a range of functional groups or ligands conjugated or adsorbed to the nanoparticle surface. Surface functionality has been shown to impact diffusion within the brain parenchyma and in some cases has helped overcome size-based limitations of diffusion. For example, nanoparticle delivery and transport through the ECS was thought to be strictly limited by the upper-bound of 60 nm, based on the restricted diffusion of 35 nm quantum dot nanoparticles[251]. Nance *et al.* published critical evidence that densely coating the quantum dot particles with PEG demonstrated that

PEG density on the particle surface significantly influenced diffusive ability[77]. This finding of controlling surface density allowed for larger than previously expected nanoparticles, up to 114 nm in size, to diffuse in the brain ECS[77].

Surface functionality has important implications for delivering higher quantities of drug encapsulated in larger nanoparticles. Nanoparticles in drug delivery and biological imaging applications need to be able to travel to penetrate the brain parenchyma to reach their target sites without degrading or being phagocytosed. Nanoparticles that can diffuse can improve therapeutic outcome, as shown in several glioma models in rats and mice following intratumoral administration of nanoparticles loaded with paclitaxel[252], systemic administration in combination with focused ultrasound of cisplatin nanoparticles[253], and convection-enhanced delivery of cisplatin nanoparticles[254]. Other formulations functionalized with PEG, such as poly(lactic-co-glycolic acid) (PLGA)-PEG nanoparticles loaded with curcumin, have shown improved delivery and efficacy in an *in vivo* model of hypoxia-ischemia, when particles are capable of diffusing[255]. The impact of surface functionality is not restrictive to larger nanoparticles such as PLGA and similar polymers that are often in the size range of 60-100 nm. Dendrimer nanoparticles conjugated with N-acetyl cysteine (3-4 nm in size) were injected systemically in a rabbit model of cerebral palsy and evaluated for therapeutic effect. An -OH functionalization on the dendrimer surface is effective at both crossing the blood brain barrier, distributing in the brain parenchyma, and reaching microglia cells[256], which significantly improved neurological function in a rabbit model of cerebral palsy[257]. In a study investigating quantum penetration in the brain ECS, quantum dots functionalized with PEG-OMe and PEG-OH showed significantly increased distribution within the rat brain ECS in an organotypic brain slice model, compared to negatively charged 3-mercaptopropionic acid (MPA) functionalized quantum dots[247]. All quantum dots had the same hydrodynamic size. These findings translated *in vivo*, where uptake and cellular localization in the brain varied depending on end-functional group on the quantum dot surface[247]. Nanoparticle surface functionalization is a highly tunable formulation parameter that clearly impacts penetration and distribution within the brain ECS, regardless of nanoparticle size, and is a design consideration that requires further investigation for a wider range of nanomaterials.

4.4.1.4 Shape

Penetration ability within the brain ECS may be altered by nanoparticle shape, considering force balances between local ECS viscosity and nanoparticle inertia (directly related to surface area). Different nanoparticle shapes can have higher surface-area-to-volume ratios, which would allow for more dense "stealth" coatings or other biologically functional ligand coatings. Tuning formulations to be more sensitive to viscous forces could ultimately provide more insight into brain micro-rheology, further uncovering the mechanics of ECS remodeling[258].

While the effect of shape on brain parenchymal penetration has not been extensively explored, we can take lead from studies in ECM-model systems and other biological environments. Geng *et al.* examined the effects of PEGylated micelle shape on clearance and drug delivery of anticancer drug paclitaxel to human-derived tumors within mice. Paclitaxel was loaded into filament-like micelles of different lengths, referred to as *filomicelles*. It was determined that filomicelles up to 8 microns in length were stable throughout circulation. Studies found that a 1 mg/kg loading of paclitaxel in 8-μm long filomicelles had the same therapeutic impact as an 8 mg/kg loading in 1-μm long filomicelles[259]. Therefore, the shape of the delivery vehicle may offer one approach to optimizing chemotherapeutic dose for impact and patient reaction.

Lee *et al.* compared diffusion rates of different shaped viral nanoparticles (VNPs). VNPs are derived from natural plant viruses, genetically encoded to self-assemble into monodisperse structures with high precision over shape and size[260]. In these studies, rod and spherical VNPs were used in a spheroid model of a tumor microenvironment. Axial and transversal diffusion coefficients were computed from fluorescence microscopy data, which will be discussed in Section 4.2.3. Rod-shaped VNPs showed axial diffusion approximately 40% faster than transversal diffusion in the porous environment of the spheroid tumor model. Initially, the rod-shaped VNPs diffused faster than their spherical counterparts; however, beyond 30 minutes, the spherical VNPs achieved a diffusivity 12-fold larger than the rod-shaped VNPs[260]. Observing a greater difference in initial diffusivity of rod-shaped nanoparticles has important implications for delivery applications where initial release should be maximized, such as in treatment of acute injuries.

Ridolfo *et al.* performed a set of studies in *ex vivo* porcine retinal tissue, for which a variety of nanoparticle morphologies (tube, sphere, and curved, flexible tubes referred to as worms) were observed

for their impact on tissue penetration and diffusivity[261]. Fluorescent labeled nanoparticles of each morphology were tracked *ex vivo* in porcine retinal tissue, with movement quantified by live-video fluorescence microscopy for particle tracking. Diffusivities were compared by mobility ratio, defined as the ratio of diffusivity in water to the diffusivity in the vitreous fluid of retinal slices - mobility ratio that approaches unity would indicate the fastest diffusion. It was found that the worm-like nanoparticles (1 μm length, 50-100 nm width) diffused the fastest, with a mobility ratio of approximately 5 to 6-fold less than the spherical nanoparticles (Figure 8)[261]. Although these studies were performed in other extracellular environments, rather than in the brain, the results demonstrate the potential for shape to further probe nanoparticle diffusion within the brain microenvironment. Nanoparticle shape is certainly an area of emphasis for future nanoprobe studies in the brain.

FAST	Dw/Dv ratio						SLOW
4.98	5.23	12.8	17.1	17.1	18.8	27.0	31.3
CA-worm	**Worm**	**CA-tube**	**CA-sphere**	**Tube**	**A-tube**	**A-sphere**	**Sphere**

Figure 4.8. Mobility ratio of nanoprobe diffusivity in water (Dw) representative of a free medium, versus diffusivity *in vitreous* fluid (Dv) for a different nanoparticle morphology (worm, tube) and surface functionalization (A, amine; CA, carboxylic acid) in *ex vivo* porcine retinal tissues, quantified by particle tracking live-video fluorescence microscopy. Adapted and reprinted with permission from (233).

4.4.1.5 Additional Design Considerations for Nanoparticle Probes

In addition to physicochemical properties, nanoparticle behavior in environments such as the brain ECS may be influenced by the method of administration. As noted in Section 4.1.2, intravenous versus intra-amniotic delivery (e.g. oral delivery for the fetus) of COOH- and OH- modified dendrimer nanoparticles resulted in different parenchymal distributions in the brain[249,256]. The presence of disease will also influence nanoprobe behavior in the brain ECS, as has been shown in cerebral palsy[246,256,257], tumor[252–254], and ischemia models[242]. An often-understudied factor in evaluating nanoprobe use in the brain is the colloidal stability of the nanoprobe in relevant media such as CSF and ISF. Curtis *et al.* investigated colloidal stability of PEG and COOH functionalized PS nanoparticles in a range of CSF compositions, and at different pH and temperature[236]. The results indicated that colloidal stability and subsequent ability to probe the ECS is impacted by presence and concentration of divalent cations such as Ca^{2+} and change in local pH[236]. Additional studies investigating the colloidal stability of nanoprobes in conditions relevant to brain disease and brain injury should continue to be performed.

4.4.2 Methods for quantifying diffusion in the brain microenvironment

Multiple techniques exist to quantify diffusion and diffusion-related parameters (tortuosity, pore size) within the brain microenvironment. This section outlines a selection of imaging techniques, across a range of resolutions and experimental applications, highlighting advantages and drawbacks. Integrative optical imaging (IOI), for example, provides a widely applicable method to measure the diffusion of fluorescent nanoparticles by delivering a solution of either charged or neutral particles to the sample, but relies on pressure ejection which can lead to variance in the delivered volume[262]. Real-time iontophoresis (RTI) provides another method for diffusion analysis and molecule delivery, used in pioneering studies by Nicholson and Syková, with high precision in volume delivered but can only inject charged molecules[262]. Particle tracking techniques, specifically single particle and multiple particle tracking, provide nanoscale spatial resolution and can be used for microrheological studies, but most accurate when applied to soft materials at equilibrium[66,238,263]. Each method has benefits and limitations, making it important to choose an appropriate technique depending on the context of a study and the questions being asked.

4.4.2.1 Integrative optical imaging

IOI is a technique that allows for detection of the optical signal from diffusing, fluorescently tagged molecules. This is done by using pressure to eject the tagged molecules which then diffuse through the sample being imaged as shown in Figure 4.9. The microscope captures an image consisting of the in-focus two-dimensional plane as well as signals from the other out-of-focus planes from the sample. The diffusion parameters for the whole signal are calculated by fitting a theoretical expression based on the diffusion of molecules away from the point source. IOI has proven effective in a variety of applications for probing the ECS. IOI with dextran polymers has been successfully employed to analyze extracellular diffusion in the ECS. Nicholson *et al.* used IOI to compare diffusion coefficients of dextrans across four molecular weights (3,000 – 70,000 Daltons) in agarose hydrogels and brain tissue and found that the diffusivity values agreed with theoretical models. Tortuosity measurements for 3,000 and 10,000 MW dextrans agreed with prior TMA^+ experiments, showing higher tortuosities for higher-MW dextrans. These experiments validated IOI's capability of measuring diffusion parameters in tissue, as well as size-related hindrance of diffusing molecules within engineered gels and *ex vivo* brain tissue depending on the choice of material[66,263]. Xiao *et al.* used IOI to analyze anisotropic diffusion in *ex vivo* turtle brain tissue, determining the major-axis and

minor-axis diffusion coefficients for five dextran polymers with molecular weights ranging from 547 to 525,000 Daltons, once again capturing size-related hindrance of diffusion. The authors found that in an anisotropic brain region, the diffusion coefficients decreased with increasing molecular weight until 75,000 Da and then plateaued, indicating that polymers at a molecular weight of 282,000 and 525,000 Da are restricted in movement in the brain ECS[66]. These studies motivated the design of nanoparticle probes to minimally interact with the brain microenvironment. As highlighted in Section 1.1, IOI coupled with quantum dots has also been used to determine diffusion coefficients in normal rat brain ECS and in rats with terminal ischemia[251].

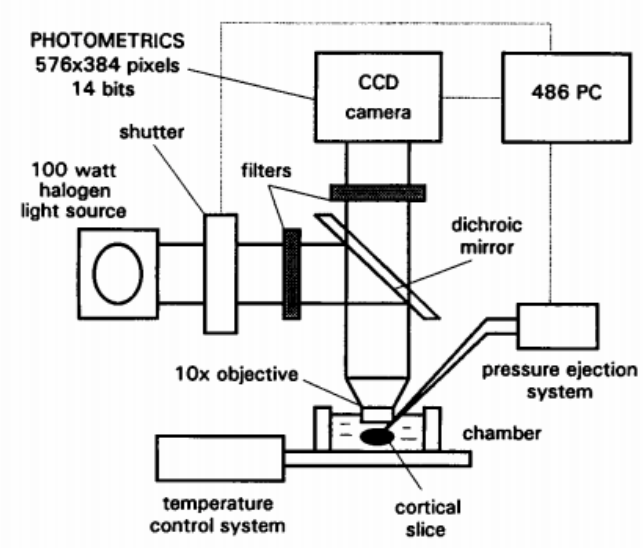

Figure 4.9. Experimental setup for integrative optical imaging of *ex vivo* brain tissue sections. Reprinted with permission from (68).

4.4.2.2 Real-time iontophoresis

Recalling Section 1.1, RTI is another material-based approach to quantifying ECS characteristics such as volume fraction and tortuosity. This method resolves spatial distribution of ECS parameters in brain tissue by probing the changing concentrations of an inert ionic molecule with a highly selective microelectrode and fitting the results to quantify geometric characteristics[48,50]. This method was originally used by Nicholson and Syková to quantify ECS volume fraction and other bulk extracellular properties in response to neonatal development and adult acute ischemia[50]. Two types of RTI are Fluorescence Recovery After

Photobleaching (FRAP) and Forster Resonance Energy Transfer (FRET). FRAP is generally useful for studying diffusion of proteins and biomolecules, binding characteristics and immobilization patterns, and has been used to measure *in vivo* ECS diffusion of fluorescein dextrans in *ex vivo* slice cultures[50,264]. To examine smaller-scale biological processes such as Ca^{2+} signaling, transduction pathways, protein conformational changes, FRET is preferred and has been successfully used to image glutamate neurotransmitters in *ex vivo* slices, as well as to probe *in vivo* neuroinflammation in adult mice[265–267]. At the time of this publication, little to no FRET or FRAP protocols are applied to nanoparticles and are instead used to photobleach biological molecules like proteins. One could conceivably use these techniques to track fluorescent nanoparticles in the brain microenvironment, providing an additional method of gathering diffusional data. However, given the expected intensity of light needed to photobleach fluorescent nanoparticles, which are often designed to resist photobleaching, one concern would be the cytotoxic effects of high intensity light on cells in the model system. Alternative imaging methods can address this by limiting the volume of high intensity light required to generate fluorescence, such as multi-/two-photon excitation. This method also narrows the focal plane to reduce out-of-plane fluorescence in 3D samples. Nanoparticles could be conjugated with fluorochromes that photobleach at lower intensities, such as green-fluorescent protein. Another material alternative to limit cytotoxicity from photobleach-level intensity is quantum dots (QDs) due to their photostability. However, studies of surface-functionalized Cd/Se and Cd/S QDs in all three types of model system for the brain environment demonstrated that QD stability and toxicity depend on the choice of model system, as well as concentration when applied to *in vivo* and *ex vivo* systems[268]. The limitations associated with IOI and RTI motivated the development of novel probing techniques to achieve higher resolution analysis with higher throughput and minimized toxicity.

4.4.2.3 Particle tracking

As introduced in Section 1.1, techniques such as IOI and RTI are useful for capturing spatiotemporal changes in living tissue but lack the resolution to capture nanoscale ECS dynamics. Particle tracking is a common method that generates quantifiable features of the nanoscale environment, such as pore size, diffusivity, diffusion modes, and effective nanoscale viscosity, by measuring the displacements of fluorescent nanoscale probes driven by random Brownian motion in media[268]. In one study demonstrating the connection between particle tracking and rheology, trajectories of PEGylated nanoparticles were

quantified in three hyaluronic acid (HA) hydrogels of increasing molecular weight. Hydrogel molecular weight is proportional to increasing chain length, chain density, and mesh size, differences in which diffusing nanoparticles should detect. Bulk viscosities were first determined by cone-and-plate rheometer measurements (Figure 10A). Diffusivity was measured using multiple particle tracking (MPT) to generate nanoparticle positional displacements over time in HA gels. This expected viscosity change with increasing molecular weight corresponded to a significant decrease in median effective diffusion coefficient (D_{eff}) and distribution of effective diffusion of nanoparticles, demonstrating the ability of nanoparticle probes to sense microstructural changes via diffusion measurements (Figure 10B). While this study provides one example in an engineered model of brain tissue, particle tracking techniques provide a method for measuring changes in ECS diffusion as a function of local viscosity or structural changes, enabling nanoscale sensitivity and the capability to track hundreds to thousands of particles simultaneously[69].

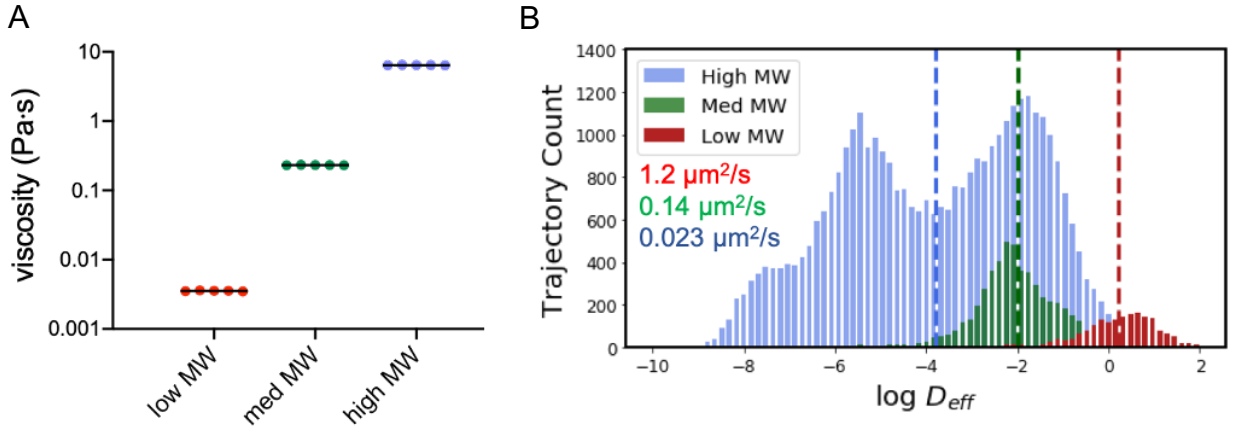

Figure 4.10. (A) Viscosity of hydrogels made with low (red), medium (green) and high (blue) molecular weight hyaluronic acid. (B) Log of the diffusion coefficient, and corresponding trajectory count, for hydrogels with high molecular weight hyaluronic acid (blue), medium molecular weight hyaluronic acid (green), and low molecular weight hyaluronic acid (red).

4.4.2.3.1 Single Particle Tracking

Single particle tracking (SPT) employs bright-field or epifluorescence microscopy to track Brownian motion of particles such as quantum dots, carbon nanotubes, fluorescent nanoparticles within a medium. SPT begins by introducing fluorescently labeled nanoparticles *in vivo*, *ex vivo*, or *in vitro.* SPT tracks the motion of one single particle and computes the associated MSD of the trajectory. This allows for long time-scale tracking for tens of minutes over localized areas, but also results in less overall trajectory data. SPT

has successfully been employed in efforts to probe the brain ECS. Single-walled carbon nanotubes (SWCNTs) have been used to probe nanoscale ECS rheology, detecting regional variations and significant differences across tissue donor age and species[79]. Another study used SWCNTs *in vivo* to probe ECS in a Parkinson's neurodegenerative mouse model, finding that the resulting damaged hyaluronan structure led to higher diffusivity within the ECS[74]. SWCNTs provide a unique platform for single particle tracking due to their length/width ratio and higher surface area to volume ratio, which as mentioned previously in section 4.4.1.4, can alter surface functionality and diffusive ability. SWCNTs couple well with SPT's key benefit of long time scaled, localized tracking, and have complimented MPT findings in the field that show ECS widths are much larger than previously expected[77,269].

4.4.2.3.2 Multiple Particle Tracking

MPT is like SPT in that it also uses bright-field or epifluorescence microscopy to image and track Brownian motion of particles within a sample. The principal difference is that MPT tracks the movement of up to thousands of nanoparticles simultaneously with high resolution[270,271]. It is a high throughput extension of SPT. Experimentally, MPT typically involves *in vivo* injection or *ex vivo* topical application of fluorescent nanoparticles that are subsequently tracked via microscopy[68]. Open-source software packages, such as Fiji ImageJ [272] can then be used to calculate the trajectory coordinates and MSD values for each nanoparticle. MPT has been applied across a variety of use cases to probe the brain microstructure. As discussed previously, MPT studies have identified the range of available pore sizes in the brain for nanoprobes to access[77]. MPT has been used to study changes in diffusion in response to varying degrees of insult or stimuli, showing that for example, increased disease severity results in increased diffusive capability in the presence of ischemia[31]. More recent work has demonstrated that MPT can be used to study development-based structural changes of the ECS, finding reduced diffusivity and effective ECS pore size with increasing age during normal development[68]. There is strong potential for MPT to also probe diffusion characteristics associated with the mechanisms of pathological aging, such as the development of diffusion anisotropy which is clinically seen in patients with early onset Alzheimer's disease. The larger trajectory space occupied by MPT experiments is inherently useful for probing diffusion behavior across different brain regions, further uncovering the heterogeneity of the brain microenvironment.

One of the primary applications of MPT has been to identify design parameters of nano-based drug and gene delivery systems for improved efficacy in treating brain disease. It was initially accepted that 70 nm was the cutoff for the hydrodynamic diameter of any delivery vehicle to the brain. Later MPT studies in *ex vivo* human brain tissue and *in vivo* mouse brain tissue showed nanoparticles up to 114nm in diameter diffused through the tissue, without protein adhesion or other unfavorable interactions (e.g., electrostatic) with the brain microenvironment, when coated with a dense layer of PEG[77]. This finding doubled the size of a nanoparticle that could be used to effectively penetrate within the brain, which had significant implications for enhanced drug delivery to the brain. In *ex vivo* and *in vivo* rat brain tumor tissue, PEG coated nanoparticles diffused further relative to non-coated nanoparticles, leading to delayed tumor growth[252]. Further studies in tumors have shown a variety of polymer-based nanoparticles up to 100nm in diameter can penetrate within the brain parenchyma when nanoparticles are designed to maximize diffusion based on MPT studies[253,254,273].

4.4.2.3.3 Comparison of Particle Tracking Methods

It should be evident that both SPT and MPT are viable methods for probing ECS properties, with unique advantages and disadvantages depending on the experimental context. For example, MPT can track and average particle diffusion of hundreds of particles over larger areas and trajectory spaces. Recalling Figure 1 (Section 1.1), the brain ECS is narrow and tortuous with dead-end domains. MPT is useful in handling and accounting for this heterogeneity in ECS shape and geometry over entire regions (Figure 11A)[68]. Sampling the motion of multiple particles in a small volume also allows for more power in predicting particle behavior. For example, data from MPT studies in hydrogels and *ex vivo* brain slices have been used to predict the effective nanoparticle size and nanoparticle surface functionality once in a biological environment [67] and predict the biological age of the brain[68]. One drawback to MPT is that tracking more particles within a volume limits the time scale of tracking experiments to several seconds. Another drawback to MPT is the error associated with trajectory discontinuity and overlap. MPT data is extracted from live-video fluorescence microscopy that links together the particle trajectories, so even with fast frame rates of 10Hz or greater, rapidly diffusing particles are more likely to move out of frame and not accurately be linked one frame to another. Software plugins built to quantify time-dependent MSD profiles from MPT experiments can easily generate overlapped trajectories and require iterative optimization steps to ensure

accurate parsing of trajectories. Tracking singular trajectories is one way of addressing this issue. Furthermore, SPT is useful in tracking particles over longer time scales such as tens of minutes. There is control over localized probing, where heterogeneity in nanoparticle behavior for a single nanoparticle can be better quantified (Figure 11B)[79]. However, SPT requires a larger number of videos to be acquired to capture the heterogeneous geometry of the ECS across or within brain regions. Additionally, SPT is less efficient at generating predictive data on particle motion, as multiple trajectories are needed to predict diffusional differences using machine learning interfaces.

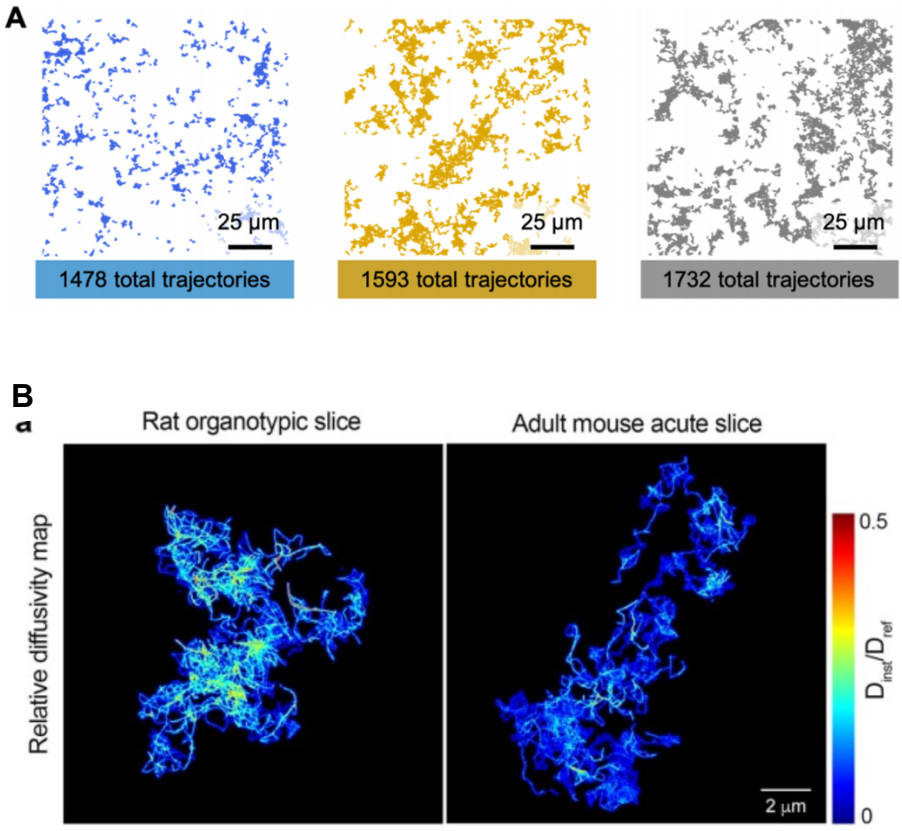

Figure 4.11. (A) Multiple-particle tracking of PS-PEG nanoparticles in *ex vivo* rat brain slices treated with three different ECM-modifying enzymes (yellow, gray) compared to non-treated slices (blue), highlighting the large number of trajectories sampled in x-y space and the increased number of trajectories in response to enzyme-mediated clearance of the ECM. Adapted and reprinted with permission from McKenna *et al.*(70). (B) SPT of a single carbon nanotube in a rat organotypic slice (cultured tissue, structurally and morphologically recovered from extraction event) versus the trajectory within an adult mouse acute slice (immediately following tissue extraction). SPT diffusion heatmap provides evidence of microstructural remodeling during culture time and highlights resulting local variations in diffusion. Adapted and reprinted with permission from (188).

There are important engineering considerations relevant to both tracking methods. Nanoparticle populations can have variability in particle sizes and often diffusion studies are performed assuming an averaged, effective diameter. Therefore, it is important that nanoparticle formulations maintain sufficiently low polydispersity index (PDI < 0.1), so that the observed diffusion behavior can confidently be attributed to an accurate average hydrodynamic diameter. From a data analysis standpoint, MPT or SPT may be more useful depending on the trajectory feature of interest. For example, trajectory asymmetry is related to diffusion anisotropy, and this measurement could be affected by the error associated with overlapping or discontinuous trajectories. Features such as pore size or effective diffusivity may be more efficiently sampled by MPT due to the larger occupancy space. Finally, it is important to address that both particle tracking methods have shared disadvantages. Both MPT and SPT capture 2D frames of particle motion within 3D environments. Accomplishing 3D particle tracking is less common but certainly emergent in engineering literature for high-resolution analysis of mass transfer, separation processes and interfacial phenomena[274]. In the biological space, researchers have incorporated machine-learning methods to track particles within intracellular cytosol in 3D[275]. As both methods capture a powerful amount of data in tracking experiments, MPT and SPT have the potential to be complimentary techniques for quantifying particle fate, relying on their respective advantages to maximize data output and biological interpretation.

4.5 Applications of Artificial Intelligence and Machine Learning

As briefly mentioned in Section 4.2.3.2, AI/ML methods have recently been applied to MPT data from nanoprobes applied to the ECS, and the early results show promise for further integration of these techniques into research in the field. Artificial neural networks were trained on MPT data from hydrogels and rat brain tissue to predict various aspects of nanoparticle behavior in ECS tissue. The model was able to predict nanoparticle size, surface functionality, stiffness, and viscosity demonstrating how AI/ML can be used to better understand changes in the ECS. Neurodevelopmental age has also been predicted from MPT data in the ECS. Using a gradient boosting decision tree, the chronological age of rat pups was predicted with high accuracy, a result which has relevance to eventual predictions for brain injury or disease. The statistical features which contributed most to the model were also calculated. The authors were able to leverage this information to understand differences between different ages, for example finding that

statistical features that indicated a slower moving or confined particle made the model more likely to predict an older age, with the opposite being true for lower age.

A primary application of AI/ML for SPT data has been classifying diffusion modes based on the particle trajectories. A study comparing convolutional neural networks (CNNs), which take raw trajectory data as inputs, and decision tress, which use statistical information about each trajectory, found that the CNNs performed better by a small margin on simulated data. Building off this, the same group used CNNs to generate 90% accuracy in predicting diffusion modes on synthetic data. A software package, TrajClassifier, can also be used on SPT data to segment and classify a trajectory's diffusion mode using a random forest model[276]**.** TrajClassifier has successfully classified between normal, anomalous, confined, and directed motion with an average error of 7.2%, demonstrating the utility of this approach for future SPT work. The authors were also able to calculate the importance of different statistical trajectory features to the model accuracy, finding the values of alpha, trappedness, and fractal dimension to contribute most significantly.

The insights generated from predictive models help make a connection between nanoprobe behavior and specific structural and biological changes in the ECS, maximizing how much information can be drawn from MPT studies. One can imagine the utility of predicting nanoparticle behavior to determine cellular or to identify biological changes that indicate disease onset or progression, such as deviation from normal aging. The early applications of AI/ML nanoprobe trajectory data highlights the potential of integrating these disciplines into the fields of engineering nanoprobes for surveying the brain microenvironment.

4.6 Conclusions and Future Directions

One area of active research is developing nanoparticles with improved solubility by utilizing molecular-based fluorescent organic nanoparticles as opposed to nanoparticles with inorganic coatings[277]. Design of materials that respond to enzymes have shown promising results in heart tissue[278] and for size-changing nanoparticles that penetrate tumor tissue[279]. Other work has been done showing that moderately rigid nanoparticles, as opposed to soft or hard nanoparticles, are capable of deforming while navigating their local environment, resulting in improved penetration in tumor and mucosal tissue[280].

Recent advances in imaging capabilities also have the potential for improving quantitative analysis of data from probing the brain ECS. Advances in super-resolution techniques for imaging single molecule switching and location, as well as imaging groups of molecules, have made live-cell imaging at nanoscale resolution more feasible[281]. Single-walled carbon nanotubes have also been used successfully as probes for super-resolution imaging while probing the ECS to determine how the ECS structure of adult mice changes in response to neurodegeneration. These studies found that the structural changes caused by neurodegeneration led to increased diffusivity of the ECS, increased width of the ECS, and degraded hyaluronan matrices in proximity of reactive microglia[74].

Current research efforts have solidified nanomaterials as a powerful tool for probing the brain ECS, and these recent research methods will only increase the potential applications. As more advances in nanomaterial design, imaging techniques, and AI/ML occur as a product of cutting-edge research, the role of the brain ECS will become increasingly understood.

Chapter 5. Conclusions and Forward-Looking Perspective

This thesis work develops the OWH brain slice platform to explore new and complex questions around the pathophysiology of neurologic disease. In this chapter, we summarize the major findings of each aspect of this thesis work and provide perspective on how our findings support critical directions the field.

In Chapter 2, we report the development of an OWH slice model of mitochondrial abnormalities using ROT exposure. The use of ROT in models of neurologic disease is not new, several studies across a range of model systems (*in vitro* to *in vivo*) use ROT to study hallmarks of Parkinson's disease, onset of neuropsychiatric disorders like schizophrenia, and other mitochondria-related disorders in the brain and how they affect various hallmarks of neuropathophysiology. To our knowledge, this is the first report using the mitochondrial toxin as an injury vehicle in whole-hemisphere slices from neonatal term-equivalent donors. We showed that mitochondrial dysfunction in neonatal brain tissue leads to region-dependent results (cell damage, microglial activation) that mirror responses to mitochondrial dysfunction in adult disease models, where deeper brain regions disproportionally experience progressive cell damage and neuronal death. We also showed that mitochondrial dysfunction alone is enough to significantly alter extracellular properties of ex vivo brain tissue.

Mitochondrial dysfunction is one of the most important hallmarks of neurologic disease that we can be studying right now, and our OWH ROT model is needed to study questions regarding the roles of mitochondria in neurologic injury and disease across the lifespan. Starting with the direct application of this work looking at mitochondrial dysfunction for neonatal populations, there are a variety of studies where this model and others like it can be used to answer pressing clinical questions related to worsened injury and disease outcomes. First, a model system specifically for neonatal populations is needed because, as introduced in Chapter 2, the energy landscape and metabolism of the developing brain is incredibly complex and also quite different than that of the adult brain[92,97]. Secondly, neonates are also at a risk of developing mitochondrial abnormalities prior to birth[84], and when factoring the incidence of pre-term or term birth injury, this type of model system could explore reasons for why the environmental factors and maternal co-morbidities driving mitochondrial dysfunction change susceptibility to birth injury. Additionally, while the OWH slices in this study were not cultured longer than 10 days, with the capability of new techniques to preserve viability of organotypic cultures from weeks to months in vitro[27,282] or culture tissue from older

donors, we could study how and why mitochondria mediate certain responses to birth injury or injury at other developmental stages and how they drive hallmarks of neurodevelopmental disorders. The OWH ROT model also enables mechanistic studies related to mitochondrial disease dynamics in a brain-representative system, where researchers could track the displacement and size distribution changes of live-labeled mitochondria in real time, explore differential cell uptake, and explore how mitophagy or mitochondrial transfer regulates gene expression in neighboring cell types. The paradigm of our OWH ROT model is not limited to neonatal brain injury, however, and the idea of inducing tunable mitochondrial function to explore the extent to which it alters responses of other diseases and disease hallmarks is an area of significant interest. One of the most impactful areas where this could be applied is to be able to distinguish tissue microenvironmental features of pathological aging, driven by progressive mitochondrial decline. Age is the biggest risk factor for ischemic stroke and neurodegenerative diseases, however how aging impacts the brain is shown to depend on a variety of non-disease or co-morbid lifestyle factors as diet and exercise, environment, socioeconomic status, and biological sex. What drives deviations from healthy aging to pathological aging is unclear and is a major exploratory area for models like our ROT OWH model to engineer and probe. For example, brain viscoelasticity is shown to decline with age in a sex-dependent manner[58] [58]and MPT could be applied to a ROT OWH model of mitochondrial dysfunction-driven aging to capture subtle changes in diffusive behavior associated with changing ECM stiffness and ECS viscosity. However, at the same time, this also introduces an “age-old” question regarding organotypic ex vivo brain cultures: to what extent does biological aging happen in culture? While this has not been explicitly quantified, some studies have confirmed presence of aging hallmarks, such as distinct microglial phenotypes that develop with age[36].

Chapter 3 shows broadly how ex vivo models can capture nuanced effects from combinatorial injury schemes that are previously demonstrated to recapitulate similar disease hallmarks on their own. Both OGD and ROT exposure in ex vivo slices, individually, are shown to drive microglial activation, modify the ECS, drive cell death, regulate expression of pro-inflammatory markers, and more[34,35,75]. Perhaps most importantly, this study showed that even though stimuli capable of producing the same responses were applied in series, the results were quite different and tunable, meaning that OWH slices can capture the subtlety of pre-existing conditions or co-morbidities on disease hallmarks and functional outcomes.

However, use of the OWH ROT model with OGD enabled a simple yet impactful study that, to our knowledge, had not yet been done, and opens the door to some interesting and critical work that can explore how two of the most fatal classes of neurologic disease are so commutable. While the cyclical nature of mitochondrial dysfunction and stroke risk and mortality are well-documented, no studies exist to quantify prior mitochondrial dysfunction changes the course of the injury. Rather, susceptibility studies focus on how the injury responses are mediated by mitochondria, and mitochondrial dysfunction as an outcome that leads to later-onset co-morbidity. These are also critical studies, but it is necessary to consider the other hand of the risk spectrum, where the pervasive nature of mitochondrial disorders that develop from several sources render multiple patient populations more susceptible to stroke fatality or neurodegenerative diseases. We also have an opportunity with our ROT OWH slice model, alone or in combination with models like OGD, to probe how co-morbidities or pre-existing conditions, affect pre-clinical screening efficacy of therapeutics.

Chapter 6. Contributions to-date

6.1 Rotenone increases susceptibility to secondary oxygen-glucose deprivation injury

Butler, B.*, Bennett, K.*, Brandon, OC., Kimerling, J., Schimek, N., Magoon, M. J., Boyle, P. M., and Nance, E.

*authors contributed equally to this work

Cerebral ischemia (CI) is a severe neurological injury characterized by lack of blood flow to the brain, the mortality and risk of which is exacerbated by pre-existing conditions, such as neurodegenerative disease. There are currently no preventative therapies or curative therapies for survivors that mitigate secondary stroke risk or onset of neurodegeneration. Therefore, understanding the pathophysiology of ischemic stroke in the presence of co-morbidities could reveal new therapies and improve standards-of-care for affected populations. Cellular metabolism, in the form of mitochondrial function, is a critical aspect of the pathophysiology of ischemic stroke. Mitochondrial dysfunction is well-documented as an acute metabolic outcome and therefore an emergent target for therapeutic intervention following ischemia However, it's less understood how pre-existing mitochondrial abnormalities alter this process, despite many of the primary risk factors for ischemic stroke being connected to mitochondrial abnormalities. Here, we used an organotypic whole-hemisphere slice model (OWH) of oxygen-glucose deprivation (OGD) to examine how the presence of mitochondrial inhibitor rotenone (ROT) changes the response of OWH slices to OGD injury. We first showed that the combined stimuli of OGD and ROT changes cell damage profiles compared to OGD alone, which was dependent on order and timing of the ROT insult. We found that the gene expression patterns varied differently between longer-term application (24h) or shorter-term application (2h prior, or simultaneously), where shorter-term application resulted in more OGD-like responses. We also quantified pro-inflammatory microglia morphology shifts, noting the most significant changes for shorter-term exposure groups. Both aligned with mitochondria image-based data specifically for microglia, showing a prominent connection between mitochondrial metabolism and pro-inflammatory activation, the closer ROT is applied relative to OGD. This study shows the effect of mitochondrial dysfunction on CI injury patterns and establishes precedent for more investigation with other model systems and the therapeutic benefit of mitochondria-targeting therapies in patients at risk for CI injury.

6.2 A rotenone organotypic whole-hemisphere slice model of mitochondrial abnormalities in the neonatal brain

Butler, B., Renney, M., Bennett, K., Charpentier, G., and Nance, E.

This chapter was published in full 14 November 2024 in the Journal of Biological Engineering **volume 18**, Article number: 67 (2024). DOI: https://doi.org/10.1186/s13036-024-00465-w

Mitochondrial abnormalities underscore a variety of neurologic injuries and diseases and are well-studied in adult populations. Clinical studies identify critical roles of mitochondria in a wide range of developmental brain injuries, but models that capture mitochondrial abnormalities in systems representative of the neonatal brain environment are lacking. Here, we develop an organotypic whole-hemisphere (OWH) brain slice model of mitochondrial dysfunction in the neonatal brain. We extended the utility of complex I inhibitor rotenone (ROT), canonically used in models of adult neurodegenerative diseases, to inflict mitochondrial damage in OWH slices from term-equivalent rats. We quantified whole-slice health over 6 days of exposure for a range of doses represented in ROT literature. We identified 50 nM ROT as a suitable exposure level for OWH slices to inflict injury without compromising viability. At the selected exposure level, we confirmed exposure- and time-dependent mitochondrial responses showing differences in mitochondrial fluorescence and nuclear localization using MitoTracker imaging in live OWH slices and dysregulated mitochondrial markers via RT-qPCR screening. We leveraged the regional structures present in OWH slices to quantify cell density and cell death in the cortex and the midbrain regions, observing higher susceptibilities to damage in the midbrain as a function of exposure and culture time. We supplemented these findings with analysis of microglia and mature neurons showing time-, region-, and exposure-dependent differences in microglial responses. We demonstrated changes in tissue microstructure as a function of region, culture time, and exposure level using live-video epifluorescence microscopy of extracellularly diffusing nanoparticle probes in live OWH slices. Our results highlight severity-, time-, and region-dependent responses and establish a complimentary model system of mitochondrial abnormalities for high-throughput or live-tissue experimental needs.

6.3 Nano-based probes for the brain extracellular microenvironment

Filteau, J.R.*, **Butler, B.*,** Schimek, N.*, and Nance, E.

*authors contributed equally to this work

This chapter is published in full in Nance, E. (eds) Engineering Biomaterials for Neural Applications. Springer, Cham. https://doi.org/10.1007/978-3-031-11409-0_2.

The brain is our most complex organ and governs all physiological function, from cognition and emotion to movement and stress response. Much of the brain's function is determined by complex interactions of cells within the brain parenchyma, the functional unit of brain tissue critical for supporting and protecting cells. In fact, trauma or disease to the brain parenchyma can result in a loss of cognitive function and, in severe cases, death. Several studies have shown microstructural changes to the brain parenchyma resulting from a variety of injury and disease states, such as traumatic brain injury (TBI), Alzheimer's and Parkinson's diseases, depression, and aging. As a result, brain microstructure has garnered significant attention in recent years from scientists and engineers as a neurological and micromechanical sink – an unexplored frontier for disease progression and a critical barrier to therapeutic delivery in the brain.

6.4 Organotypic whole hemisphere brain slice models to study the effects of donor age and oxygen-glucose-deprivation on the extracellular properties of cortical and striatal tissue

McKenna, M.*, Filteau, J.R.*, **Butler, B.,** Sluis, K., Chungyoun, M., Schimek, N., and Nance, E.

*authors contributed equally to this work

This article was published in full 13 June 2022 in the Journal of Biological Engineering **volume 16**, Article number: 14 (2022). DOI: https://doi.org/10.1186/s13036-022-00293-w

The brain extracellular environment is involved in many critical processes associated with neurodevelopment, neural function, and repair following injury. Organization of the extracellular matrix and properties of the extracellular space vary throughout development and across different brain regions, motivating the need for platforms that provide access to multiple brain regions at different stages of development. We demonstrate the utility of organotypic whole hemisphere brain slices as a platform to probe regional and developmental changes in the brain extracellular environment. We also leverage whole hemisphere brain slices to characterize the impact of cerebral ischemia on different regions of

brain tissue. Whole hemisphere brain slices taken from postnatal (P) day 10 and P17 rats retained viable, metabolically active cells through 14 days in vitro (DIV). Oxygen-glucose-deprivation (OGD), used to model a cerebral ischemic event in vivo, resulted in reduced slice metabolic activity and elevated cell death, regardless of slice age. Slices from P10 and P17 brains showed an oligodendrocyte and microglia-driven proliferative response after OGD exposure, higher than the proliferative response seen in DIV-matched normal control slices. Multiple particle tracking in oxygen-glucose-deprived brain slices revealed that oxygen-glucose-deprivation impacts the extracellular environment of brain tissue differently depending on brain age and brain region. In most instances, the extracellular space was most difficult to navigate immediately following insult, then gradually provided less hindrance to extracellular nanoparticle diffusion as time progressed. However, changes in diffusion were not universal across all brain regions and ages. We demonstrate whole hemisphere brain slices from P10 and P17 rats can be cultured up to two weeks in vitro. These brain slices provide a viable platform for studying both normal physiological processes and injury associated mechanisms with control over brain age and region. Ex vivo OGD impacted cortical and striatal brain tissue differently, aligning with preexisting data generated in in vivo models. These data motivate the need to account for both brain region and age when investigating mechanisms of injury and designing potential therapies for cerebral ischemia.

6.5 Engineering macromolecules with tunable mechanical and biophysical properties for cell-specific brain delivery

Wiegand, K., **Butler, B.**, Balistreri, G., Ramanan, S., Espinoza Marzal, R., Nance, E., Guironnet, D.
Manuscript in preparation.

Nanotherapeutic delivery to the brain is a considerable engineering challenge that faces several complex and interacting variables. As highlighted in Figure 1.1 of this text, the delivery of nanoparticles to the CNS and their ability to uptake into cells can be modulated by many forms of neuropathophysiological hallmarks and their associated stimuli. Furthermore, as discussed in Chapter 4, it is well-documented how nanoparticle physicochemical properties such as size, surface charge, surface chemistry, and shape affect drug delivery to the CNS and other biological tissues. However, to date, studies that seek to decouple the effects of particle mechanical properties are extremely limited, despite this likely playing a role in how nanoparticles interact with cell bodies and extracellular structures. Here, we seek to

characterize and quantify how nanoparticles with varied Young's Moduli diffusive differently in brain tissue. Using a novel AFM method developed by Rosa Espinoza Marzal, nanoparticle mechanical properties can be probed in solution to accurately attribute particle-tissue interactions to real mechanical properties. To contribute to this work, I performed MPT of four PLGA nanoparticles with distinct Young's Moduli, tuned by degree of cross-linking and molecular weight of the polymer. Interestingly, my preliminary findings showed proportional effective diffusion coefficients in ex vivo brain slices to the mechanical stiffness of the nanoparticle. I also quantified cell death and uptake of the mechanically-tuned PLGA particles in ex vivo slices and confirmed the particles reach microglia and do not cause significant cytotoxicity. Current work is focused on tracking nanoparticles in brain tissue around their glass transition temperature to determine the extent to which free thiol groups on PLGA particles interact with the proteoglycan structures in the ECM to better understand the extent to which mechanical properties are the pure driving force behind the trends in nanoparticle diffusion data.

Curriculum Vitae

Education and Training

The University of Washington, Seattle, 2020 – Present
Department: Chemical Engineering
GPA: 3.69 / 4.0
Expected graduation: Summer 2025

Politecnico di Milano (Milan Polytechnic University), 2019 – 2020
Department: Chemical and Materials Engineering "Giulio Natta"
Fulbright Research Fellow
Fellowship Advisor: Dr. Filippo Rossi (filippo.rossi@polimi.it)

Purdue University, 2015 – 2019
B.S. – Chemical Engineering
Concentration: Energy and the Environment
GPA: 3.76 / 4.0
Undergraduate Research Advisor: Dr. You-Yeon Won (yywon@purdue.edu)

Professional Experience

Graduate Research Assistant, Ph.D. Candidate, Advisor: Dr. Elizabeth Nance 01/2021 – Present
Department of Chemical Engineering, University of Washington

- **Thesis work:** nanoparticle behavior as a structural probe for microstructural dynamics in brain tissue during developmental injury and recovery
- **Relevant techniques:** confocal and epifluorescence microscopy of living and fixed nanoparticles and cells, nanoparticle surface chemistry and characterization, tissue culturing, immunohistochemistry, nucleic acid and organelle isolation from tissues, RT-qPCR, molecular biology assays
- Formal mentorship of four undergraduate student researchers with unique projects and lived experiences, specifically helping adapt wet lab and benchtop procedures in a cost-effective manner (< $200 total) for a disabled researcher with hand tremors and limited mobility, who has since become fully independent

Fulbright Research Fellow, Advisor: Dr. Filippo Rossi 09/2019 – 06/2020
Department of Chemical and Materials Engineering "Giulio Natta", Politecnico di Milano

- **Research project:** biologically-derived hydrogels for controlled drug delivery using micro-robot platforms
- Conducted literature reviews on suitable biopolymer candidates for controlled hydrogel release, as well as fabrication and tethering strategies to microscale delivery vehicles, optimized layer-by-layer (LbL) assembly of alginate-chitosan composite gels to balance structural integrity and drug loading, leading to published work
- **Relevant techniques:** hydrogel formulation and drug loading, in vitro release assays, FTIR
- Participated fully in Italian language for safety trainings, day-to-day work, and research communication

Undergraduate Student Researcher, Advisor: Dr. You-Yeon Won 08/2018 – 08/2019
Department of Chemical Engineering, Purdue University

- **Research project:** investigate the effects of micelle formulation parameters on air-water interfacial behavior as a surrogate for alveolar surface tension therapy in acute respiratory distress
- **Relevant techniques:** nanoprecipitation formulation of block-copolymer micelles, characterization using dynamic light scattering, surface tension measurements using Langmuir trough, and Brewster-angle microscopy
- Performed independent studies on the impact of formulation parameters on interfacial behavior, generating data that contributed to NSF funding

Technical Services & Manufacturing Sciences Intern 06/2018 – 08/2018
Eli Lilly Suzhou, Suzhou, China

- Developed and piloted a sampling study for quality control of empty insulin cartridges arriving from an external vendor
- Utilized process data from autoclave operations to model autoclave processes and explore energy-saving strategies for smaller-load sterilizations
- Cross-cultural communication and exchange: used Mandarin language skills to effectively train colleagues on sampling protocols for cartridge QC study; led one-day workshop on strategies for improving comprehension for English as a second language

Exchange Undergraduate Student Researcher, Advisor: Dr. Minhua Shao 02/2018 – 06/2018
Department of Chemical and Biological Engineering, Hong Kong University of Science and Technology

- **Project:** single-atom catalysis from earth-abundant metals for low-temperature fuel cell operation
- **Technical skills:** cyclic voltammetry and electrochemical characterizations
- Presented research to department faculty for credit at the end of the term

Engineering Intern, City of South Bend Indiana Summer 2017, 2019
Department of Public Works, Division of Engineering
Advisors: Dr. Kara Boyles and Sue-Ellen Doudrick, M.S.

- Projects: traffic volume mapping before and after construction projects, video analysis of sewer structural integrities, hydrologic mapping of watersheds to avoid pipe overflows and allocate preventative funding to the public in need
- Skills: Geographic Information Systems (GIS), hydrologic mapping and HEC-HMS software
- Invited back for second summer with raise following first internship

Honors, Awards, Certifications

2021	McCarthy Award for Excellence in Graduate Student Teaching, Chemical Engineering Department, University of Washington
2020	Catherine and Scott C. Roberts Distinguished Endowed Graduate Fellowship in Chemical Engineering, University of Washington
2019	Fulbright Study/Research Awardee to Italy
2017	Tau Beta Pi Engineering Honors Society, Inducted
2017	Omega Chi Epsilon Chemical Engineering Honors Society, Inducted
2015 – 2019	Purdue University Semester Honors (> 3.5 semester GPA, 6/8 Semesters) and Dean's List (8/8 Semesters)

2013 Indiana High School Tennis State Championships, 4th Place

Publications

*Underlined denotes first authorship

1. **Butler, B.,** Renney, M., Bennett, K., Charpentier, G., & Nance, E. (2024). A rotenone organotypic whole hemisphere brain slice model of mitochondrial abnormalities in the neonatal brain. *J Biol Eng,* (2024).
2. Filteau, J. R., **Butler, B.,** Schimek, N., & Nance, E. (2022). Nano-based probes for the brain extracellular environment. In *Engineering biomaterials for Neural Applications* (1st ed., Vol. 1). textbook, SPRINGER INTERNATIONAL PU.
3. McKenna, M., Filteau, J., **Butler, B.**, Schimek, N., Sluis, K., Chungyon, M. & Nance, E. Organotypic whole hemisphere brain slice models to study the effects of donor age and oxygen-glucose-deprivation on the extracellular properties of cortical and striatal tissue. *J Biol Eng* 16, (2022).
4. Bernasconi, R., Pizzetti, F., Rossetti, A., **Butler, B.**, Levi, M., Pané, S., Rossi, F. & Magagnini, L. Layer-by-Layer Fabrication of Hydrogel Microsystems for Controlled Drug Delivery From Untethered Microrobots. *Frontiers in Bioengineering and Biotechnology* 9, (2021).

Invited Talks and Oral Presentations

*Presenting author(s)

1. *Butler, B., Charpentier, G., Bennet, K., Renney, M., & Nance, E. (2024). An organotypic whole hemisphere slice model of mitochondrial abnormalities in the neonatal brain. AIChE Annual Meeting; San Diego, California; October 2024. *Engineered Biomimetic Tissue Models III: Microenvironmental Control for Biomimetic Models.*
2. *Butler, B., Charpentier, G., Bennet, K., Renney, M., & Nance, E. (2023). Rotenone exposure in organotypic whole-hemisphere brain slices to model mitochondrial abnormality in the neonatal brain. BMES Annual Meeting; Seattle, Washington; October 2023. *Neural Disease and Injury: Modeling and Therapeutics Track*
3. *Butler, B., Charpentier, G., Bennet, K., Renney, M., & Nance, E. (2022). Probing Brain Structure-Function Relationships Using Organotypic Whole-Hemisphere Slice Models and Multiple Particle Tracking Technology. AIChE Annual Meeting; Phoenix, Arizona; November 2022. *Nanotechnology approaches to diagnostics, implants, templating and assembly*

Poster Presentations

*Presenting author(s)

1. ***Butler, B.**, Charpentier, G., Bennet, K., Renney, M., & Nance, E. (2024). A rotenone organotypic whole-hemisphere brain slice model of mitochondrial abnormalities in the neonatal brain. University of Washington Chemical Engineering Graduate Student Symposium Poster Session
2. ***Butler, B.**, *Floryanzia, F., & *Jin, Zheyu (Ruby). *Ex-vivo* platforms for screening nanotherapeutic transport and efficacy in the brain. University of Washington Chemical Engineering Graduate Student Recruitment Poster Session
3. ***Butler, B.,** Charpentier, G., Bennet, K., Renney, M., & Nance, E. (2022). Probing brain microstructural remodeling using nanotechnology in stimuli-responsive organotypic whole-hemisphere slice models and parallel hydrogel systems. University of Washington Chemical Engineering Graduate Symposium Student Poster Session
4. **Butler, B.,** *Filteau, J., McKenna, M., & Nance, E. (2021). Cell-cell interactions and extracellular matrix structure in tissue models of acute and chronic brain disease/injury. University of Washington Chemical Engineering Graduate Student Symposium Poster Session

Teaching Experience

Spring 2024	University of Washington, Department of Chemical Engineering, Teaching Assistant for Material and Energy Balances
Spring 2022	University of Washington, Department of Chemical Engineering, Teaching Assistant for Material and Energy Balances
Spring 2021	University of Washington, Department of Chemical Engineering, Teaching Assistant for Material and Energy Balances, *McCarthy Award for Excellence in Graduate Student Teaching Award Recipient*
Spring 2017, 2018	Purdue University, College of Engineering, Teaching Assistant for Introductory Engineering Programming Course ENGR 132; Advisor: Dr. Michele Strutz

Service

Spring 2024	Volunteer; UW College of Engineering, Discovery Days
Spring 2022 – 2024	Volunteer; Women in Chemical Engineering; Introduce a Girl Outreach Series
Spring 2021 – 2023	Representative; ACES; Chemical Engineering Graduate Student Recruitment
Autumn 2021	Co-chair and organizer; Association of Chemical Engineering Graduate Students (ACES) Graduate Student Symposium; Department of Chemical Engineering, University of Washington
2018 – 2019	Tau Beta Pi Honors Society Purdue Chapter, Internal Affairs Chair
2017 – 2019	Omega Chi Epsilon Purdue Chapter, Tutoring Chair

Formal Mentorship Experience

1. Jay Kimerling, Chemical Engineering B.S. (Expected 06/2027) 10/2024 – Present
2. Kristin Bennett, Chemical Engineering (Expected 06/2025) 01/2022 – Present
3. Malcolm Renney, Chemical Engineering B.S. (06/2024) 01/2022 – 06/2024
4. Gisele Charpentier, Chemical Engineering B.S. (06/2023) 06/2021 – 06/2023

Memberships

American Institute of Chemical Engineers
Biomedical Engineering Society
Tau Beta Pi
Omega Chi Epsilon
Fulbright Scholar Alumni Network

Language Proficiencies

In order of proficiency. † Denotes professional working proficiency.

1. Italian†
2. Spanish†
3. Chinese (Mandarin)†
4. Greek (Modern)
5. Arabic (Standard)

References

1. Gooch, C. L., Pracht, E. & Borenstein, A. R. The burden of neurological disease in the United States: A summary report and call to action. *Ann Neurol* **81**, 479–484 (2017).
2. Su, X. *et al.* Dementia increases the risk of death in stroke patients: A retrospective cohort-based risk score model study. *Journal of Stroke and Cerebrovascular Diseases* **32**, 107337 (2023).
3. Pinho, J. *et al.* Incident stroke in patients with Alzheimer's disease: systematic review and meta-analysis. *Sci Rep* **11**, 16385 (2021).
4. Martin, L. J., Wong, M. & Hanaford, A. Neonatal Brain Injury and Genetic Causes of Adult-Onset Neurodegenerative Disease in Mice Interact With Effects on Acute and Late Outcomes. *Front Neurol* **10**, (2019).
5. Razaz, N. *et al.* Pre-pregnancy and pregnancy disorders, pre-term birth and the risk of cerebral palsy: a population-based study. *Int J Epidemiol* **52**, 1766–1773 (2023).
6. Kuring, J. K., Mathias, J. L. & Ward, L. Risk of Dementia in persons who have previously experienced clinically-significant Depression, Anxiety, or PTSD: A Systematic Review and Meta-Analysis. *J Affect Disord* **274**, 247–261 (2020).
7. Curtis, C., Zhang, M., Liao, R., Wood, T. & Nance, E. Systems-level thinking for nanoparticle-mediated therapeutic delivery to neurological diseases. *WIREs Nanomedicine and Nanobiotechnology* **9**, (2017).
8. Liu, B. & Hong, J.-S. Role of Microglia in Inflammation-Mediated Neurodegenerative Diseases: Mechanisms and Strategies for Therapeutic Intervention. *Journal of Pharmacology and Experimental Therapeutics* **304**, 1–7 (2003).
9. Johnson, V. E. *et al.* Inflammation and white matter degeneration persist for years after a single traumatic brain injury. *Brain* **136**, 28–42 (2013).
10. Velu, L. *et al.* Early rise of glutamate-glutamine levels in mild cognitive impairment: Evidence for emerging excitotoxicity. *Journal of Neuroradiology* **51**, 168–175 (2024).
11. KETY, S. S. THE GENERAL METABOLISM OF THE BRAIN IN VIVO. in *Metabolism of the Nervous System* 221–237 (Elsevier, 1957). doi:10.1016/B978-0-08-009062-7.50026-6.
12. Attwell, D. & Laughlin, S. B. An Energy Budget for Signaling in the Grey Matter of the Brain. *Journal of Cerebral Blood Flow & Metabolism* **21**, 1133–1145 (2001).
13. Leaw, B. *et al.* Mitochondria, Bioenergetics and Excitotoxicity: New Therapeutic Targets in Perinatal Brain Injury. *Front Cell Neurosci* **11**, (2017).
14. Bader, V. & Winklhofer, K. F. Mitochondria at the interface between neurodegeneration and neuroinflammation. *Semin Cell Dev Biol* **99**, 163–171 (2020).
15. Joshi, A. U. *et al.* Fragmented mitochondria released from microglia trigger A1 astrocytic response and propagate inflammatory neurodegeneration. *Nat Neurosci* **22**, 1635–1648 (2019).
16. Prabakaran, S. *et al.* Mitochondrial dysfunction in schizophrenia: evidence for compromised brain metabolism and oxidative stress. *Mol Psychiatry* **9**, 684–697 (2004).
17. Niatsetskaya, Z. V. *et al.* The Oxygen Free Radicals Originating from Mitochondrial Complex I Contribute to Oxidative Brain Injury Following Hypoxia–Ischemia in Neonatal Mice. *The Journal of Neuroscience* **32**, 3235–3244 (2012).
18. Beal, M. F. Mitochondria take center stage in aging and neurodegeneration. *Annals of Neurology* vol. 58 495–505 Preprint at https://doi.org/10.1002/ana.20624 (2005).

19. Velu, L. *et al.* Early rise of glutamate-glutamine levels in mild cognitive impairment: Evidence for emerging excitotoxicity. *Journal of Neuroradiology* **51**, 168–175 (2024).
20. Chauhan, A. *et al.* Brain region-specific deficit in mitochondrial electron transport chain complexes in children with autism. *J Neurochem* **117**, 209–220 (2011).
21. Zhao, T. *et al.* Associations of Mitochondrial Function, Stress, and Neurodevelopmental Outcomes in Early Life: A Systematic Review. *Dev Neurosci* **44**, 438–454 (2022).
22. Kasala, S. *et al.* Exposure to Morphine and Caffeine Induces Apoptosis and Mitochondrial Dysfunction in a Neonatal Rat Brain. *Front Pediatr* **8**, (2020).
23. Chong, M. R. *et al.* Mitochondrial DNA Copy Number as a Marker and Mediator of Stroke Prognosis. *Neurology* **98**, (2022).
24. Humpel, C. Organotypic brain slice cultures: A review. *Neuroscience* **305**, 86–98 (2015).
25. Gähwiler, B. Organotypic slice cultures: a technique has come of age. *Trends Neurosci* **20**, 471–477 (1997).
26. Bak, A. *et al.* Human organotypic brain slice cultures: a detailed and improved protocol for preparation and long-term maintenance. *J Neurosci Methods* **404**, 110055 (2024).
27. Wilhelmi, E. *et al.* Organotypic Brain-slice Cultures from Adult Rats: Approaches for a Prolonged Culture Time. *Alternatives to Laboratory Animals* **30**, 275–283 (2002).
28. Croft, C. L., Futch, H. S., Moore, B. D. & Golde, T. E. Organotypic brain slice cultures to model neurodegenerative proteinopathies. *Mol Neurodegener* **14**, 45 (2019).
29. Delbridge, A. R. D. *et al.* Organotypic Brain Slice Culture Microglia Exhibit Molecular Similarity to Acutely-Isolated Adult Microglia and Provide a Platform to Study Neuroinflammation. *Front Cell Neurosci* **14**, (2020).
30. Holthoff, K. & Witte, O. W. Intrinsic optical signals in vitro: a tool to measure alterations in extracellular space with two-dimensional resolution. *Brain Res Bull* **47**, 649–655 (1998).
31. Joseph, A. *et al.* Nanoparticle-microglial interaction in the ischemic brain is modulated by injury duration and treatment. *Bioeng Transl Med* **5**, e10175 (2020).
32. Xu, N., Wong, M., Balistreri, G. & Nance, E. Neonatal Pharmacokinetics and Biodistribution of Polymeric Nanoparticles and Effect of Surfactant. *Pharmaceutics* **15**, 1176 (2023).
33. Liao, R., Wood, T. R. & Nance, E. Superoxide dismutase reduces monosodium glutamate-induced injury in an organotypic whole hemisphere brain slice model of excitotoxicity. *J Biol Eng* **14**, 3 (2020).
34. Nguyen, N. P. *et al.* Brain Tissue-Derived Extracellular Vesicle Mediated Therapy in the Neonatal Ischemic Brain. *Int J Mol Sci* **23**, 620 (2022).
35. Butler, B., Renney, M., Bennett, K., Charpentier, G. & Nance, E. A rotenone organotypic whole hemisphere slice model of mitochondrial abnormalities in the neonatal brain. *J Biol Eng* **18**, 67 (2024).
36. Njie, eMalick G. *et al.* Ex vivo cultures of microglia from young and aged rodent brain reveal age-related changes in microglial function. *Neurobiol Aging* **33**, 195.e1-195.e12 (2012).
37. Wood, T. R. *et al.* A ferret brain slice model of oxygen–glucose deprivation captures regional responses to perinatal injury and treatment associated with specific microglial phenotypes. *Bioeng Transl Med* **7**, (2022).
38. Dahl, V. *et al.* Characterization of a mGluR5 Knockout Rat Model with Hallmarks of Fragile X Syndrome. *Life* **12**, 1308 (2022).

39. Jin, Z. R. *et al.* Multi-modal screening for synergistic neuroprotection of extremely preterm brain injury. Preprint at https://doi.org/10.1101/2025.04.25.650638 (2025).
40. Dauth, S. *et al.* Extracellular matrix protein expression is brain region dependent. *Journal of Comparative Neurology* **524**, 1309–1336 (2016).
41. Griffiths, D. R., Jenkins, T. M., Addington, C. P., Stabenfeldt, S. E. & Lifshitz, J. Extracellular matrix proteins are time-dependent and regional-specific markers in experimental diffuse brain injury. *Brain Behav* **10**, (2020).
42. Sethi, M. K. & Zaia, J. Extracellular matrix proteomics in schizophrenia and Alzheimer's disease. *Anal Bioanal Chem* **409**, 379–394 (2017).
43. Griffiths, D. R., Jenkins, T. M., Addington, C. P., Stabenfeldt, S. E. & Lifshitz, J. Extracellular matrix proteins are time-dependent and regional-specific markers in experimental diffuse brain injury. *Brain Behav* **10**, (2020).
44. Kamali-Zare, P. & Nicholson, C. Brain extracellular space: geometry, matrix and physiological importance. *Basic Clin Neurosci* **4**, 282–6 (2013).
45. Lau, L. W., Cua, R., Keough, M. B., Haylock-Jacobs, S. & Yong, V. W. Pathophysiology of the brain extracellular matrix: a new target for remyelination. *Nat Rev Neurosci* **14**, 722–729 (2013).
46. Syková, E. The Extracellular Space in the CNS: Its Regulation, Volume and Geometry in Normal and Pathological Neuronal Function. *The Neuroscientist* **3**, 28–41 (1997).
47. Ayad, N. M. E., Kaushik, S. & Weaver, V. M. Tissue mechanics, an important regulator of development and disease. *Philos Trans R Soc Lond B Biol Sci* **374**, 20180215 (2019).
48. Nicholson, C. & Syková, E. Extracellular space structure revealed by diffusion analysis. *Trends Neurosci* **21**, 207–215 (1998).
49. Hrabětová, S., Hrabe, J. & Nicholson, C. Dead-Space Microdomains Hinder Extracellular Diffusion in Rat Neocortex during Ischemia. *The Journal of Neuroscience* **23**, 8351–8359 (2003).
50. Odackal, J. *et al.* Real-time Iontophoresis with Tetramethylammonium to Quantify Volume Fraction and Tortuosity of Brain Extracellular Space. *Journal of Visualized Experiments* (2017) doi:10.3791/55755.
51. Toole, B. P. Hyaluronan: from extracellular glue to pericellular cue. *Nat Rev Cancer* **4**, 528–539 (2004).
52. Elkin, B. S., Shaik, M. A. & Morrison, B. Fixed negative charge and the Donnan effect: a description of the driving forces associated with brain tissue swelling and oedema. *Philos Trans A Math Phys Eng Sci* **368**, 585–603 (2010).
53. Chaudhuri, O., Cooper-White, J., Janmey, P. A., Mooney, D. J. & Shenoy, V. B. Effects of extracellular matrix viscoelasticity on cellular behaviour. *Nature* **584**, 535–546 (2020).
54. Elosegui-Artola, A. The extracellular matrix viscoelasticity as a regulator of cell and tissue dynamics. *Curr Opin Cell Biol* **72**, 10–18 (2021).
55. Elosegui-Artola, A. The extracellular matrix viscoelasticity as a regulator of cell and tissue dynamics. *Curr Opin Cell Biol* **72**, 10–18 (2021).
56. Chaudhuri, O., Cooper-White, J., Janmey, P. A., Mooney, D. J. & Shenoy, V. B. Effects of extracellular matrix viscoelasticity on cellular behaviour. *Nature* **584**, 535–546 (2020).
57. Mattana, S., Caponi, S., Tamagnini, F., Fioretto, D. & Palombo, F. Viscoelasticity of amyloid plaques in transgenic mouse brain studied by Brillouin microspectroscopy and correlative Raman analysis. *J Innov Opt Health Sci* **10**, 1742001 (2017).

58. Sack, I. *et al.* The impact of aging and gender on brain viscoelasticity. *Neuroimage* **46**, 652–657 (2009).
59. Verkman, A. S. Diffusion in the extracellular space in brain and tumors. *Phys Biol* **10**, 045003 (2013).
60. Syková, E. The Extracellular Space in the CNS: Its Regulation, Volume and Geometry in Normal and Pathological Neuronal Function. *The Neuroscientist* **3**, 28–41 (1997).
61. Syková, E. *et al.* Learning deficits in aged rats related to decrease in extracellular volume and loss of diffusion anisotropy in hippocampus. *Hippocampus* **12**, 269–279 (2002).
62. Fang, Y. *et al.* Altered Tracer Distribution and Clearance in the Extracellular Space of the Substantia Nigra in a Rodent Model of Parkinson's Disease. *Front Neurosci* **11**, (2017).
63. Nance, E., Pun, S. H., Saigal, R. & Sellers, D. L. Drug delivery to the central nervous system. *Nat Rev Mater* **7**, 314–331 (2021).
64. Helmbrecht, H., Joseph, A., McKenna, M., Zhang, M. & Nance, E. Governing transport principles for nanotherapeutic application in the brain. *Curr Opin Chem Eng* **30**, 112–119 (2020).
65. Streitberger, K.-J. *et al.* Brain Viscoelasticity Alteration in Chronic-Progressive Multiple Sclerosis. *PLoS One* **7**, e29888 (2012).
66. Nicholson, C. & Tao, L. Hindered diffusion of high molecular weight compounds in brain extracellular microenvironment measured with integrative optical imaging. *Biophys J* **65**, 2277–2290 (1993).
67. Curtis, C. *et al.* Predicting: In situ nanoparticle behavior using multiple particle tracking and artificial neural networks. *Nanoscale* **11**, 22515–22530 (2019).
68. McKenna, M., Shackelford, D., Ferreira Pontes, H., Ball, B. & Nance, E. Multiple Particle Tracking Detects Changes in Brain Extracellular Matrix and Predicts Neurodevelopmental Age. *ACS Nano* **15**, 8559–8573 (2021).
69. Chenouard, N. *et al.* Objective comparison of particle tracking methods. *Nat Methods* **11**, 281–289 (2014).
70. Kaler, L. *et al.* Influenza A virus diffusion through mucus gel networks. *Commun Biol* **5**, 249 (2022).
71. Xu, Q. *et al.* Nanoparticle diffusion in, and microrheology of, the bovine vitreous ex vivo. *Journal of Controlled Release* **167**, 76–84 (2013).
72. Jin, H., Heller, D. A. & Strano, M. S. Single-Particle Tracking of Endocytosis and Exocytosis of Single-Walled Carbon Nanotubes in NIH-3T3 Cells. *Nano Lett* **8**, 1577–1585 (2008).
73. Birjiniuk, A. *et al.* Single particle tracking reveals spatial and dynamic organization of the *Escherichia coli* biofilm matrix. *New J Phys* **16**, 085014 (2014).
74. Soria, F. N. *et al.* Synucleinopathy alters nanoscale organization and diffusion in the brain extracellular space through hyaluronan remodeling. *Nat Commun* **11**, 3440 (2020).
75. McKenna, M. *et al.* Organotypic whole hemisphere brain slice models to study the effects of donor age and oxygen-glucose-deprivation on the extracellular properties of cortical and striatal tissue. *J Biol Eng* **16**, (2022).
76. Schimek, N. *et al.* High-fidelity predictions of diffusion in the brain microenvironment. *Biophys J* **123**, 3935–3950 (2024).
77. Nance, E. A. *et al.* A Dense Poly(Ethylene Glycol) Coating Improves Penetration of Large Polymeric Nanoparticles Within Brain Tissue. *Sci Transl Med* **4**, (2012).

78. Amsden, B. An Obstruction-Scaling Model for Diffusion in Homogeneous Hydrogels. *Macromolecules* **32**, 874–879 (1999).
79. Paviolo, C. *et al.* Nanoscale exploration of the extracellular space in the live brain by combining single carbon nanotube tracking and super-resolution imaging analysis. *Methods* **174**, 91–99 (2020).
80. Filteau, J. R., Butler, B. P., Schimek, N. & Nance, E. Nano-Based Probes for the Brain Extracellular Environment. in *Engineering Biomaterials for Neural Applications* 53–88 (Springer International Publishing, Cham, 2022). doi:10.1007/978-3-031-11409-0_2.
81. Hendgen-Cotta, U. B., Giorgio, V. & Hool, L. Mitochondria at the Crossroads of Survival and Demise. *Oxid Med Cell Longev* **2019**, 1–2 (2019).
82. Bélanger, M., Allaman, I. & Magistretti, P. J. Brain Energy Metabolism: Focus on Astrocyte-Neuron Metabolic Cooperation. *Cell Metab* **14**, 724–738 (2011).
83. Sokoloff, L. *et al.* THE [^{14} C]DEOXYGLUCOSE METHOD FOR THE MEASUREMENT OF LOCAL CEREBRAL GLUCOSE UTILIZATION: THEORY, PROCEDURE, AND NORMAL VALUES IN THE CONSCIOUS AND ANESTHETIZED ALBINO RAT [1]. *J Neurochem* **28**, 897–916 (1977).
84. Zhao, T. *et al.* Associations of Mitochondrial Function, Stress, and Neurodevelopmental Outcomes in Early Life: A Systematic Review. *Dev Neurosci* **44**, 438–454 (2022).
85. Hiebert, J. B., Shen, Q., Thimmesch, A. R. & Pierce, J. D. Traumatic Brain Injury and Mitochondrial Dysfunction. *Am J Med Sci* **350**, 132–138 (2015).
86. Lushchak, O., Strilbytska, O., Koliada, A. & Storey, K. B. An orchestrating role of mitochondria in the origin and development of post-traumatic stress disorder. *Front Physiol* **13**, (2023).
87. Yang, J.-L., Mukda, S. & Chen, S.-D. Diverse roles of mitochondria in ischemic stroke. *Redox Biol* **16**, 263–275 (2018).
88. Rosenfeld, M., Brenner-Lavie, H., Ari, S. G.-B., Kavushansky, A. & Ben-Shachar, D. Perturbation in Mitochondrial Network Dynamics and in Complex I Dependent Cellular Respiration in Schizophrenia. *Biol Psychiatry* **69**, 980–988 (2011).
89. D'Antoni, S. *et al.* Aberrant mitochondrial bioenergetics in the cerebral cortex of the *Fmr1* knockout mouse model of fragile X syndrome. *Biol Chem* **401**, 497–503 (2020).
90. Kennedy, C. & Sokoloff, L. An Adaptation of the Nitrous Oxide Method to the Study of the Cerebral Circulation in Children; Normal Values for Cerebral Blood Flow and Cerebral Metabolic Rate in Childhood1. *Journal of Clinical Investigation* **36**, 1130–1137 (1957).
91. Gogtay, N. *et al.* Dynamic mapping of human cortical development during childhood through early adulthood. *Proceedings of the National Academy of Sciences* **101**, 8174–8179 (2004).
92. Cacciatore, M., Grasso, E. A., Tripodi, R. & Chiarelli, F. Impact of glucose metabolism on the developing brain. *Front Endocrinol (Lausanne)* **13**, (2022).
93. Chugani, H. T., Phelps, M. E. & Mazziotta, J. C. Positron emission tomography study of human brain functional development. *Ann Neurol* **22**, 487–497 (1987).
94. Demarest, T. G. *et al.* Sex dependent alterations in mitochondrial electron transport chain proteins following neonatal rat cerebral hypoxic-ischemia. *J Bioenerg Biomembr* **48**, 591–598 (2016).

95. Odorcyk, F. K. *et al.* Differential Age-Dependent Mitochondrial Dysfunction, Oxidative Stress, and Apoptosis Induced by Neonatal Hypoxia-Ischemia in the Immature Rat Brain. *Mol Neurobiol* **58**, 2297–2308 (2021).
96. Guevara, R. *et al.* Sex-dependent differences in aged rat brain mitochondrial function and oxidative stress. *Free Radic Biol Med* **46**, 169–175 (2009).
97. Arias-Reyes, C., Losantos-Ramos, K., Gonzales, M., Furrer, D. & Soliz, J. NADH-linked mitochondrial respiration in the developing mouse brain is sex-, age- and tissue-dependent. *Respir Physiol Neurobiol* **266**, 156–162 (2019).
98. González-Pardo, H., Arias, J. L., Gómez-Lázaro, E., López Taboada, I. & Conejo, N. M. Sex-Specific Effects of Early Life Stress on Brain Mitochondrial Function, Monoamine Levels and Neuroinflammation. *Brain Sci* **10**, 447 (2020).
99. Bajic, D., Commons, K. G. & Soriano, S. G. Morphine-enhanced apoptosis in selective brain regions of neonatal rats. *International Journal of Developmental Neuroscience* **31**, 258–266 (2013).
100. Bastian, T. W., Rao, R., Tran, P. V & Georgieff, M. K. The Effects of Early-Life Iron Deficiency on Brain Energy Metabolism. *Neurosci Insights* **15**, 263310552093510 (2020).
101. Davies, K. L. *et al.* Development of cerebral mitochondrial respiratory function is impaired by thyroid hormone deficiency before birth in a region-specific manner. *The FASEB Journal* **35**, (2021).
102. Cheng, X.-Y. *et al.* Human iPSCs derived astrocytes rescue rotenone-induced mitochondrial dysfunction and dopaminergic neurodegeneration in vitro by donating functional mitochondria. *Transl Neurodegener* **9**, 13 (2020).
103. Ishido, M., Suzuki, J. & Masuo, Y. Neonatal rotenone lesions cause onset of hyperactivity during juvenile and adulthood in the rat. *Toxicol Lett* **266**, 42–48 (2017).
104. Varga, T. G. *et al.* Haloperidol rescues the schizophrenia-like phenotype in adulthood after rotenone administration in neonatal rats. *Psychopharmacology (Berl)* **238**, 2569–2585 (2021).
105. Radad, K., Rausch, W.-D. & Gille, G. Rotenone induces cell death in primary dopaminergic culture by increasing ROS production and inhibiting mitochondrial respiration. *Neurochem Int* **49**, 379–386 (2006).
106. Fan, L.-W. *et al.* Neonatal exposure to lipopolysaccharide enhances vulnerability of nigrostriatal dopaminergic neurons to rotenone neurotoxicity in later life. *Neurobiol Dis* **44**, 304–316 (2011).
107. Ullrich, C. & Humpel, C. Rotenone Induces Cell Death of Cholinergic Neurons in an Organotypic Co-Culture Brain Slice Model. *Neurochem Res* **34**, 2147–2153 (2009).
108. Tien, L.-T. *et al.* Neonatal exposure to lipopolysaccharide enhances accumulation of α-synuclein aggregation and dopamine transporter protein expression in the substantia nigra in responses to rotenone challenge in later life. *Toxicology* **308**, 96–103 (2013).
109. Fairley, L. H., Wong, J. H. & Barron, A. M. Mitochondrial Regulation of Microglial Immunometabolism in Alzheimer's Disease. *Front Immunol* **12**, (2021).
110. S. Ten, V. *et al.* Mitochondrial Dysfunction and Permeability Transition in Neonatal Brain and Lung Injuries. *Cells* **10**, 569 (2021).
111. Ayala, A. Mitochondrial toxins and neurodegenerative diseases. *Frontiers in Bioscience* **12**, 986 (2007).

112. Higgins, Jr. , D. S. & Greenamyre, J. T. [^{3} H]Dihydrorotenone Binding to NADH: Ubiquinone Reductase (Complex I) of the Electron Transport Chain: An Autoradiographic Study. *The Journal of Neuroscience* **16**, 3807–3816 (1996).
113. Sherer, T. B., Kim, J.-H., Betarbet, R. & Greenamyre, J. T. Subcutaneous Rotenone Exposure Causes Highly Selective Dopaminergic Degeneration and α-Synuclein Aggregation. *Exp Neurol* **179**, 9–16 (2003).
114. Goh, T. Y., Basah, S. N., Yazid, H., Aziz Safar, M. J. & Ahmad Saad, F. S. Performance analysis of image thresholding: Otsu technique. *Measurement* **114**, 298–307 (2018).
115. Nance, E. Brain-Penetrating Nanoparticles for Analysis of the Brain Microenvironment. in 91–104 (2017). doi:10.1007/978-1-4939-6840-4_6.
116. Curtis, C., Rokem, A. & Nance, E. diff_classifier: Parallelization of multi-particle tracking video analyses. *J Open Source Softw* **4**, 989 (2019).
117. Testa, C. M., Sherer, T. B. & Greenamyre, J. T. Rotenone induces oxidative stress and dopaminergic neuron damage in organotypic substantia nigra cultures. *Molecular Brain Research* **134**, 109–118 (2005).
118. Sherer, T. B., Betarbet, R., Kim, J.-H. & Greenamyre, J. T. Selective microglial activation in the rat rotenone model of Parkinson's disease. *Neurosci Lett* **341**, 87–90 (2003).
119. Isaev, N. K., Stelmashook, E. V, Ruscher, K., Andreeva, N. A. & Zorov, D. B. Menadione reduces rotenone-induced cell death in cerebellar granule neurons. . *Neuroreport* **15**, 2227–2231 (2004).
120. Gao, H.-M., Hong, J.-S., Zhang, W. & Liu, B. Distinct Role for Microglia in Rotenone-Induced Degeneration of Dopaminergic Neurons. *The Journal of Neuroscience* **22**, 782–790 (2002).
121. Goswami, P. *et al.* Endoplasmic Reticulum Stress Plays a Key Role in Rotenone-Induced Apoptotic Death of Neurons. *Mol Neurobiol* **53**, 285–298 (2016).
122. Wang, T. *et al.* Neuroprotective effects of Danshensu on rotenone-induced Parkinson's disease models in vitro and in vivo. *BMC Complement Med Ther* **20**, 20 (2020).
123. Pakrashi, S., Chakraborty, J. & Bandyopadhyay, J. Neuroprotective Role of Quercetin on Rotenone-Induced Toxicity in SH-SY5Y Cell Line Through Modulation of Apoptotic and Autophagic Pathways. *Neurochem Res* **45**, 1962–1973 (2020).
124. Emmrich, J. V., Hornik, T. C., Neher, J. J. & Brown, G. C. Rotenone induces neuronal death by microglial phagocytosis of neurons. *FEBS J* **280**, 5030–5038 (2013).
125. Savage, J. C., Carrier, M. & Tremblay, M.-È. Morphology of Microglia Across Contexts of Health and Disease. in 13–26 (2019). doi:10.1007/978-1-4939-9658-2_2.
126. Ansari, F. *et al.* How many molecules of mitochondrial complex I are in a cell? *Anal Biochem* **646**, 114646 (2022).
127. Khakh, B. S. & Sofroniew, M. V. Diversity of astrocyte functions and phenotypes in neural circuits. *Nat Neurosci* **18**, 942–952 (2015).
128. Wisnowski, J. L. *et al.* Brain Injury Outcomes after Adjuvant Erythropoietin Neuroprotection for Moderate or Severe Neonatal Hypoxic-Ischemic Encephalopathy: A Report from the HEAL Trial. *Dev Neurosci* 1–12 (2023) doi:10.1159/000534618.
129. Durán-Carabali, L. E. *et al.* Maternal environmental enrichment protects neonatal brains from hypoxic-ischemic challenge by mitigating brain energetic dysfunction and modulating glial cell responses. *Exp Neurol* **374**, 114713 (2024).

130. Anderova, M. *et al.* Cell Death/Proliferation and Alterations in Glial Morphology Contribute to Changes in Diffusivity in the Rat Hippocampus after Hypoxia—Ischemia. *Journal of Cerebral Blood Flow & Metabolism* **31**, 894–907 (2011).
131. Jayaraj, R. L. *et al.* Lycopodium Attenuates Loss of Dopaminergic Neurons by Suppressing Oxidative Stress and Neuroinflammation in a Rat Model of Parkinson's Disease. *Molecules* **24**, (2019).
132. Swarnkar, S., Tyagi, E., Agrawal, R., Singh, M. P. & Nath, C. A comparative study on oxidative stress induced by LPS and rotenone in homogenates of rat brain regions. *Environ Toxicol Pharmacol* **27**, 219–224 (2009).
133. Reinhard, S. M., Razak, K. & Ethell, I. M. A delicate balance: role of MMP-9 in brain development and pathophysiology of neurodevelopmental disorders. *Front Cell Neurosci* **9**, (2015).
134. Vafadari, B., Salamian, A. & Kaczmarek, L. <scp>MMP</scp> -9 in translation: from molecule to brain physiology, pathology, and therapy. *J Neurochem* **139**, 91–114 (2016).
135. Ethell, I. M. & Ethell, D. W. Matrix metalloproteinases in brain development and remodeling: Synaptic functions and targets. *J Neurosci Res* **85**, 2813–2823 (2007).
136. Chen, K., Wang, Y., Deng, X., Guo, L. & Wu, C. Extracellular matrix stiffness regulates mitochondrial dynamics through PINCH-1- and kindlin-2-mediated signalling. *Curr Res Cell Biol* **2**, 100008 (2021).
137. Gao, J. *et al.* Intracerebral fate of organic and inorganic nanoparticles is dependent on microglial extracellular vesicle function. *Nat Nanotechnol* **19**, 376–386 (2024).
138. Chehrehasa, F., Meedeniya, A. C. B., Dwyer, P., Abrahamsen, G. & Mackay-Sim, A. EdU, a new thymidine analogue for labelling proliferating cells in the nervous system. *J Neurosci Methods* **177**, 122–130 (2009).
139. Khalifa, A. R. M. *et al.* Sex-specific differences in mitochondria biogenesis, morphology, respiratory function, and ROS homeostasis in young mouse heart and brain. *Physiol Rep* **5**, (2017).
140. Rangaraju, V. *et al.* Pleiotropic Mitochondria: The Influence of Mitochondria on Neuronal Development and Disease. *The Journal of Neuroscience* **39**, 8200–8208 (2019).
141. Peferoen, L., Kipp, M., van der Valk, P., van Noort, J. M. & Amor, S. Oligodendrocyte-microglia cross-talk in the central nervous system. *Immunology* **141**, 302–313 (2014).
142. Fairley, L. H., Grimm, A. & Eckert, A. Mitochondria Transfer in Brain Injury and Disease. *Cells* **11**, 3603 (2022).
143. Meyer, N. & Rinholm, J. E. Mitochondria in Myelinating Oligodendrocytes: Slow and Out of Breath? *Metabolites* **11**, 359 (2021).
144. Mosconi, M. G. & Paciaroni, M. Treatments in Ischemic Stroke: Current and Future. *Eur Neurol* **85**, 349–366 (2022).
145. Virani, S. S. *et al.* Heart Disease and Stroke Statistics—2020 Update: A Report From the American Heart Association. *Circulation* **141**, (2020).
146. Cai, W. *et al.* Dysfunction of the neurovascular unit in ischemic stroke and neurodegenerative diseases: An aging effect. *Ageing Res Rev* **34**, 77–87 (2017).
147. Fan, H.-C., Lee, H.-F., Yue, C.-T. & Chi, C.-S. Clinical Characteristics of Mitochondrial Encephalomyopathy, Lactic Acidosis, and Stroke-Like Episodes. *Life* **11**, 1111 (2021).
148. Ng, Y. S. *et al.* Forecasting stroke-like episodes and outcomes in mitochondrial disease. *Brain* **145**, 542–554 (2022).

149. Liu, F., Lu, J., Manaenko, A., Tang, J. & Hu, Q. Mitochondria in Ischemic Stroke: New Insight and Implications. *Aging Dis* **9**, 924 (2018).
150. Tian, H. *et al.* Mitochondrial quality control in stroke: From the mechanisms to therapeutic potentials. *J Cell Mol Med* **26**, 1000–1012 (2022).
151. Li, Q. & Gao, S. Mitochondrial Dysfunction in Ischemic Stroke. in 201–221 (2017). doi:10.1007/978-981-10-5804-2_10.
152. Gan, J. *et al.* Neuroprotective mechanisms of microglia in ischemic stroke: a review focused on mitochondria. *Mol Biol Rep* **52**, 355 (2025).
153. Miao, G. *et al.* Microglia promote inflammatory cell death upon neuronal mitochondrial impairment during neurodegeneration. *Nat Struct Mol Biol* (2025) doi:10.1038/s41594-025-01602-9.
154. Fields, R. ATP: an extracellular signaling molecule between neurons and glia. *Trends Neurosci* **23**, 625–633 (2000).
155. Nair, S. *et al.* Induction of Mitochondrial Fragmentation and Mitophagy after Neonatal Hypoxia–Ischemia. *Cells* **11**, 1193 (2022).
156. Gong, Z., Pan, J., Shen, Q., Li, M. & Peng, Y. Mitochondrial dysfunction induces NLRP3 inflammasome activation during cerebral ischemia/reperfusion injury. *J Neuroinflammation* **15**, 242 (2018).
157. Mondal, N. K. *et al.* Tetrahydrocurcumin epigenetically mitigates mitochondrial dysfunction in brain vasculature during ischemic stroke. *Neurochem Int* **122**, 120–138 (2019).
158. Huang, J. *et al.* The role of mitochondrial dynamics in cerebral ischemia-reperfusion injury. *Biomedicine & Pharmacotherapy* **162**, 114671 (2023).
159. Wen, B. *et al.* Preserving mitochondrial function by inhibiting GRP75 ameliorates neuron injury under ischemic stroke. *Mol Med Rep* **25**, 165 (2022).
160. Hummon, A. B., Lim, S. R., Difilippantonio, M. J. & Ried, T. Isolation and Solubilization of Proteins After TRI <scp>zol</scp> ® Extraction of RNA and DNA from Patient Material Following Prolonged Storage. *Biotechniques* **42**, 467–472 (2007).
161. Wu, P.-H. *et al.* Evolution of cellular morpho-phenotypes in cancer metastasis. *Sci Rep* **5**, 18437 (2015).
162. Lu, D. *et al.* Neuroprotective effect of lipopolysaccharides in a dual-hit rat pup model of preterm hypoxia–ischemia. *Neurosci Lett* **795**, 137033 (2023).
163. Gao, F., Chen, D., Hu, Q. & Wang, G. Rotenone Directly Induces BV2 Cell Activation via the p38 MAPK Pathway. *PLoS One* **8**, e72046 (2013).
164. Sarkar, S. *et al.* Mitochondrial impairment in microglia amplifies NLRP3 inflammasome proinflammatory signaling in cell culture and animal models of Parkinson's disease. *NPJ Parkinsons Dis* **3**, 30 (2017).
165. Montilla, A. *et al.* Role of Mitochondrial Dynamics in Microglial Activation and Metabolic Switch. *Immunohorizons* **5**, 615–626 (2021).
166. Solaini, G., Baracca, A., Lenaz, G. & Sgarbi, G. Hypoxia and mitochondrial oxidative metabolism. *Biochimica et Biophysica Acta (BBA) - Bioenergetics* **1797**, 1171–1177 (2010).
167. Lin, Y., Wang, Y. & Li, P. Mutual regulation of lactate dehydrogenase and redox robustness. *Front Physiol* **13**, (2022).
168. Tassinari, I. D. *et al.* Lactate Protects Microglia and Neurons from Oxygen–Glucose Deprivation/Reoxygenation. *Neurochem Res* **49**, 1762–1781 (2024).

169. Chenna, S., Koopman, W. J. H., Prehn, J. H. M. & Connolly, N. M. C. Mechanisms and mathematical modeling of ROS production by the mitochondrial electron transport chain. *American Journal of Physiology-Cell Physiology* **323**, C69–C83 (2022).
170. Kristián, T. Metabolic stages, mitochondria and calcium in hypoxic/ischemic brain damage. *Cell Calcium* **36**, 221–233 (2004).
171. Chandel, N. S. *et al.* Mitochondrial reactive oxygen species trigger hypoxia-induced transcription. *Proceedings of the National Academy of Sciences* **95**, 11715–11720 (1998).
172. Doege, K., Heine, S., Jensen, I., Jelkmann, W. & Metzen, E. Inhibition of mitochondrial respiration elevates oxygen concentration but leaves regulation of hypoxia-inducible factor (HIF) intact. *Blood* **106**, 2311–2317 (2005).
173. van Gisbergen, M. W. *et al.* Mitochondrial Dysfunction Inhibits Hypoxia-Induced HIF-1α Stabilization and Expression of Its Downstream Targets. *Front Oncol* **10**, (2020).
174. Semenza, G. L. Hypoxia-inducible factor 1: Regulator of mitochondrial metabolism and mediator of ischemic preconditioning. *Biochimica et Biophysica Acta (BBA) - Molecular Cell Research* **1813**, 1263–1268 (2011).
175. Hagen, T., Taylor, C. T., Lam, F. & Moncada, S. Redistribution of Intracellular Oxygen in Hypoxia by Nitric Oxide: Effect on HIF1α. *Science (1979)* **302**, 1975–1978 (2003).
176. Chandel, N. S. *et al.* Mitochondrial reactive oxygen species trigger hypoxia-induced transcription. *Proceedings of the National Academy of Sciences* **95**, 11715–11720 (1998).
177. Afridi, R., Kim, J.-H., Rahman, M. H. & Suk, K. Metabolic Regulation of Glial Phenotypes: Implications in Neuron–Glia Interactions and Neurological Disorders. *Front Cell Neurosci* **14**, (2020).
178. Xue, J. *et al.* Ischemic preconditioning-induced protective effect for promoting angiogenesis in renal ischemia-reperfusion injury by regulating miR-376c-3p/HIF-1α/VEGF axis in male rats. *Life Sci* **299**, 120357 (2022).
179. Dong, P., Li, Q. & Han, H. HIF-1α in cerebral ischemia (Review). *Mol Med Rep* **25**, 41 (2021).
180. Guo, Y. Role of HIF-1a in regulating autophagic cell survival during cerebral ischemia reperfusion in rats. *Oncotarget* **8**, 98482–98494 (2017).
181. Giordano, S. *et al.* Bioenergetic adaptation in response to autophagy regulators during rotenone exposure. *J Neurochem* **131**, 625–633 (2014).
182. Legros, F., Lombès, A., Frachon, P. & Rojo, M. Mitochondrial Fusion in Human Cells Is Efficient, Requires the Inner Membrane Potential, and Is Mediated by Mitofusins. *Mol Biol Cell* **13**, 4343–4354 (2002).
183. Vannucci, R. C., Towfighi, J. & Vannucci, S. J. Secondary Energy Failure after Cerebral Hypoxia–Ischemia in the Immature Rat. *Journal of Cerebral Blood Flow & Metabolism* **24**, 1090–1097 (2004).
184. Cai, W. *et al.* Dysfunction of the neurovascular unit in ischemic stroke and neurodegenerative diseases: An aging effect. *Ageing Res Rev* **34**, 77–87 (2017).
185. Rinaldi, C. *et al.* Oxidative Stress and the Neurovascular Unit. *Life* **11**, 767 (2021).
186. Miyazaki, I. *et al.* Chronic Systemic Exposure to Low-Dose Rotenone Induced Central and Peripheral Neuropathology and Motor Deficits in Mice: Reproducible Animal Model of Parkinson's Disease. *Int J Mol Sci* **21**, 3254 (2020).
187. Koopman, W. J. H. *et al.* Mitochondrial network complexity and pathological decrease in complex I activity are tightly correlated in isolated human complex I deficiency. *American Journal of Physiology-Cell Physiology* **289**, C881–C890 (2005).

188. Distelmaier, F. *et al.* Mitochondrial complex I deficiency: from organelle dysfunction to clinical disease. *Brain* **132**, 833–842 (2008).
189. Dawson, T. M. & Dawson, V. L. Mitochondrial Mechanisms of Neuronal Cell Death: Potential Therapeutics. *Annu Rev Pharmacol Toxicol* **57**, 437–454 (2017).
190. Bonkhoff, A. K. *et al.* Generative lesion pattern decomposition of cognitive impairment after stroke. *Brain Commun* **3**, (2021).
191. Szarka, N. *et al.* Single Mild Traumatic Brain Injury Induces Persistent Disruption of the Blood-Brain Barrier, Neuroinflammation and Cognitive Decline in Hypertensive Rats. *Int J Mol Sci* **20**, (2019).
192. Thal, D. R., Griffin, W. S. T. & Braak, H. Parenchymal and vascular Aβ-deposition and its effects on the degeneration of neurons and cognition in Alzheimer's disease. *J Cell Mol Med* **12**, 1848–1862 (2008).
193. Smith, A. J., Yao, X., Dix, J. A., Jin, B.-J. & Verkman, A. S. Test of the 'glymphatic' hypothesis demonstrates diffusive and aquaporin-4-independent solute transport in rodent brain parenchyma. *Elife* **6**, (2017).
194. Hrabetova, S., Cognet, L., Rusakov, D. A. & Nägerl, U. V. Unveiling the Extracellular Space of the Brain: From Super-resolved Microstructure to *In Vivo* Function. *The Journal of Neuroscience* **38**, 9355–9363 (2018).
195. Korogod, N., Petersen, C. C. & Knott, G. W. Ultrastructural analysis of adult mouse neocortex comparing aldehyde perfusion with cryo fixation. *Elife* **4**, (2015).
196. Nicholson, C. & Syková, E. Extracellular space structure revealed by diffusion analysis. *Trends Neurosci* **21**, 207–215 (1998).
197. Thorne, R. G. & Nicholson, C. *In vivo* diffusion analysis with quantum dots and dextrans predicts the width of brain extracellular space. *Proceedings of the National Academy of Sciences* **103**, 5567–5572 (2006).
198. Thorne, R. G., Lakkaraju, A., Rodriguez-Boulan, E. & Nicholson, C. *In vivo* diffusion of lactoferrin in brain extracellular space is regulated by interactions with heparan sulfate. *Proceedings of the National Academy of Sciences* **105**, 8416–8421 (2008).
199. Nance, E. A. *et al.* A Dense Poly(Ethylene Glycol) Coating Improves Penetration of Large Polymeric Nanoparticles Within Brain Tissue. *Sci Transl Med* **4**, (2012).
200. Godin, A. G. *et al.* Single-nanotube tracking reveals the nanoscale organization of the extracellular space in the live brain. *Nat Nanotechnol* **12**, 238–243 (2017).
201. Lau, L. W., Cua, R., Keough, M. B., Haylock-Jacobs, S. & Yong, V. W. Pathophysiology of the brain extracellular matrix: a new target for remyelination. *Nat Rev Neurosci* **14**, 722–729 (2013).
202. Stylianopoulos, T. *et al.* Diffusion of Particles in the Extracellular Matrix: The Effect of Repulsive Electrostatic Interactions. *Biophys J* **99**, 1342–1349 (2010).
203. Barnes, J. M., Przybyla, L. & Weaver, V. M. Tissue mechanics regulate brain development, homeostasis and disease. *J Cell Sci* **130**, 71–82 (2017).
204. Eby, G. A. & Eby, K. L. Rapid recovery from major depression using magnesium treatment. *Med Hypotheses* **67**, 362–370 (2006).
205. Nicholson, C. & Hrabětová, S. Brain Extracellular Space: The Final Frontier of Neuroscience. *Biophys J* **113**, 2133–2142 (2017).
206. Wight, T. N. Provisional matrix: A role for versican and hyaluronan. *Matrix Biology* **60–61**, 38–56 (2017).

207. Izumikawa, T., Sato, B. & Kitagawa, H. Chondroitin Sulfate Is Indispensable for Pluripotency and Differentiation of Mouse Embryonic Stem Cells. *Sci Rep* **4**, 3701 (2014).
208. Yamaguchi, Y. Lecticans: organizers of the brain extracellular matrix. *Cellular and Molecular Life Sciences* **57**, 276–289 (2000).
209. Manrique-Castano, D. *et al.* Tenascin-C preserves microglia surveillance and restricts leukocyte and, more specifically, T cell infiltration of the ischemic brain. *Brain Behav Immun* **91**, 639–648 (2021).
210. Holley, J. E., Gveric, D., Whatmore, J. L. & Gutowski, N. J. Tenascin C induces a quiescent phenotype in cultured adult human astrocytes. *Glia* **52**, 53–58 (2005).
211. Kamali-Zare, P. & Nicholson, C. Brain extracellular space: geometry, matrix and physiological importance. *Basic Clin Neurosci* **4**, 282–6 (2013).
212. Silva, I., Silva, J., Ferreira, R. & Trigo, D. Glymphatic system, AQP4, and their implications in Alzheimer's disease. *Neurol Res Pract* **3**, 5 (2021).
213. Iliff, J. J. *et al.* A Paravascular Pathway Facilitates CSF Flow Through the Brain Parenchyma and the Clearance of Interstitial Solutes, Including Amyloid β. *Sci Transl Med* **4**, (2012).
214. Thal, D. R., Griffin, W. S. T. & Braak, H. Parenchymal and vascular Aβ-deposition and its effects on the degeneration of neurons and cognition in Alzheimer's disease. *J Cell Mol Med* **12**, 1848–1862 (2008).
215. Lehmenkühler, A., Syková, E., Svoboda, J., Zilles, K. & Nicholson, C. Extracellular space parameters in the rat neocortex and subcortical white matter during postnatal development determined by diffusion analysis. *Neuroscience* **55**, 339–351 (1993).
216. Vořísek, I. & Syková, E. Evolution of Anisotropic Diffusion in the Developing Rat Corpus Callosum. *J Neurophysiol* **78**, 912–919 (1997).
217. Syková, E. Diffusion properties of the brain in health and disease. *Neurochem Int* **45**, 453–466 (2004).
218. van der Toorn, A. *et al.* Dynamic changes in water ADC, energy metabolism, extracellular space volume, and tortuosity in neonatal rat brain during global ischemia. *Magn Reson Med* **36**, 52–60 (1996).
219. Xie, L. *et al.* Sleep Drives Metabolite Clearance from the Adult Brain. *Science (1979)* **342**, 373–377 (2013).
220. Hablitz, L. M. *et al.* Increased glymphatic influx is correlated with high EEG delta power and low heart rate in mice under anesthesia. *Sci Adv* **5**, (2019).
221. Coleman, L. G., Liu, W., Oguz, I., Styner, M. & Crews, F. T. Adolescent binge ethanol treatment alters adult brain regional volumes, cortical extracellular matrix protein and behavioral flexibility. *Pharmacol Biochem Behav* **116**, 142–151 (2014).
222. Streitberger, K.-J. *et al.* Brain Viscoelasticity Alteration in Chronic-Progressive Multiple Sclerosis. *PLoS One* **7**, e29888 (2012).
223. Sack, I. *et al.* The impact of aging and gender on brain viscoelasticity. *Neuroimage* **46**, 652–657 (2009).
224. Sethi, M. K. & Zaia, J. Extracellular matrix proteomics in schizophrenia and Alzheimer's disease. *Anal Bioanal Chem* **409**, 379–394 (2017).
225. Naudí, A. *et al.* Lipidomics of Human Brain Aging and Alzheimer's Disease Pathology. in 133–189 (2015). doi:10.1016/bs.irn.2015.05.008.
226. Gonzalez-Riano, C. *et al.* Metabolic Changes in Brain Slices over Time: a Multiplatform Metabolomics Approach. *Mol Neurobiol* **58**, 3224–3237 (2021).

227. Bang, S., Jeong, S., Choi, N. & Kim, H. N. Brain-on-a-chip: A history of development and future perspective. *Biomicrofluidics* **13**, 051301 (2019).
228. Sadakane, O. *et al.* Long-Term Two-Photon Calcium Imaging of Neuronal Populations with Subcellular Resolution in Adult Non-human Primates. *Cell Rep* **13**, 1989–1999 (2015).
229. Li, M., Liu, F., Jiang, H., Lee, T. S. & Tang, S. Long-Term Two-Photon Imaging in Awake Macaque Monkey. *Neuron* **93**, 1049-1057.e3 (2017).
230. Huang, Y., Williams, J. C. & Johnson, S. M. Brain slice on a chip: opportunities and challenges of applying microfluidic technology to intact tissues. *Lab Chip* **12**, 2103 (2012).
231. Gutiérrez, R. & Heinemann, U. Synaptic reorganization in explanted cultures of rat hippocampus. *Brain Res* **815**, 304–316 (1999).
232. Sillay, K. A., McClatchy, S. G., Shepherd, B. A., Venable, G. T. & Fuehrer, T. S. Image-guided Convection-enhanced Delivery into Agarose Gel Models of the Brain. *Journal of Visualized Experiments* (2014) doi:10.3791/51466.
233. Zhi-Jian Chen, Broaddus, W. C., Viswanathan, R. R., Raghavan, R. & Gillies, G. T. Intraparenchymal drug delivery via positive-pressure infusion: experimental and modeling studies of poroelasticity in brain phantom gels. *IEEE Trans Biomed Eng* **49**, 85–96 (2002).
234. Ogawa, B. *et al.* Reversible aberration of neurogenesis targeting late-stage progenitor cells in the hippocampal dentate gyrus of rat offspring after maternal exposure to acrylamide. *Arch Toxicol* **86**, 779–790 (2012).
235. Iwashita, M. *et al.* Brain-stiffness-mimicking tilapia collagen gel promotes the induction of dorsal cortical neurons from human pluripotent stem cells. *Sci Rep* **9**, 3068 (2019).
236. Curtis, C., Toghani, D., Wong, B. & Nance, E. Colloidal stability as a determinant of nanoparticle behavior in the brain. *Colloids Surf B Biointerfaces* **170**, 673–682 (2018).
237. Ting, J. T. *et al.* A robust ex vivo experimental platform for molecular-genetic dissection of adult human neocortical cell types and circuits. *Sci Rep* **8**, 8407 (2018).
238. Damodarasamy, M. *et al.* The microvascular extracellular matrix in brains with Alzheimer's disease neuropathologic change (ADNC) and cerebral amyloid angiopathy (CAA). *Fluids Barriers CNS* **17**, 60 (2020).
239. Qian, X., Song, H. & Ming, G. Brain organoids: advances, applications and challenges. *Development* **146**, (2019).
240. Silvia, N. & Dai, G. Cerebral organoids as a model for glioblastoma multiforme. *Curr Opin Biomed Eng* **13**, 152–159 (2020).
241. Liu, J., Li, J. & Gu, M. The correlation between myocardial function and cerebral hemodynamics in term infants with hypoxic-ischemic encephalopathy. *J Trop Pediatr* **53**, 44–48 (2006).
242. Zhang, F. *et al.* Generation-6 hydroxyl PAMAM dendrimers improve CNS penetration from intravenous administration in a large animal brain injury model. *Journal of Controlled Release* **249**, 173–182 (2017).
243. Jorio, A. & Saito, R. Raman spectroscopy for carbon nanotube applications. *J Appl Phys* **129**, (2021).
244. Nance, E. *et al.* Non-invasive delivery of stealth, brain-penetrating nanoparticles across the blood − brain barrier using MRI-guided focused ultrasound. *Journal of Controlled Release* **189**, 123–132 (2014).

245. Feigin, V. L. *et al.* Global, regional, and national burden of neurological disorders, 1990–2016: a systematic analysis for the Global Burden of Disease Study 2016. *Lancet Neurol* **18**, 459–480 (2019).
246. Lesniak, W. G. *et al.* Biodistribution of Fluorescently Labeled PAMAM Dendrimers in Neonatal Rabbits: Effect of Neuroinflammation. *Mol Pharm* **10**, 4560–4571 (2013).
247. Zhang, M. *et al.* Quantum dot cellular uptake and toxicity in the developing brain: implications for use as imaging probes. *Nanoscale Adv* **1**, 3424–3442 (2019).
248. Stylianopoulos, T. *et al.* Diffusion of Particles in the Extracellular Matrix: The Effect of Repulsive Electrostatic Interactions. *Biophys J* **99**, 1342–1349 (2010).
249. Zhang, F. *et al.* Surface functionality affects the biodistribution and microglia-targeting of intra-amniotically delivered dendrimers. *Journal of Controlled Release* **237**, 61–70 (2016).
250. Nance, E. *et al.* Nanoscale effects in dendrimer-mediated targeting of neuroinflammation. *Biomaterials* **101**, 96–107 (2016).
251. Thorne, R. G. & Nicholson, C. *In vivo* diffusion analysis with quantum dots and dextrans predicts the width of brain extracellular space. *Proceedings of the National Academy of Sciences* **103**, 5567–5572 (2006).
252. Nance, E. *et al.* Brain-Penetrating Nanoparticles Improve Paclitaxel Efficacy in Malignant Glioma Following Local Administration. *ACS Nano* **8**, 10655–10664 (2014).
253. Timbie, K. F. *et al.* MR image-guided delivery of cisplatin-loaded brain-penetrating nanoparticles to invasive glioma with focused ultrasound. *Journal of Controlled Release* **263**, 120–131 (2017).
254. Zhang, C. *et al.* Convection enhanced delivery of cisplatin-loaded brain penetrating nanoparticles cures malignant glioma in rats. *Journal of Controlled Release* **263**, 112–119 (2017).
255. Joseph, A. *et al.* Curcumin-loaded polymeric nanoparticles for neuroprotection in neonatal rats with hypoxic-ischemic encephalopathy. *Nano Res* **11**, 5670–5688 (2018).
256. Nance, E. *et al.* Nanoscale effects in dendrimer-mediated targeting of neuroinflammation. *Biomaterials* **101**, 96–107 (2016).
257. Kannan, S. *et al.* Dendrimer-Based Postnatal Therapy for Neuroinflammation and Cerebral Palsy in a Rabbit Model. *Sci Transl Med* **4**, (2012).
258. Huang, X. *et al.* The Shape Effect of Mesoporous Silica Nanoparticles on Biodistribution, Clearance, and Biocompatibility *in Vivo*. *ACS Nano* **5**, 5390–5399 (2011).
259. Geng, Y. *et al.* Shape effects of filaments versus spherical particles in flow and drug delivery. *Nat Nanotechnol* **2**, 249–255 (2007).
260. Lee, K. L. *et al.* Shape matters: the diffusion rates of TMV rods and CPMV icosahedrons in a spheroid model of extracellular matrix are distinct. *Biomater Sci* **1**, 581 (2013).
261. Ridolfo, R. *et al.* Exploring the Impact of Morphology on the Properties of Biodegradable Nanoparticles and Their Diffusion in Complex Biological Medium. *Biomacromolecules* **22**, 126–133 (2021).
262. *Electrochemical Methods for Neuroscience.* . (2007).
263. Xiao, F., Nicholson, C., Hrabe, J. & Hrabětová, S. Diffusion of Flexible Random-Coil Dextran Polymers Measured in Anisotropic Brain Extracellular Space by Integrative Optical Imaging. *Biophys J* **95**, 1382–1392 (2008).

264. Binder, D. K., Papadopoulos, M. C., Haggie, P. M. & Verkman, A. S. *In Vivo* Measurement of Brain Extracellular Space Diffusion by Cortical Surface Photobleaching. *The Journal of Neuroscience* **24**, 8049–8056 (2004).
265. Ishikawa-Ankerhold, H. C., Ankerhold, R. & Drummen, G. P. C. Advanced Fluorescence Microscopy Techniques—FRAP, FLIP, FLAP, FRET and FLIM. *Molecules* **17**, 4047–4132 (2012).
266. Dulla, C. *et al.* Imaging of glutamate in brain slices using FRET sensors. *J Neurosci Methods* **168**, 306–19 (2008).
267. Radbruch, H. *et al.* Intravital FRET: Probing Cellular and Tissue Function in Vivo. *Int J Mol Sci* **16**, 11713–11727 (2015).
268. Joyner, K., Yang, S. & Duncan, G. A. Microrheology for biomaterial design. *APL Bioeng* **4**, 041508 (2020).
269. Godin, A. G. *et al.* Single-nanotube tracking reveals the nanoscale organization of the extracellular space in the live brain. *Nat Nanotechnol* **12**, 238–243 (2017).
270. Selvaggi, L. *et al.* Multiple-Particle-Tracking to investigate viscoelastic properties in living cells. *Methods* **51**, 20–26 (2010).
271. Valentine, M. T. *et al.* Colloid surface chemistry critically affects multiple particle tracking measurements of biomaterials. *Biophys J* **86**, 4004–14 (2004).
272. Schneider, C. A., Rasband, W. S. & Eliceiri, K. W. NIH Image to ImageJ: 25 years of image analysis. *Nat Methods* **9**, 671–675 (2012).
273. Zhou, J. *et al.* Highly penetrative, drug-loaded nanocarriers improve treatment of glioblastoma. *Proceedings of the National Academy of Sciences* **110**, 11751–11756 (2013).
274. Zhong, Y. & Wang, G. Three-Dimensional Single Particle Tracking and Its Applications in Confined Environments. *Annual Review of Analytical Chemistry* **13**, 381–403 (2020).
275. McLaughlin, G. A. *et al.* Spatial heterogeneity of the cytosol revealed by machine learning-based 3D particle tracking. *Mol Biol Cell* **31**, 1498–1511 (2020).
276. Wagner, T., Kroll, A., Haramagatti, C. R., Lipinski, H.-G. & Wiemann, M. Classification and Segmentation of Nanoparticle Diffusion Trajectories in Cellular Micro Environments. *PLoS One* **12**, e0170165 (2017).
277. Rosendale, M. *et al.* A Bottom-Up Approach to Red-Emitting Molecular-Based Nanoparticles with Natural Stealth Properties and their Use for Single-Particle Tracking Deep in Brain Tissue. *Advanced Materials* **33**, (2021).
278. Nguyen, M. M. *et al.* Enzyme-Responsive Nanoparticles for Targeted Accumulation and Prolonged Retention in Heart Tissue after Myocardial Infarction. *Advanced Materials* **27**, 5547–5552 (2015).
279. Wong, C. *et al.* Multistage nanoparticle delivery system for deep penetration into tumor tissue. *Proceedings of the National Academy of Sciences* **108**, 2426–2431 (2011).
280. Yu, M. *et al.* Rapid transport of deformation-tuned nanoparticles across biological hydrogels and cellular barriers. *Nat Commun* **9**, 2607 (2018).
281. Tønnesen, J. & Nägerl, U. V. Superresolution imaging for neuroscience. *Exp Neurol* **242**, 33–40 (2013).
282. Kim, H., Kim, E., Park, M., Lee, E. & Namkoong, K. Organotypic hippocampal slice culture from the adult mouse brain: A versatile tool for translational neuropsychopharmacology. *Prog Neuropsychopharmacol Biol Psychiatry* **41**, 36–43 (2013).

Appendix A: Supplemental Information for Chapter 2

Table S2.1. Summary of median (±IQR) values for total cell count, % cell damage, % microglia-PI co-localization, % microglia-DAPI co-localization, and % neuron-PI co-localization in healthy OWH slices. Number of asterisks (*) following the IQR denotes extent of non-Gaussian distribution if the dataset failed

the D'Agostino-Pearson omnibus K2 test for normality. Normally distributed datasets are denoted with a hash symbol (#) following the IQR.

	6DIV HC		8DIV HC		10DIV HC	
	Cortex	Midbrain	Cortex	Midbrain	Cortex	Midbrain
Median cell count (±IQR)	290 ± 74.0#	315 ± 58.0#	334.5 ± 103.7#	391 ± 61.5#	374 ± 57.5#	389 ± 73*
Median % cell damage (±IQR)	0.00 ± 4.10****	0.00 ± 0.00****	8.00 ± 6.25#	0.00 ± 5.50****	11.0 ± 14***	2.00 ± 9.75****
Median % NeuN-PI nuclei co-localization (±IQR)	0.00 ± 0.00****	0.00 ± 0.00	4.92 ± 4.04****	0.00 ± 2.57****	0.00 ± 1.00***	0.00 ± 0.00**
Median % Iba1-PI nuclei co-localization (±IQR)	5.10 ± 20.03#	0.00 ± 1.52****	1.00 ± 3.00#	0.00 ± 1.00****	20.85 ± 18.72#	11.65 ± 24.81#
Median % Iba1/nuclei co-localization (±IQR)	26.5 ± 26.3#	18.4 ± 5.90*	27.2 ± 17.9#	31.6 ± 8.90#	23.6 ± 8.80#	28.3 ± 25.9#

Table S2.2. Summary of median (±IQR) values for total cell count, % cell damage, % microglia-PI co-localization, % microglia-DAPI co-localization, and % neuron-PI co-localization following a single 50 nM exposure. Number of asterisks (*) following the IQR denotes extent of non-Gaussian distribution if the dataset failed the D'Agostino-Pearson omnibus K2 test for normality. Normally distributed datasets are denoted with a hash symbol (#) following the IQR.

	8DIV 50 nM (single exposure)		10DIV 50 nM (single exposure)	
	Cortex	Midbrain	Cortex	Midbrain
Median cell count (±IQR)	255 ± 168#	248 ± 166*	342 ± 54.0#	387.5 ± 88.0#
Median % cell damage (±IQR)	38.0 ± 30.3*	26.5 ± 23.8#	9.50 ± 18.8*	40.0 ± 18.0#
Median % NeuN-PI nuclei co-localization (±IQR)	54.6 ± 41.1#	50.0 ± 22.4#	70.0 + 45.0#	81.0 ± 19.5*
Median % Iba1-PI nuclei co-localization (±IQR)	80.0 ± 20.0#	70.0 ± 12.5#	21.4 ± 35.7#	71.2 ± 20.4#
Median % Iba1/nuclei co-localization (±IQR)	62.4 ± 20.3#	61.9 ± 13.4#	28.7 ± 10.1#	26.2 ± 21.0#

Table S2.3. Summary of median (±IQR) values for total cell count, % cell damage, % microglia-PI co-localization, % microglia-DAPI co-localization, and % neuron-PI co-localization following repeated 50 nM exposure. Number of asterisks (*) following the IQR denotes extent of non-Gaussian distribution if the

dataset failed the D'Agostino-Pearson omnibus K2 test for normality. Normally distributed datasets are denoted with a hash symbol (#) following the IQR.

	6DIV 50 nM		8DIV 50 nM (repeated exposure)		10DIV 50 nM (repeated exposure)	
	Cortex	Midbrain	Cortex	Midbrain	Cortex	Midbrain
Median cell count (±IQR)	281 ± 105$^{\#}$	319 ± 117.3$^{\#}$	228.5 ± 196.5*	205 ± 150.8*	296 ± 237**	303 ± 164*
Median % cell damage (±IQR)	30.0 ± 19.0$^{\#}$	27.8 ± 14.2$^{\#}$	45.0 ± 15.8$^{\#}$	39.5 ± 36.0$^{\#}$	74.0 ± 16.0***	68.0 ± 39.0$^{\#}$
Median % NeuN-PI nuclei co-localization (±IQR)	36.5 ± 26.3$^{\#}$	40.0 ± 24.3$^{\#}$	48.7 ± 49.8$^{\#}$	48.5 ± 17.2$^{\#}$	77.0 ± 38.5$^{\#}$	73.0 ± 31.5$^{\#}$
Median % Iba1-PI nuclei co-localization (±IQR)	4.24 ± 31.9*	24.3 ± 42.4$^{\#}$	94.5 ± 15.0$^{\#}$	89.5 ± 12.5$^{\#}$	74.0 ± 10.4$^{\#}$	78.0 ± 18.1$^{\#}$
Median % Iba1/nuclei co-localization (±IQR)	32.7 ± 12.2$^{\#}$	30.6 ± 18.5$^{\#}$	38.9 ± 13.0$^{\#}$	44.3 ± 16.8$^{\#}$	50.4 ± 7.86$^{\#}$	33.2 + 16.0$^{\#}$

Table S2.4. Summary of median (±IQR) values of total cell count and % cell damage (by region and aggregate) following single and repeat 10 μM exposure. Number of asterisks (*) following the IQR denotes extent of non-Gaussian distribution if the dataset failed the D'Agostino-Pearson omnibus K2 test for normality. Normally distributed datasets are denoted with a hash symbol (#) following the IQR.

	6DIV 10 μM			8DIV 10 μM (single exposure)			8DIV 10 μM (repeated exposure)		
	Cortex	Midbrain	Aggregate	Cortex	Midbrain	Aggregate	Cortex	Midbrain	Aggregate
Median cell count (±IQR)	82.5 ± 36.1$^{\#}$	109 ± 36.0****	95.5 ± 38.0****	51.5 ± 23.0$^{\#}$	74.0 ± 36.0$^{\#}$	57.0 ± 22.0****	65.0 ± 24.0***	48.0 ± 7.00$^{\#}$	89.5 ± 9.75*
Median % cell damage (±IQR)	77.0 ± 13.0$^{\#}$	77.0 ± 19.6*	78.2 ± 14.2$^{\#}$	91.0 ± 12.0$^{\#}$	81.0 ± 8.50$^{\#}$	85.0 ± 13.0*	90.0 ± 5.50***	86.0 ± 12.0$^{\#}$	58.5 ± 40.2$^{\#}$

Table S2.5. Physicochemical properties for the two batches of 40 nm polystyrene-(poly)ethylene glycol (PS-PEG) nanoparticles used for MPT measurements in this study.

40 nm PS-PEG	Number mean size (nm) ± SEM	PDI ± SEM	Zeta potential (mV) ± SEM
Batch 1	55.2 ± 2.83	0.08 ± 0.014	-2.56 ± 0.31

Batch 2	54.6 ± 1.92	0.06 ± 0.015	-3.13 ± 0.68

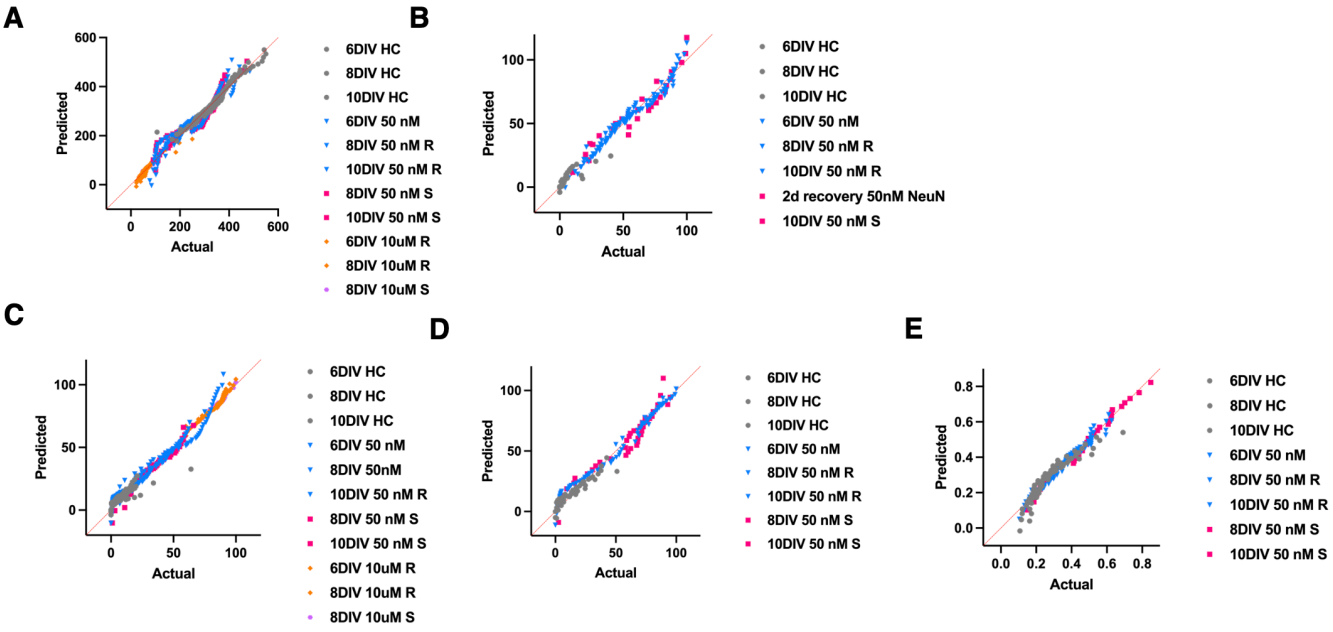

Figure S2.1. Normality QQ plots of aggregate (A) total cell count, (B) % neuron-PI co-localization, (C) % cell damage, (D) % microglia-PI co-localization and (E) microglia-DAPI co-localization for all relevant experimental groups.

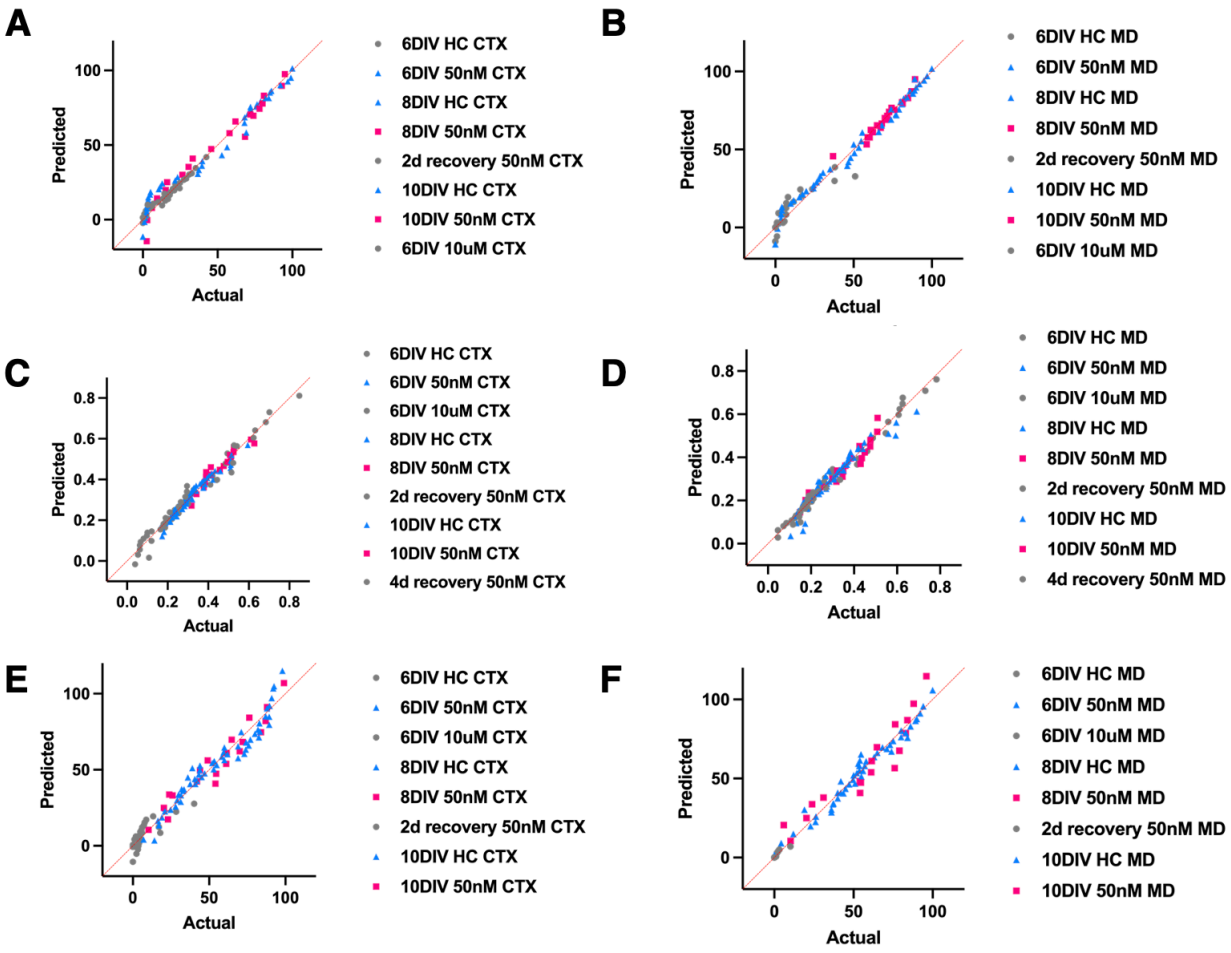

Figure S2.2 Normality QQ plots of regional % NeuN-PI co-localization in the **(A)** cortex and **(B)** midbrain, % microglia-DAPI co-localization (density) in the **(C)** cortex and **(D)** midbrain, **%** microglia-PI co-localization in the **(E)** cortex and **(F)** midbrain for all relevant experimental groups.

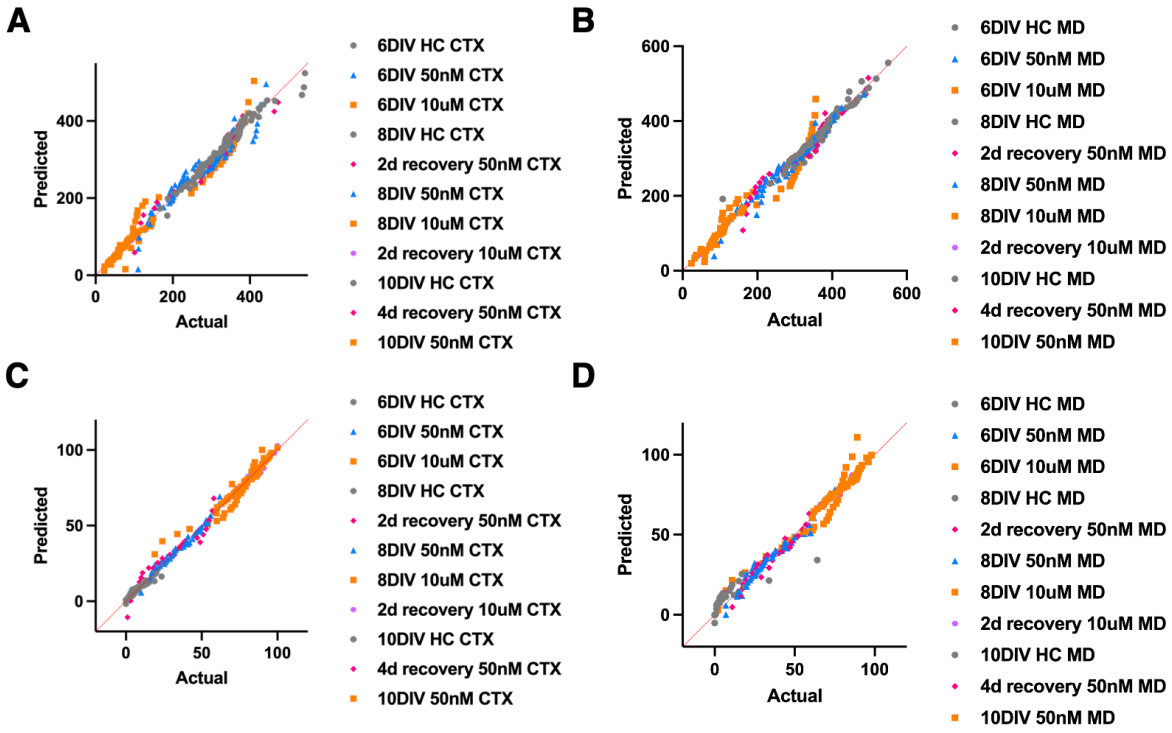

Figure S2.3. Normality QQ plots of regional cell counts in the **(A)** cortex and **(B)** midbrain and % cell damage in the **(C)** cortex and **(D)** midbrain for all relevant experimental groups.

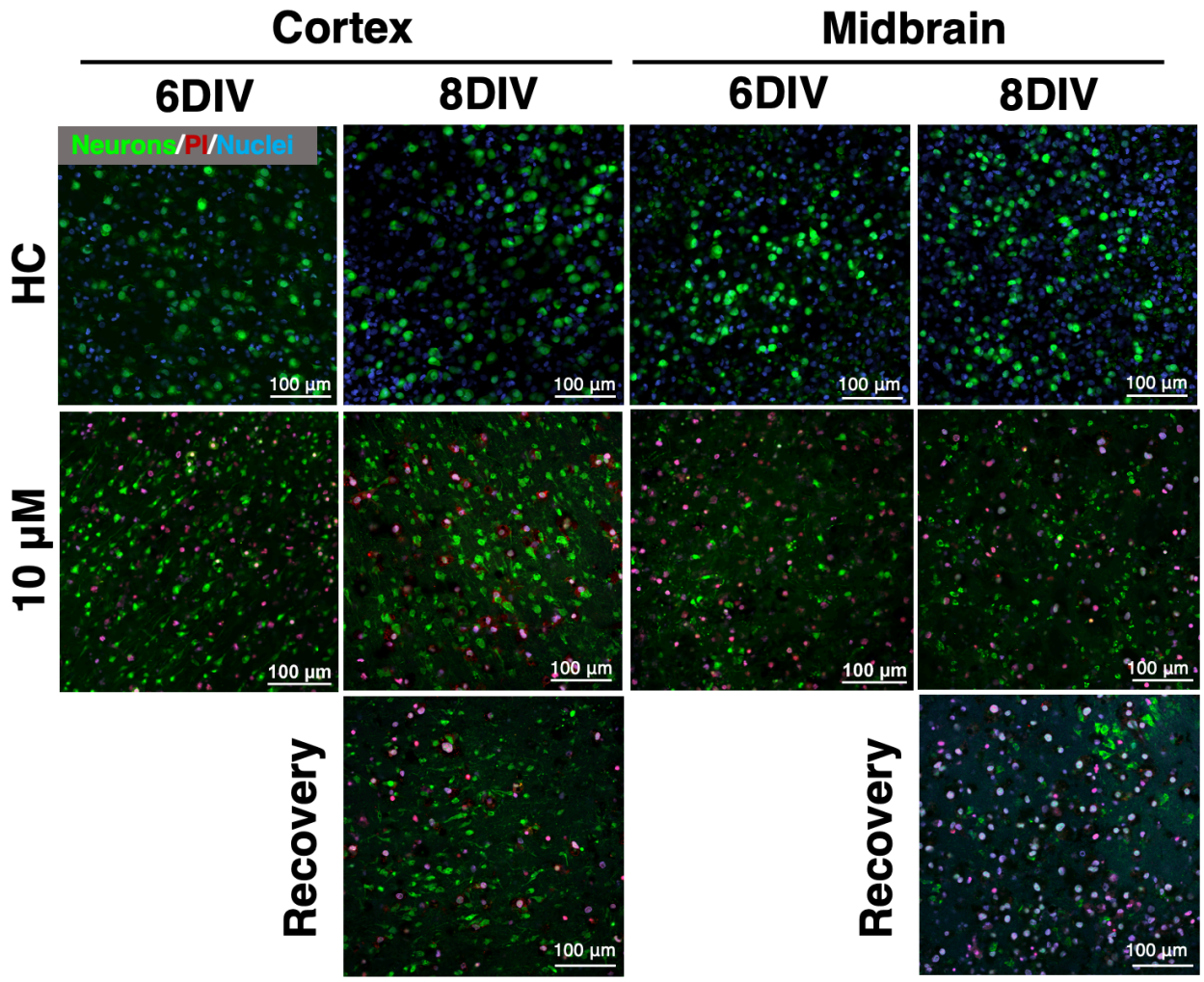

Figure S2.4. Representative images of NeuN+ neurons in the cortex and midbrain of OWH slices (N=2 OWH slices/condition) exposed to 10 µM ROT with n=5-10 images taken at 40x magnification per condition in each region).

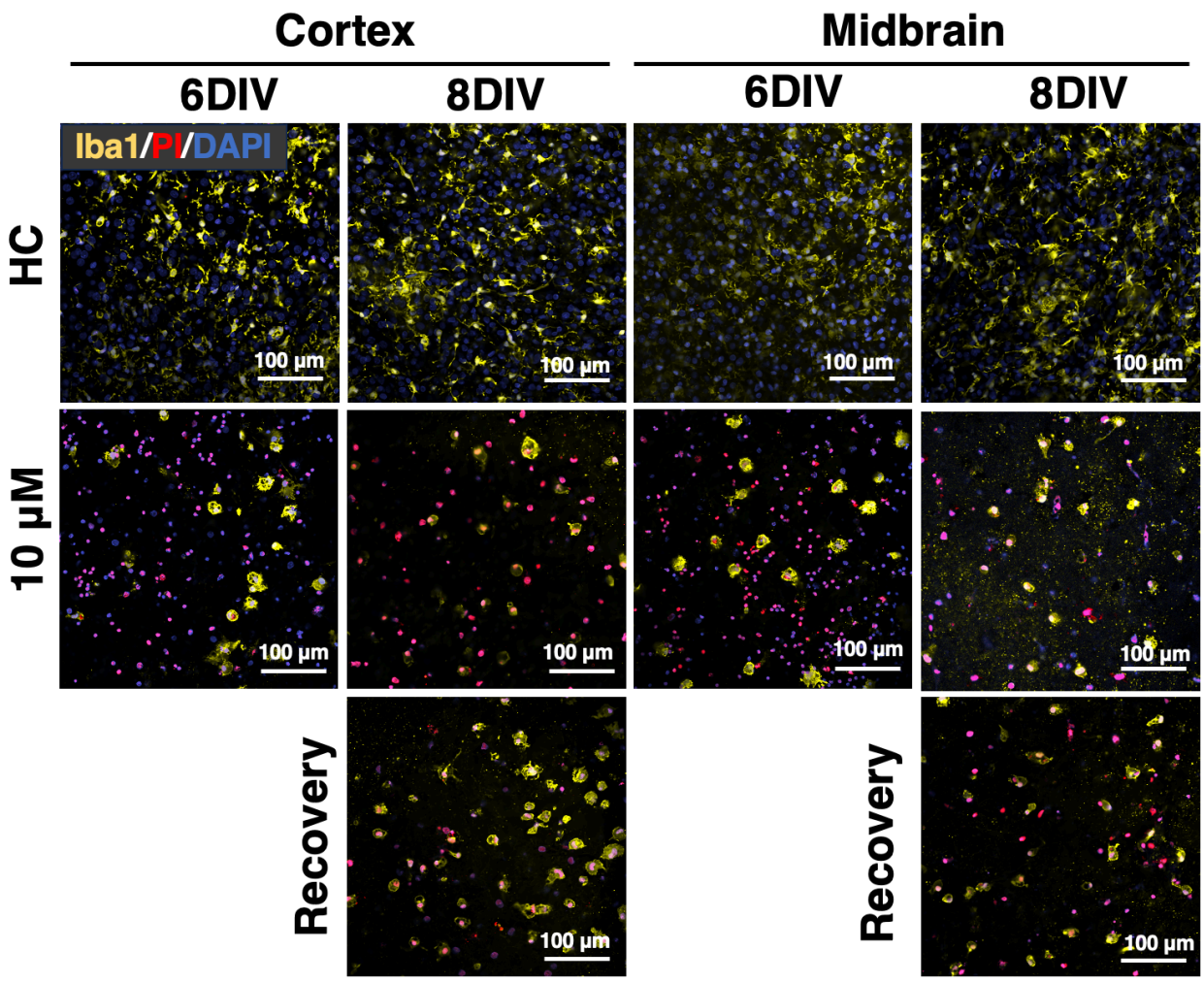

Figure S2.5. Representative images of Iba1+ microglia in the cortex and midbrain of OWH slices (N=2 OWH slices/condition) exposed to 10 µM ROT with n=5-10 images taken at 40x magnification per condition in each region).

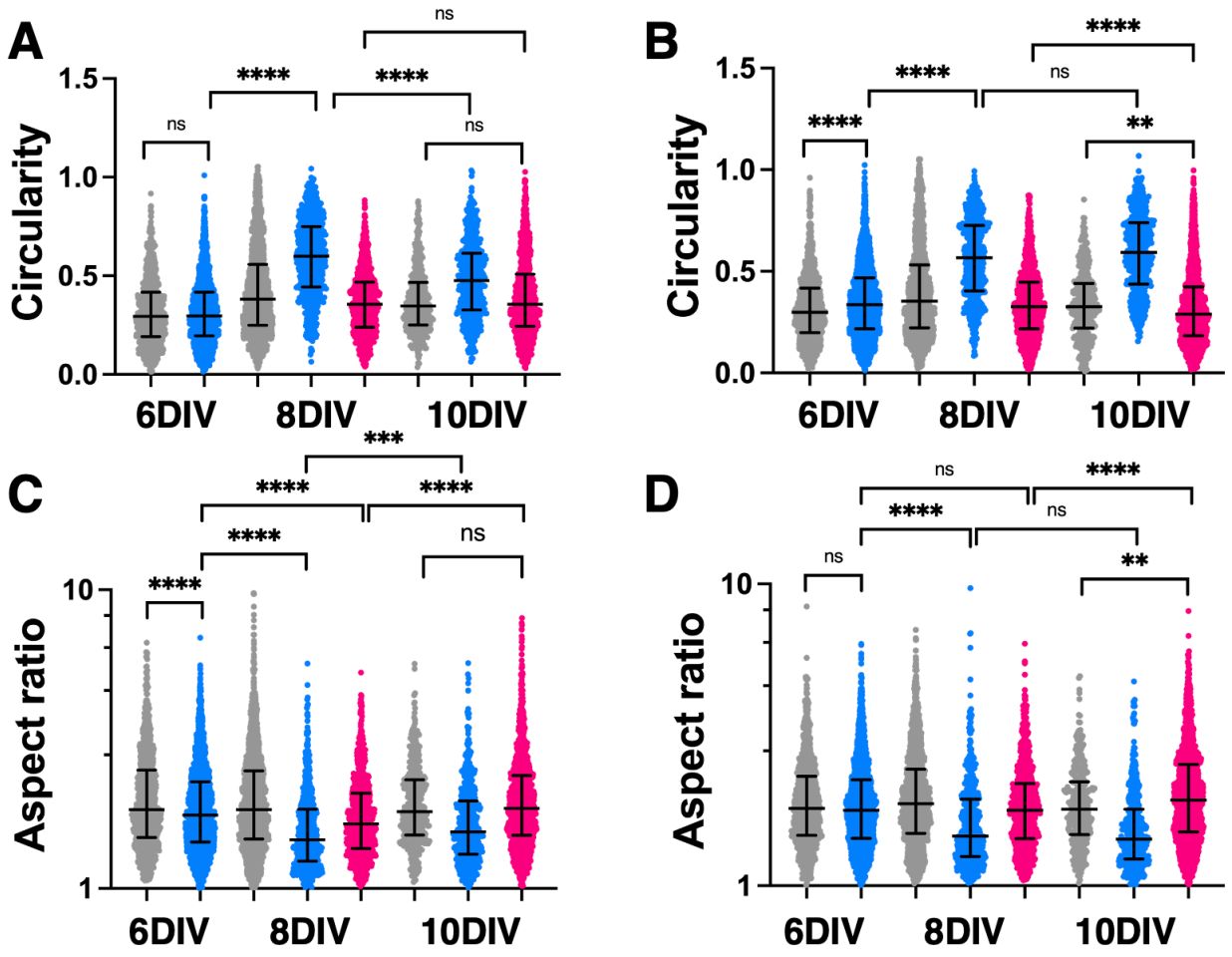

Figure S2.6. Regional differences across experimental groups for microglial morphological features. Circularity (4π*area/perimeter^2) of Li-thresholded microglia in the **(A)** cortex and **(B)** midbrain of OWH slices. Aspect ratio (major axis length/minor axis length) of Li-thresholded microglia in the **(C)** cortex and **(D)** midbrain of OWH slices. Each datapoint represents a single cell in an image (N=2-3 OWH slices/ group/region) with n=5-10 images taken at 40x magnification. All code available at https://github.com/Nance-Lab/cellmorphflows.

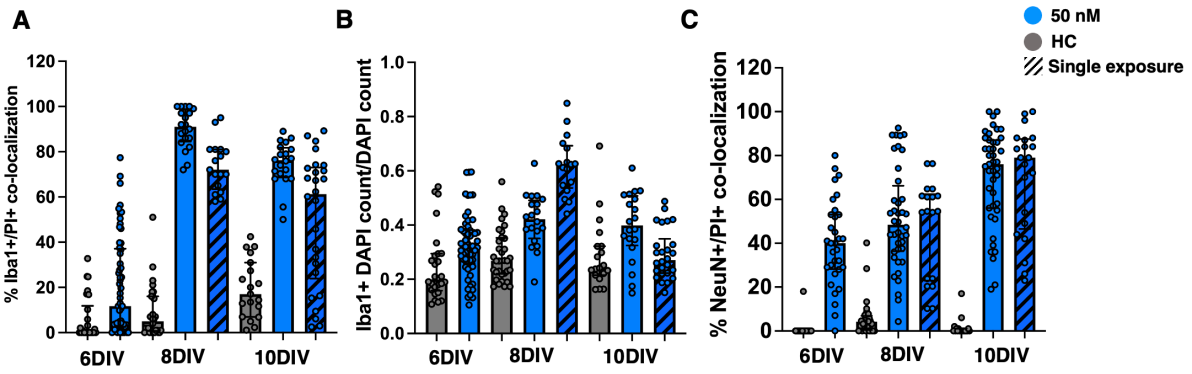

Figure S2.7. Aggregate (A) % microglia-PI+ co-localization, (B) % microglia-DAPI+ co-localization and (C) % neuron-PI+ co-localization damage, (D) % microglia-PI co-localization and for OWH slices (N=2-3 OWH slices/group) from n=5-10 images taken at 40x magnification per condition in each region.

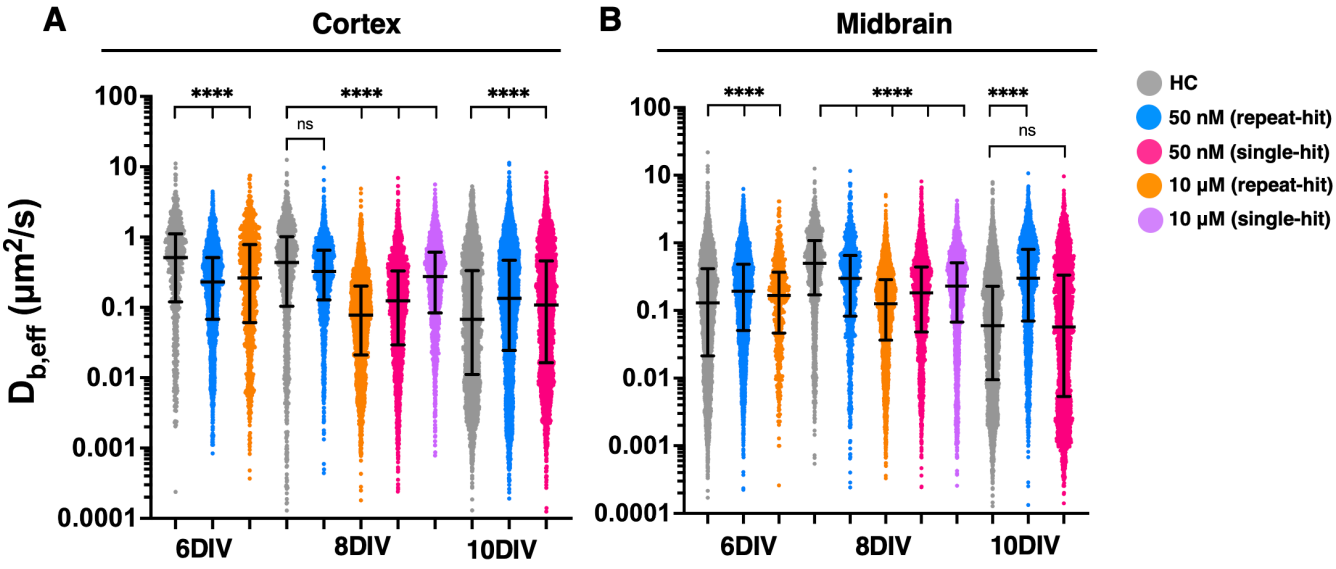

Figure S2.8. Distributions of effective diffusion coefficients ($D_{b,eff}$) comparing 40 nm PS-PEG particle diffusion for all experimental groups in the **(A)** cortex and **(B)** midbrain. Particles were tracked in 2-3 slices per each condition, with 3-5 videos were collected in each region per condition, resulting in > 2,000 trajectories per condition. All videos were acquired at 67 frames per second, 100x magnification, and within 1 hour following particle incubation. Representative effective diffusion coefficients and viscosities are calculated at a trajectory lag time of $\tau = 0.1$ s. For grouped significance bars, number of asterisks (*) denotes significance relative to healthy (gray) distributions.

Appendix B: Supplemental Information for Chapter 3

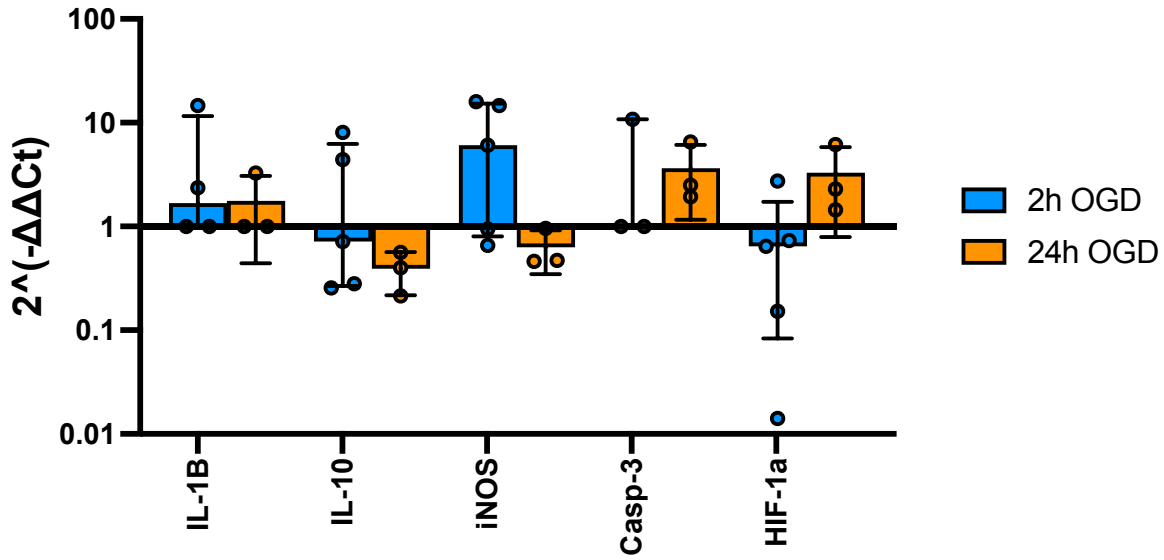

Figure S3.1. Fold change expression of inflammatory markers at 2h (blue) and 24h (orange) post 30m OGD. Data points represent RNA from three pooled slices, distributed over n=3-5 individual experiments.

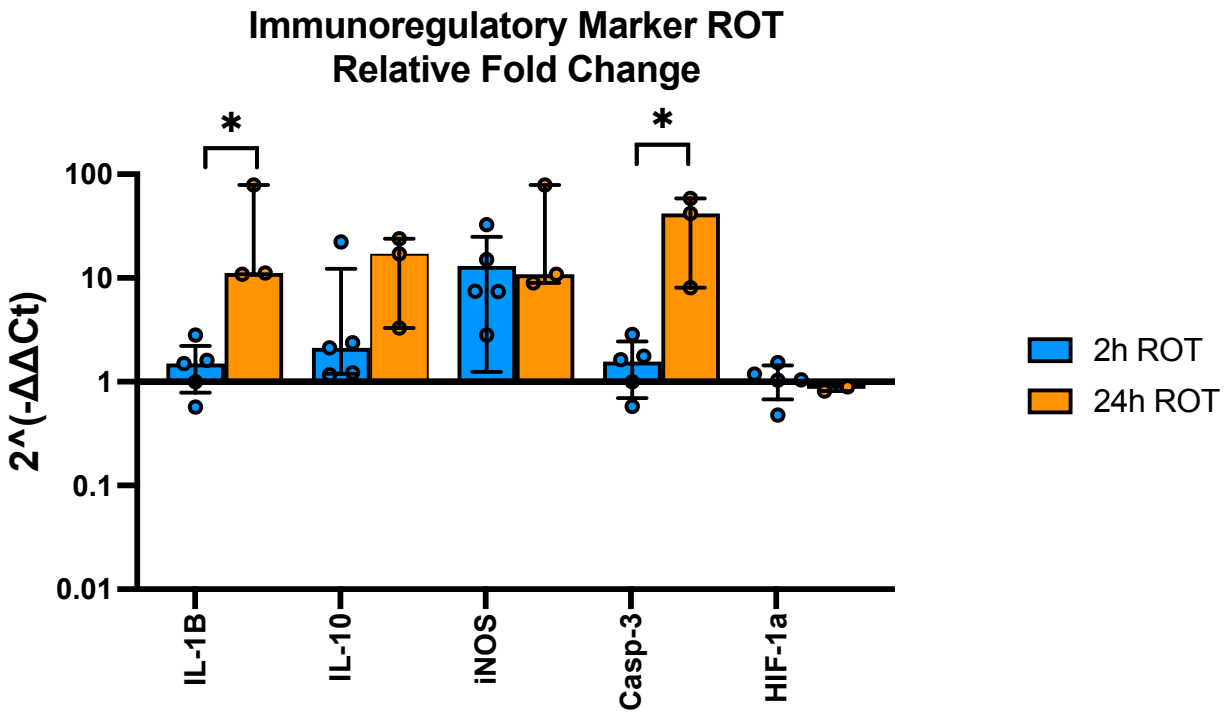

Figure S3.2. Fold change expression of inflammatory markers at 2h (blue) and 24h (orange) post 50 nM ROT. Data points represent RNA from three pooled slices, distributed over n=3-5 individual experiments.